NOVEL BCU-BASED METHODS FOR ENHANCING POWER SYSTEM TRANSIENT STABILITY

A Dissertation

Presented to the Faculty of the Graduate School

of Cornell University

In Partial Fulfillment of the Requirements for the Degree of

Doctor of Philosophy

by

Warut Suampun

August 2013

NOVEL BCU-BASED METHODS FOR ENHANCING POWER SYSTEM TRANSIENT STABILITY

Warut Suampun, Ph.D.

Cornell University 2013

Transient stability is the ability of the power system to maintain synchronism when subjected to a severe transient disturbance such as transmission line shortage, loss of a transmission line, loss of generation, or loss of a large load. Loss of synchronism due to transient instability is very dangerous because it can lead to a widespread power outage, and moreover it is extremely fast to manifest and affect the system, usually within 2 to 3 seconds of the initial disturbance. As a result, the best approach to deal with transient instability is to detect and prevent it before it actually happens. The BCU (Boundary of stability region based Controlling Unstable equilibrium point) method for direct analysis of power system transient stability prevails over existing assessment methods due to (1) its fast computational speed, (2) its ability to provide conservative index for degree of stability, and (3) its ability to provide useful information regarding how to derive enhancement control actions. In this thesis work, we expand the applicability of the BCU method to a wider range of power system applications and models, by providing numerical illustrations, conducting critical evaluations, and developing new solution methods. We propose new BCU-based methods for enhancing power system transient stability based on the TSCOPF (transient stability constrained optimal power flow) and direct generation rescheduling frameworks. Our methods combine the advantages of the traditional transient stability enhancement/preventive control schemes with that of the dynamic and geometric characteristics of the stability regions of the corresponding power system transient

stability model. Our methods were tested on several practical power systems with large contingency lists and the advantages of using this novel framework are clearly evident. This framework not only significantly improves the computational aspects of the algorithm (i.e. speed, and the ability to handle large-scale power systems with large contingency lists), but also enhances the overall accuracy in enforcing transient stability within the methods. Numerical studies of the stability regions for various power system models are also conducted to illustrate the CUEP method for DAE system, and to evaluate several CUEP-based direct methods in approximating relevant stability boundaries.

BIOGRAPHICAL SKETCH

Warut Suampun was born in Bangkok, Thailand on October 29, 1982. Upon graduating from Chulalongkorn University Demonstration high school, he received a full scholarship from the royal Thai government to pursue his higher education in the United States of America. He attended Cornell University, Ithaca, NY, in 2001 and obtained the Bachelor's degree in electrical and computer engineering in 2005. He continued his study in the Department of Electrical and Computer Engineering at Cornell University to pursue his doctoral studies. His primary research interests include Power System Transient Stability, Nonlinear Systems, Preventive and Enhancement controls for Power System Voltage and Transient Stability.

Dedicated to my parents

ACKNOWLEDGMENTS

I would like to express my deepest gratitude to my thesis advisor, Prof. Hsiao-Dong Chiang, for the guidance and support he has provided throughout my PhD studies. His enthusiasm, dedicated efforts, and superb teaching skills were extremely inspirational and helpful for me in successfully pursuing this research work. It has been a great pleasure and an honor for me to have Prof. Robert Thomas and Prof. John Guckenheimer on my thesis committee. I am very grateful for the excellent courses I took with them. This dissertation would not have been possible without their valuable discussions and suggestions on my research work. Special thanks to Dr. Byoung-Kon Choi, Dr. Hua Li, Dr. Luis Alberto and Dr. Bin Wang for their helpful comments and discussions.

I would like to thank my friends in the ECE department for many interesting discussions and for making my life at Cornell so enjoyable: Dr. Jeng-Heui Chen, Dr. Chandan Reddy, Stephen Jhun, Cheng Li, Xiaozhe Wang, Robert Owusu Mireku, and Jeremy Keen. I was also fortunate to have known so many great Thai friends here at Cornell whom I would like to thank for making this little town feel like home to me. I truly thank my wonderful friend, Bye-sah, for being there for me during the toughest time of my life. Thanks for giving me strength and encouragement, and for the wonderful time we shared together.

Last and the most important, I wish to extend my utmost gratitude to all members of my family, especially my parents, Mr. Umpon and Mrs. Nisakorn Suampun, and my grandparents, Mr. Tawee and Mrs. Siripen Wangwiwatsilp, for their unconditional love, support and encouragement. This journey would not have been as wonderful nor possible without them.

TABLE OF CONTENTS

LIST OF FIGURES

LIST OF TABLES

CHAPTER 1
Introduction

1.1 Transient Stability in Power Systems

Transient stability analysis is associated with the ability of a power system to maintain its machine synchronism following a large disturbance, or a *fault*. The mathematical model for transient stability is described by either a set of nonlinear differential algebraic equations (DAE) or ordinary differential equations (ODE). There are three stages in transient stability analysis: *pre-fault* stage, *fault-on* stage, and *post-fault* stage [1]. Mathematically, the transient stability of a power system can be determined by checking the initial state of the post-fault trajectory. If this point lies inside the stability region of the post-fault stable equilibrium point (SEP), then the post-fault system trajectory is stable.

The three stages in power system transient stability analysis are illustrated in Figure 1.1 and can be mathematically described as follows:

1. Pre-Fault

In the pre-fault stage, the system is operating at a pre-fault SEP or x_s^{pre}. The dynamics of this stage is described by:

$$\dot{x} = F_1(x), \quad t < 0, \quad x \in R^{2n} \tag{1.1}$$

where $x_s^{pre} = x(0)$, and state variables are machine angles and angular speeds.

2. Fault-On

At $t = 0$, the system experiences a large disturbance and enters the fault-on stage whose dynamics are governed by

$$\dot{x} = F_2(x), \quad x(0) = x_s^{pre}, \quad 0 \le t < t_{cl} \tag{1.2}$$

where t_{cl} is the time when the protective system is activated. It should be noted that the fault-on stage can also be modeled as several sub-stages when multiple protective devices are activated at different times. For now, we only consider a single-stage fault-on period.

3. Post-Fault

When the fault or disturbance is cleared, the system enters the last stage whose dynamics are described by

$$\dot{x} = f(x), \quad t \ge t_{cl} \tag{1.3}$$

In this stage, the system is assumed to have a post-fault SEP at x_s^{post}.

The fundamental issue of transient stability analysis is whether the system trajectory, starting at the post-fault initial state $x(t_{cl})$, will be able to settle down at x_s^{post}. This can be expressed using the concept of the stability region. The stability region (or the region of attraction $A(x_s^{post})$) of the post fault stable equilibrium point x_s^{post} is defined as the set of points from which the trajectories converge to x_s^{post}. The goal of transient stability analysis is to determine whether the initial point of the post-fault trajectory is located inside the stability region of the post-fault SEP, x_s^{post}. Therefore it can be mathematically expressed by checking the following condition:

$$x(t_{cl}) \in A(x_s^{post}) \tag{1.4}$$

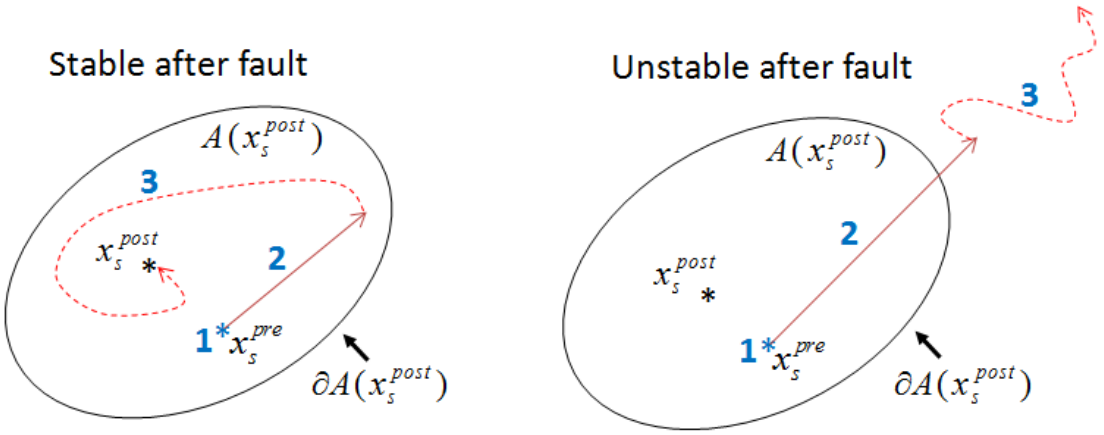

Figure 1.1 Three stages in transient stability analysis. The sustained fault-on trajectory moves towards the stability boundary $\partial A(x_s^{post})$ of post-fault SEP, x_s^{post}. If the initial point of the post-fault trajectory lies inside the stability region, or $x(t_{cl}) \in A(x_s^{post})$, then the post-fault trajectory converges to x_s^{post} and the system is stable after fault. However, if the fault-on trajectory exits the stability region of x_s^{post}, then $x(t_{cl}) \notin A(x_s^{post})$ and the system becomes unstable after fault.

The methods for transient stability assessment can be categorized into two main approaches; the time-domain approach, and the direct methods. In the time-domain approach, complete numerical integrations must be performed at every stage of transient stability analysis. Although this may result in great accuracy in assessing stability, the speed performance suffers due to large computational requirements. Moreover, the time-domain approach does not provide any measurement for the degree of stability (which indicates how stable (or unstable) the post-fault system is). The direct methods have been developed to overcome these limitations. By providing an approximation of the stability boundary, direct methods can assess stability without having to rely on numerical integrations during the post-fault stage. The stability boundary approximation can be used to provide degrees of stability of the system as well. The PEBS method [49], the closest UEP method [12, 47, 94], and the controlling UEP method [13, 50] are energy function based direct methods. Some of the non-energy function based methods include the hyperplane method [51, 52], a quadratic approximation approach [53, 54] and a normal form

approach [55, 56]. The transient stability status of a power system with respect to a fault (or a contingency) can be assessed by these methods and categorized as following:

1) Secure: The critical clearing time (CCT) of the system with respect to the contingency is much larger than the fault clearing time. A secure contingency is considered safe and does not require any further actions.
2) Critical: The CCT of the system with respect to the contingency is slightly larger than the fault clearing time. Although a critical contingency is considered safe, it is still close to instability and can be undesirable. Enhancement control actions can be taken to increase the stability margin. The result is a new system configuration with a larger CCT and hence improved transient stability.
3) Insecure: The CCT of the system with respect to the contingency is smaller than the fault clearing time. The system will become unstable if the contingency occurs. An insecure contingency is considered dangerous and it is crucial that a preventive control action must be taken to bring the CCT to a safe value.

Generally, it takes around 5-8 cycles or 0.083-0.133 second for a 60 Hz system, typical fault clearing times, before the protective relay system is activated to clear a fault. To ensure transient stability, the fault clearing time must be smaller than the system's CCT. This guarantees the post-fault trajectory to stay inside the post-fault stability region and to asymptotically converge to a post-fault stable operating point, or a post-fault SEP. When a contingency is considered critical or unstable, a control action should be immediately taken to move the insecure (or critical) operating point to a new configuration with better transient stability profile.

1.2 BCU Method

A boundary of stability region based controlling unstable equilibrium point method (BCU method) for direct analysis of power system transient stability was proposed in [13]. The BCU method is an energy function based direct method that gives direct transient stability assessment via the critical potential energy value at the controlling unstable equilibrium point (CUEP), a UEP on the post-fault stability boundary whose stable manifold is intersected by the fault-on trajectory. The features distinguishing the BCU method from other existing direct methods are as following:

1) It is capable of consistently computing the exact CUEP relative to a fault-on trajectory.
2) It has a sound theoretical basis which can be found in [6, 13, 14].

1.2.1 The BCU methodology [6, 13, 14]

The BCU method finds the CUEP of the original system via a reduced-state system whose CUEP is computationally cheaper and easier to obtain. A general network-preserving transient stability model with losses can be described by a set of nonlinear differential algebraic equations (DAE) shown in (1.5).

$$\begin{aligned} 0 &= -\frac{\partial U}{\partial u}(u,w,x,y) + g_1(u,w,x,y) \\ 0 &= -\frac{\partial U}{\partial w}(u,w,x,y) + g_2(u,w,x,y) \\ T\dot{x} &= -\frac{\partial U}{\partial x}(u,w,x,y) + g_3(u,w,x,y) \\ \dot{y} &= z \\ M\dot{z} &= -Dz - \frac{\partial U}{\partial y}(u,w,x,y) + g_4(u,w,x,y) \end{aligned} \tag{1.5}$$

where $U(u,w,x,y)$ is a scalar function, and $g(u,w,x,y)$ represents transfer conductances. In developing a BCU method for a given power system stability model, an associated reduced-state model must be defined. The DAE system in (1.6) is the corresponding reduced-state system of the DAE system in (1.5).

$$\begin{aligned} 0 &= -\frac{\partial U}{\partial u}(u,w,x,y) + g_1(u,w,x,y) \\ 0 &= -\frac{\partial U}{\partial w}(u,w,x,y) + g_2(u,w,x,y) \\ T\dot{x} &= -\frac{\partial U}{\partial x}(u,w,x,y) + g_3(u,w,x,y) \\ \dot{y} &= -\frac{\partial U}{\partial y}(u,w,x,y) + g_4(u,w,x,y) \end{aligned} \tag{1.6}$$

It is shown in [6] that the original model in (1.5) and the artificial, reduced-state model in (1.6) satisfy the following static and dynamic properties.

Static Properties ([6], p.280)

(S1) The locations of the equilibrium points of the reduced-state model correspond to the locations of the equilibrium points of the original model.

(S2) The types of equilibrium points of the reduced-state model are the same as those of the original model.

Dynamic Properties ([6], p.281)

(D1) There exists an energy function for the artificial, reduced-state model.

(D2) An equilibrium point, say $(\bar{u},\bar{w},\bar{x},\bar{y})$ is on the stability boundary $\partial A(u_s,w_s,x_s,y_s)$ of the reduced-state model in (1.6) if and only if the equilibrium point $(\bar{u},\bar{w},\bar{x},\bar{y},0)$ is on the stability boundary of $\partial A(u_s,w_s,x_s,y_s,0)$ of the original model in (1.5).

(D3) It is computationally feasible to detect efficiently the point at which the projected fault-on trajectory $(u(t), w(t), x(t), y(t))$ intersects the stability boundary $\partial A(u_s, w_s, x_s, y_s)$ of the post-fault reduced-state model.

These static and dynamic properties allow the BCU method to compute the CUEP of the original model (1.5) by computing the CUEP of the artificial, reduced-state model (1.6). The BCU method then relates the CUEP of the reduced-state model to the CUEP of the original model. There are several ways to numerically implement the conceptual network-preserving BCU method described in [6]. The following numerical BCU method is implemented and used extensively in this thesis.

A Numerical BCU Method ([6] p.301)

Step 1: Construct a numerical energy function $W_{num}(u, w, x, y, z)$ for the original post-fault system:

$$W_{num}(u, w, x, y, z) = \frac{1}{2} z^T M z + U_{num}(u, w, x, y) \tag{1.7}$$

where the scalar function $U_{num}(u, w, x, y)$ is the numerical energy function for the reduced-state model.

Step 2: From the fault-on trajectory $(u(t), w(t), x(t), y(t), z(t))$ of the original system, detect the exit point $(u^*, w^*, x^*, y^*, z^*)$ at which the projected trajectory $(u(t), w(t), x(t), y(t))$ reaches the first local maximum of the numerical potential energy function $U_{num}(u, w, x, y)$.

Step 3: Use the point (u^*, w^*, x^*, y^*) as the initial condition and integrate the post-fault, reduced-state system (1.6) to the first local minimum of the norm of the post-fault, reduced-state system. Let the local minimum be $(u_0^*, w_0^*, x_0^*, y_0^*)$

Step 4: Use the point $(u_0^*, w_0^*, x_0^*, y_0^*)$ as the initial guess to solve the following set of nonlinear algebraic equations. Let the solution be $(u_{C0}^*, w_{C0}^*, x_{C0}^*, y_{C0}^*)$.

$$\begin{aligned} &\left\| \frac{\partial U}{\partial u}(u, w, x, y) + g_1(u, w, x, y) \right\| \\ &+ \left\| \frac{\partial U}{\partial w}(u, w, x, y) + g_2(u, w, x, y) \right\| \\ &+ \left\| \frac{\partial U}{\partial x}(u, w, x, y) + g_3(u, w, x, y) \right\| \\ &+ \left\| \frac{\partial U}{\partial y}(u, w, x, y) + g_4(u, w, x, y) \right\| = 0 \end{aligned} \tag{1.8}$$

Step 5: The CUEP relative to the fault-on trajectory $(u(t), w(t), x(t), y(t), z(t))$ of the original model is $(u_{C0}^*, w_{C0}^*, x_{C0}^*, y_{C0}^*, 0)$.

Step 6: The critical energy v_{cr} is the numerical energy function value at CUEP, $v_{cr} = W_{num}(u_{C0}^*, w_{C0}^*, x_{C0}^*, y_{C0}^*, 0)$.

Step 7: Calculate the numerical energy function at the time of fault clearance t_{cl} using the fault on trajectory $v_f = W_{num}(u(t_{cl}), w(t_{cl}), x(t_{cl}), y(t_{cl}), z(t_{cl}))$.

Step 8: If $v_f < v_{cr}$ then the post-fault trajectory is considered stable. Otherwise, it may be unstable.

1.2.2 An illustrative example

Consider a network-preserving model of the 3-machine WSCC9 system [2], with constant impedance load model and a uniform damping of 0.1. The contingency being considered is where bus 8 is shorted during the fault-on stage, and line 8-7 is tripped to clear the fault. The state variables are machine rotor angles and speeds $(\delta_1, \delta_2, \delta_3, \omega_1, \omega_2, \omega_3)$. The network or algebraic variables are terminal bus voltage magnitudes and angles $(V_1, ..., V_9, \theta_1, ..., \theta_9)$. Figure 1.2 shows the stability region (on the $\omega = 0$ intersection plane) of the original system along with the pre-fault SEP, post-fault SEP and the UEPs on the stability boundary. Figure 1.3 shows the stability region of the artificial, reduced-state system along with the same set of SEPs and UEPs. The locations of pre-fault and post-fault SEPs of both original and reduced-state system are listed in Table 1.1.

Table 1.1: Pre-fault SEP and Post-fault SEP of original and reduced-state systems

	Original system	Reduced-state system
	$\begin{pmatrix} \delta_1, \delta_2, \delta_3, \omega_1, \omega_2, \omega_3 \\ V_1, ..., V_9, \theta_1, ..., \theta_9 \end{pmatrix}$	$\begin{pmatrix} \delta_1, \delta_2, \delta_3, \omega_1, \omega_2, \omega_3 \\ V_1, ..., V_9, \theta_1, ..., \theta_9 \end{pmatrix}$
Pre-fault SEP	(-0.048,0.125,0.112,0.0,0.0,0.0, 1.1,1.097,1.087,1.094,1.072, 1.084,1.1,1.089,1.1,-0.093,-0.008, -0.036, -0.136,-0.174,-0.163, -0.077,-0.114,-0.083)	(-0.048,0.125,0.112,1.1,1.097, 1.087,1.094,1.072,1.084,1.1, 1.089,1.1,-0.093,-0.008,-0.036, -0.136,-0.174,-0.163,-0.077, -0.114,-0.083)
Post-fault SEP	(-0.065,0.243,-0.002, 0.0,0.0,0.0, 1.093,1.094,1.054,1.080,1.055, 1.062,1.095,1.023,1.057,-0.105, 0.113,-0.153,-0.143,-0.136,-0.209, 0.044,-0.282,-0.202)	(-0.065,0.243,-0.002,1.093, 1.094,1.054,1.080,1.055, 1.062,1.095,1.023,1.057,-0.105, 0.113,-0.153,-0.143,-0.136,-0.209, 0.044,-0.282,-0.202)

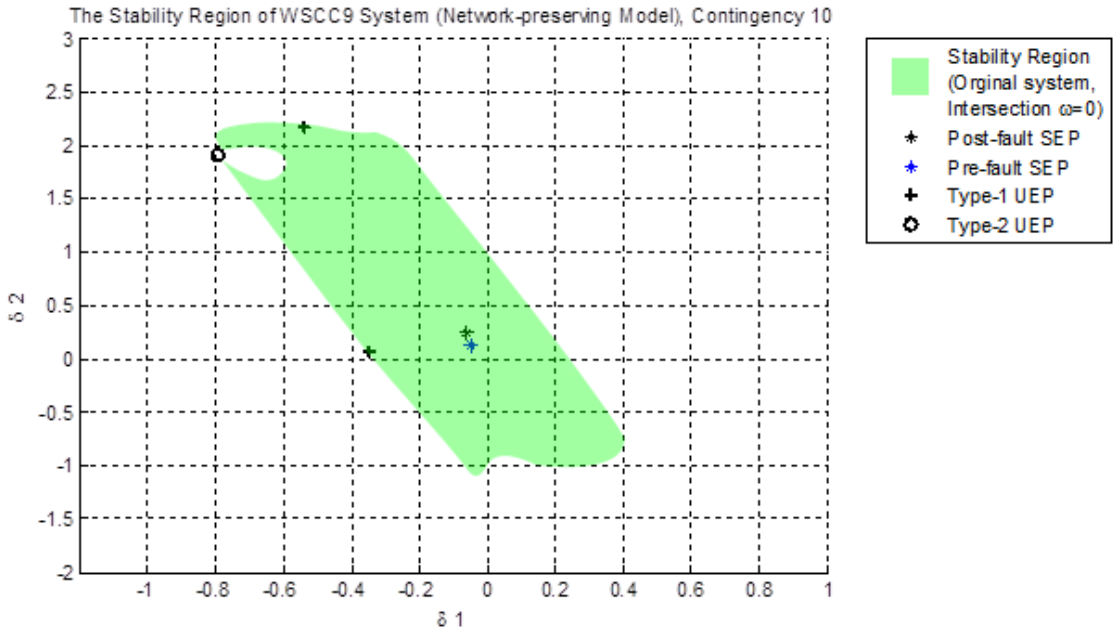

Figure 1.2 The stability region of the WSCC9 system (original system) on the intersection plane of $\omega = 0$. Post-fault SEP, pre-fault SEP, and UEP on the stability boundary are also included.

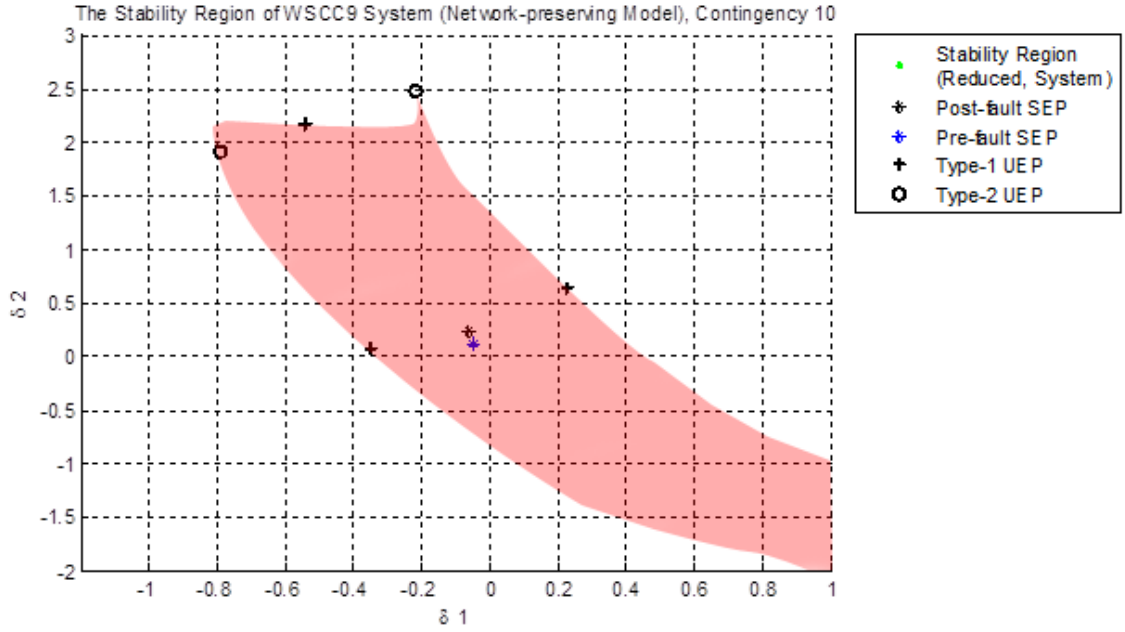

Figure 1.3 The stability region of the WSCC9 system (reduced-state system) on the intersection plane of $\omega = 0$. Post-fault SEP, pre-fault SEP, and UEP on the stability boundary are also included.

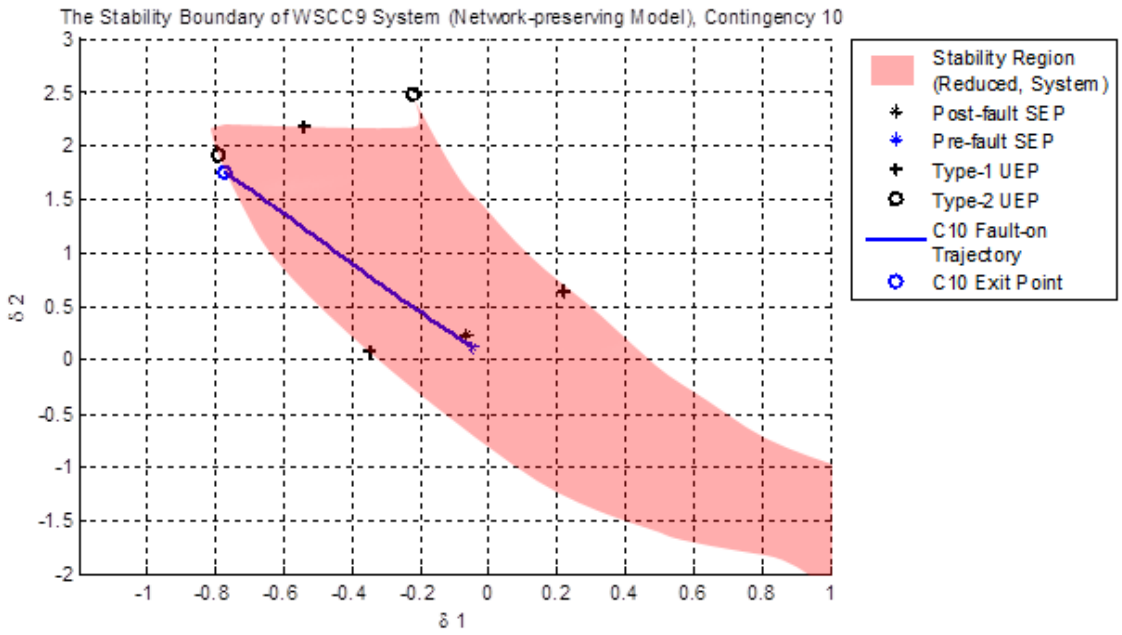

Figure 1.4 The fault-on trajectory and the exit-point of the WSCC9 system with respect to contingency 10 (Fault bus: 8, Tripped line: 8-7).

The first step of the numerical BCU method is to integrate along the fault-on trajectory and locate an exit-point on the stability boundary of the reduced system, as shown in Figure 1.4. The exit point is computed by locating the first local maximum of the numerical energy function of the reduced-state system along the fault-on trajectory. It is illustrated in Figure 1.4 that the exit point in this example is very close to the actual point where the projected fault-on trajectory exits the stability region of the reduced-state system.

After the exit point is obtained, a short numerical integration is performed to locate the minimum gradient point (or MGP). The MGP corresponds to the point along the trajectory with the lowest norm value of the post-fault, reduced-state system. Figure 1.5 illustrates the process of finding MGP in the BCU method. It also shows that the trajectory moves towards a type-1 UEP on the stability boundary of the post-fault SEP.

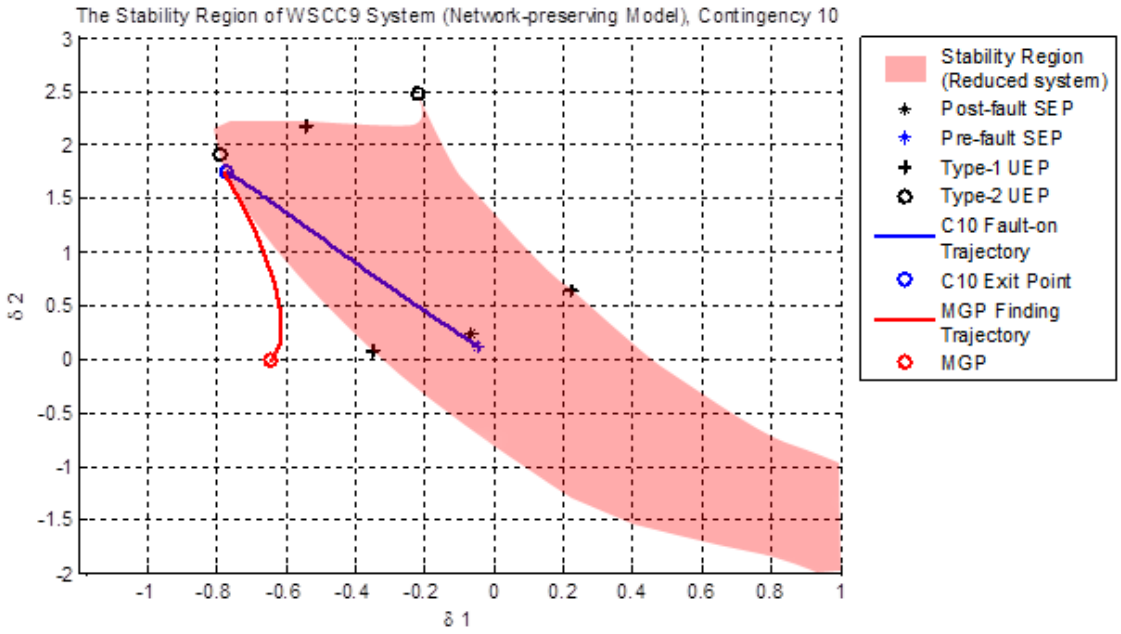

Figure 1.5 The fault-on trajectory, the exit-point and the MGP finding path of the WSCC9 system with respect to contingency 10 (Fault bus: 8, Tripped line: 8-7).

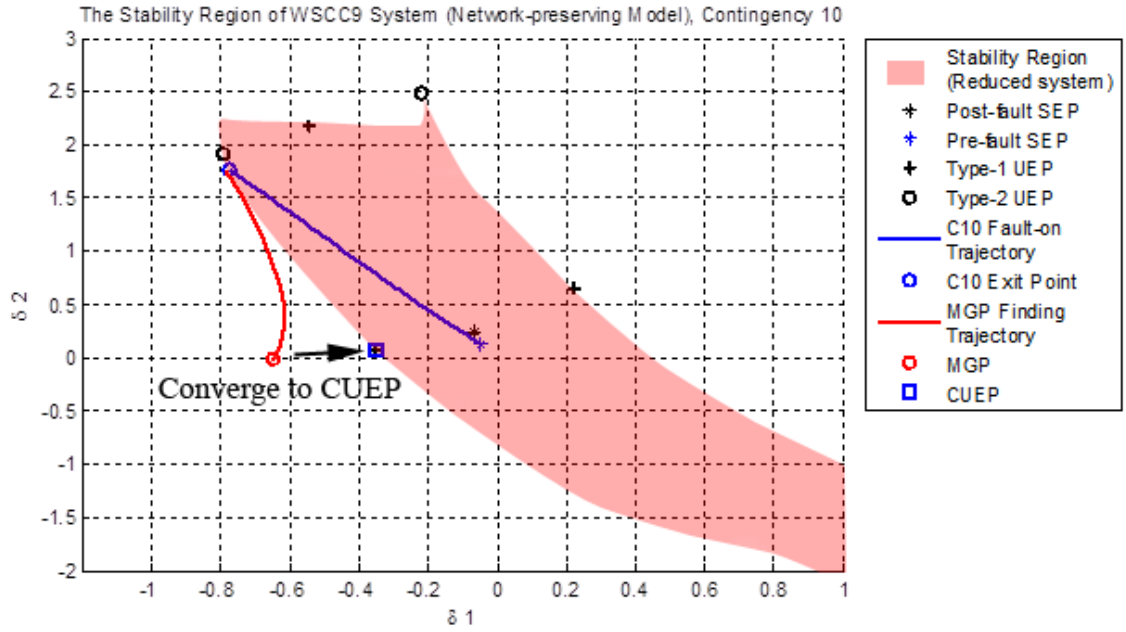

Figure 1.6 The fault-on trajectory, the exit-point, the MGP finding path, and CUEP convergence of the WSCC9 system with respect to contingency 10 (Fault bus: 8, Tripped line: 8-7).

After the MGP has been computed, it is then used as an initial guess for a local solver to compute for the controlling unstable equilibrium point or CUEP of the reduced-state system, see Figure 1.6. Once the CUEP has been found, the direct transient stability assessment can be made based on the critical energy function value at the CUEP, as described previously in the numerical BCU method.

1.3 Contributions of this Thesis

This thesis work contributes mainly to the analysis, applications and extended development of the BCU methods:

- Illustrate the theoretical foundations of the CUEP method for network-preserving power system models via the visualization of stability regions.
- Extend and implement a BCU-based method for power systems with dynamic load models. Construct a numerical energy function for network-preserving power system models with induction motors.
- Develop a CUEP-based control scheme and algorithms to enhance power system transient stability via generation rescheduling of critical machines. Demonstrate empirically that the schemes are effective and robust on practical test systems.
- Propose exact and CUEP-based methods for computing accurate system threshold values. Use the proposed methods to evaluate the discretization-based TSCOPF methods.
- Demonstrate that the current fixed-threshold proxi used in TSCOPF is inaccurate and may cause both underestimate and overestimate assessment. Emphasize the importance of adjusting the threshold values based on the actual system dynamics.

- Establish a stability-region framework in the area of transient stability constrained optimization power flow (TSCOPF). Propose a more accurate TSCOPF formulation based on the stability-region framework.
- Develop a novel BCU-based TSCOPF algorithm for large-scale power systems with transient stability constraints. The method is capable of solving large-scale TSCOPF problems with large contingency lists.
- Apply the above mentioned BCU-based TSCOPF method and CUEP-based enhancement control scheme to practical power system cases.

1.4 Organization of this Thesis

Figure 1.7 shows the organization chart of this thesis. There are three main parts in this thesis, which are i) analysis, ii) methods, and iii) extensions. The analysis part consists of Chapter 2, 5 and 7. Chapter 2 presents the illustrations and numerical results for the CUEP method for DAE systems. Chapter 5 analyzes the accuracy of transient stability constraints in TSCOPF, and proposes a stability-region framework for TSCOPF formulation. In Chapter 7,

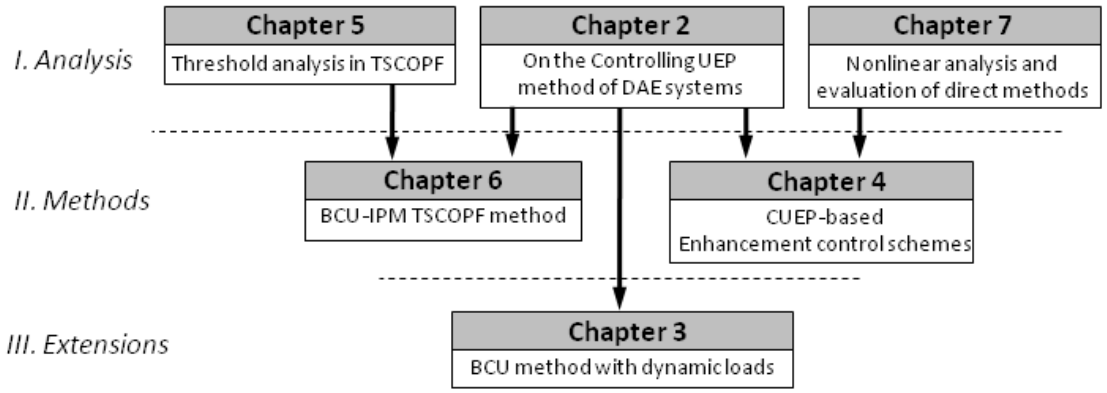

Figure 1.7 Organization chart of this thesis. The three main parts (analysis, methods, and extensions) are illustrated.

nonlinear analysis and critical evaluation of direct methods are performed using the proposed CUEP-based visualization technique and time-domain simulations. The methods part consists of Chapter 4 and 6 where BCU-based methods are developed for transient stability enhancement control and TSCOPF problems in power systems. In Chapter 4, a CUEP-based control scheme for direct enhancement of power system transient stability via generation rescheduling of critical machines are proposed. Chapter 6 presents the proposed novel BCU-based TSCOPF method for solving large-scale TSCOPF problems with large contingency lists. A direct extension and implementation of the BCU method to include dynamic loads is presented in Chapter 3. All proposed methods are tested and applied on practical test systems. Finally, the thesis is concluded in Chapter 8 with proposals for future research directions.

CHAPTER 2

On the Controlling UEP Method and Stability Regions of DAE Systems

The controlling unstable equilibrium point (CUEP) method is a reliable direct method for stability analysis of electrical power systems [6]. The foundations of the CUEP method, initially developed for network-reduced power system models, have been extended to network-preserving power system models, which are represented by a set of differential-algebraic equations (DAEs) [6]. The network-preserving CUEP method explores the relationship between the stability boundary of DAE systems and those of their associated singularly perturbed systems (SPS). In this chapter, the network-preserving CUEP method is numerically evaluated with the focus of characterizing relevant stability regions of DAE system.

2.1 Introduction

The CUEP method has been recognized as a viable and reliable direct method for stability analysis of electrical power systems [6, 7]. Roughly, the CUEP method computes the unstable equilibrium point that is in the "direction" of the fault-on trajectory to obtain a good estimation of the relevant part of the stability boundary and consequently of the critical clearing time (CCT).

The basis for the foundations of the CUEP method is the theory of stability region for nonlinear dynamical systems represented by a set of ordinary differential equations (ODEs) [9]. These foundations led to a precise definition of CUEP, which guarantees the conservativeness of the results, i.e. the estimated CCT is always smaller than the real CCT.

The foundations of the CUEP method were initially developed for network-reduced power system models [7]. In network-reduced models, loads are represented as constant impedance and the algebraic equations of the network are reduced. Consequently, network-reduced models are composed of a set of ODEs. The CUEP, for these models, is defined as the unstable equilibrium point (UEP) whose stable manifold is intersected by the sustained fault-on trajectory.

Network-reduced models were used in the early development of direct methods for transient stability analysis [6]. However, the necessity of considering comprehensive models of loads and generation, including power grids with dynamic loads and renewable energy, requires the preservation of the network in these analyses, see [57], for example, for the inclusion of DC lines. The network-preserving CUEP method has been extended in [6].

2.2 Problem Formulation

In transient stability analysis, power system dynamic models go through three stages: pre-fault stage, fault-on stage and post-fault stage. The dynamics of the pre-fault system (2.1), fault-on system (2.2) and post-fault system (2.3) are all modeled by different sets of differential algebraic equations (DAEs):

$$\begin{cases} \dot{x} = f_{pre}(x, y) \\ 0 = g_{pre}(x, y) \end{cases} \qquad t \in (-\infty, 0) \tag{2.1}$$

$$\begin{cases} \dot{x} = f_{f}(x, y) \\ 0 = g_{f}(x, y) \end{cases} \qquad t \in [0, t_{cl}) \tag{2.2}$$

$$\begin{cases} \dot{x} = f(x, y) \\ 0 = g(x, y) \end{cases} \qquad t \in [t_{cl}, \infty) \tag{2.3}$$

where $x \in R^n$ and $y \in R^m$ are the corresponding dynamic and static variables of the systems, respectively. The system undergoes a disturbance at $t = 0$ and the protection system is activated to clear the fault at $t = t_{cl}$. The DAE system (2.3) can be interpreted as an implicitly dynamic system defined on the constraint manifold Γ:

$$\Gamma = \{(x, y) : g(x, y) = 0\} \tag{2.4}$$

All the equilibrium points, stable and unstable manifolds, and stability regions must lie in the above constraint manifold. We note that the constraint manifold of the pre-fault, fault-on and post-fault systems are different. We will respectively denote them by Γ_{pre}, Γ_f and Γ.

Typically, the constraint manifold is composed of several disjoint connected components. In each connected component Γ_i, the number of eigenvalues of $D_z g$ on the right-half of the complex plane is constant. Therefore, it makes sense to define a type of stability for each component Γ_i with respect to the fast dynamics. If all the eigenvalues of $D_z g$ calculated at points of Γ_i have a negative real part, then we call Γ_i a stable component of Γ. Otherwise, it is called an unstable component.

Usually the system is operating at an asymptotically stable equilibrium point (x_0, y_0) of the pre-fault system. At time $t = 0$, the system undergoes a perturbation and the trajectory jumps instantaneously from $(x_0, y_0) \in \Gamma_{pre}$ to a point $(x_0, y_0^+) \in \Gamma_f$. For the fault-on trajectory, along the fault-on constraint manifold Γ_f, we will use the notation $z_f(t) = \left(x_f(t), y_f(t)\right)$. At the clearing time t_{cl}, trajectory instantaneously jumps from $z_f(t_{cl}) = \left(x_f(t_{cl}), y_f(t_{cl})\right)$ on the fault-on manifold Γ_f to a point $z^+(t_{cl}) = \left(x(t_{cl}), y^+(t_{cl})\right)$ on the post-fault manifold Γ.

These jump behaviors are a modeling problem that arises as a consequence of neglecting some parasitic or fast dynamics. This problem has been fixed using the singular perturbation approach [58] . The singular perturbation approach treats the set of algebraic equations describing a DAE system as a limit of the fast dynamics: $\varepsilon \dot{y} = g(x, y)$. In other words, as ε approaches zero, the fast dynamics will approach its constraint manifold. In this way, the jumps will be associated with the limit, as ε approaches zero, of very fast dynamics.

Therefore, for the DAE system (2.3), we can define an associated SPS:

$$\begin{aligned} \dot{x} &= f(x, y) \\ \varepsilon \dot{y} &= g(x, y) \end{aligned} \tag{2.5}$$

where ε is a sufficiently small positive number. The state variables of system (2.5) have very different rates of dynamics and they can be separated into two distinct time scales: slow variable $\boldsymbol{x}$ and fast variable $\boldsymbol{y}$.

Note that trajectories of the SPS (2.5) will not be confined to the constrained manifold Γ and are not exactly the same as those of the original DAE system (2.3). However, trajectories generated by the SPS are still valid approximations as opposed to those of the DAE system. A theoretical justification to ensure that the difference of solution trajectories between the original DAE (2.3) and the singularly perturbed system (2.5) is uniformly bounded by the order of $O(\varepsilon)$ is provided by the Tikhonov's theorem over the infinite time interval [59].

2.3 CUEP for DAE Systems

The concept of a controlling UEP is well defined for network-reduced power system models described by ODEs. The controlling UEP of a fault-on trajectory is the UEP whose stable manifold contains the *exit point*, i.e. the point at which the fault-on trajectory intersects the stability boundary and leaves the stability region.

One key difficulty in extending the concept of the controlling UEP to network-preserving power systems modeled by DAEs is that the fault-on trajectory will not lie on the constraint manifold of its post-fault DAE system, making the task of defining exit point and controlling UEP for DAE systems difficult. Since the fault-on trajectory does not belong to the constraint manifold of the post-fault DAE system, the fault-on trajectory does not reach the stability boundary of the post-fault DAE system. Thus, the exit point of the DAE trajectory cannot be defined as the point of intersection between the fault-on trajectory and the stability boundary of the post-fault system, which lies on a different constraint manifold.

Two approaches are developed to overcome this issue. One approach is to exploit the SPS associated with the DAE system and define the controlling UEP of this DAE system as the controlling UEP of the associated singularly perturbed system. In this case, the fault-on trajectory will intersect the stability boundary of the corresponding singularly perturbed post-fault system and hence the controlling UEP of the singularly perturbed system is well defined.

Definition 2.3.1 (CUEP for singularly perturbed model) [61] The controlling UEP of the singularly perturbed model (2.5) for a fixed small $\varepsilon > 0$ with respect to a fault-on trajectory is the UEP on the stability boundary $\partial A_\varepsilon(x_s, y_s)$ of the singularly perturbed post-fault system (2.5), whose stable manifold contains the exit point of the fault-on trajectory.

This definition is based on the fact that the exit point must lie on the stable manifold of some UEP on the stability boundary of the singularly perturbed post-fault model (2.5). By exploiting the complete characterization of the stability boundary of the singularly perturbed

post-fault system (2.5), one can prove the existence and uniqueness of the controlling UEP of the singularly perturbed model (2.5).

Now, it is needed to establish a relationship between the controlling UEP of the SPS (2.5) and the controlling UEP of the DAE system (2.3). In other words, it is desirable to study the behavior of the controlling UEP for the SPS (2.5) when $\varepsilon \to 0$. This requirement leads to the following definition of a uniform controlling UEP.

Definition 2.3.2 (Uniform Controlling UEP) [61] Let $(x_{co}^{\varepsilon}, y_{co}^{\varepsilon})$ be the controlling UEP of the singularly perturbed post-fault system (2.5) with respect to the fault-on trajectory $(x_f^{\varepsilon}(t), y_f^{\varepsilon}(t))$. Consider the map $\varepsilon \to (x_{co}^{\varepsilon}, y_{co}^{\varepsilon})$. If there exist an $\varepsilon^* > 0$ such that the map is constant for all $\varepsilon \in (0, \varepsilon^*)$, then $(x_{co}^{0}, y_{co}^{0}) = (x_{co}^{\varepsilon}, y_{co}^{\varepsilon})$ is a uniform controlling UEP with respect to the fault-on trajectory $(x_f^{\varepsilon}(t), y_f^{\varepsilon}(t))$ for all $\varepsilon \in (0, \varepsilon^*)$.

The controlling UEP of the SPS with respect to a fault-on trajectory may alter due to the change of ε. However, the CUEPs of SPS are generically uniform. This property not only allows us to define the controlling UEP of DAE systems via the controlling UEP of the singularly perturbed system, but also provides a way to compute the controlling UEP of the DAE system with the aid of the associated singularly perturbed system.

Definition 2.3.3 (Controlling UEP for DAE systems # 1) [61] The controlling UEP of a DAE system (2.3) with respect to a fault-on trajectory is the uniform controlling UEP of the associated SPS (2.5).

Definition 2.3.4 (Relevant stability boundary) [61] The relevant stability boundary with respect to a projected fault-on trajectory is the stable manifold of the controlling UEP of the DAE system.

An alternative definition for the CUEP of DAE systems exploits the concept of projected fault-on trajectory. For each point $(x_f(t), y_f(t))$ of the fault-on trajectory, we define a projected point on the post-fault constraint manifold denoted by $(x_f(t), y_p(t))$ such that $(x_f, y_p) \in \Gamma$ and $g(x_f, y_p) = 0$. Since the projected fault-on trajectory lies on the constraint manifold of the post-fault system, we can define the exit point of a DAE system with respect to a DAE fault-on trajectory as the point at which the projected fault-on trajectory intersects the stability boundary of the post-fault DAE system.

Definition 2.3.5 (Exit point) [61] The point at which a (sustained) projected fault-on DAE trajectory intersects the stability boundary of a post-fault DAE system is termed the exit point of the fault-on DAE trajectory (relative to the post-fault DAE system).

With the definition of the exit point for a DAE system, we next present an alternative definition of controlling UEP of DAE trajectories.

Definition 2.3.6 (Controlling UEP of DAE systems # 2) [61] The controlling UEP of a fault-on DAE trajectory is the UEP of the post-fault DAE system whose stable manifold intersects the projected fault-on DAE trajectory at the exit point.

Assuming that the jump behavior of the switched DAE systems can be approximately modeled by the fast dynamics of the associated SPS, the next theorem shows that both definitions of controlling UEP for DAE systems are equivalent.

Theorem 2.3.1 (Equivalence between the two definitions of CUEP) [61] Suppose (x_{co}, y_{co}) is the controlling UEP of the DAE system (2.3), with respect to a projected fault-on trajectory $(x_f(t), y_p(t))$, then (x_{co}, y_{co}) is the uniform controlling UEP of the singularly perturbed system SPS (2.5).

2.4 Numerical Simulation Results

We next illustrate the theoretical developments derived so far in this chapter on two simple examples.

2.4.1 Example 1 [62,63]

The following dynamical system represent a simple power system with single generator and one load.

$$\begin{aligned} \dot{\omega} &= -\frac{1}{M_g} D_g \omega - \frac{1}{M_g} f(\alpha, V) \\ \dot{\alpha} &= -\frac{1}{D_l} f(\alpha, V) + \omega \\ 0 &= -g(\alpha, V) \end{aligned} \tag{2.6}$$

where $f(\alpha,V) = B_{12} V \sin\alpha - P_l$ and $g(\alpha,V) = \frac{1}{V}(Q_l - B_{12} V \cos\alpha - B_{22} V^2)$

For the following set of parameters: M_g = 20, D_g = 9, D_l = 50, P_l = 4, Q_l = -0.5, B_{12} = 10 and B_{22} = -10, system (2.6) possesses the stable equilibrium point (0,0.4291,0.9613) and the

following two unstable equilibrium points (0, 1.2660, 0.4193) and (0, -5.0172, 0.4193). These equilibrium points lie on the constraint manifold $\Gamma = \{(\omega, \alpha, V) : g(\alpha, V) = 0\}$. Figure 2.1 illustrates a stable component of this constraint manifold, which contains these 3 equilibrium points. Both unstable equilibrium points lie on the stability boundary of the stable equilibrium point. The stability boundary is composed of the union of the stable manifolds of these two UEPs, as indicated in Figure 2.1. The system is operating at the stable equilibrium point when it undergoes a short-circuit on the load bus.

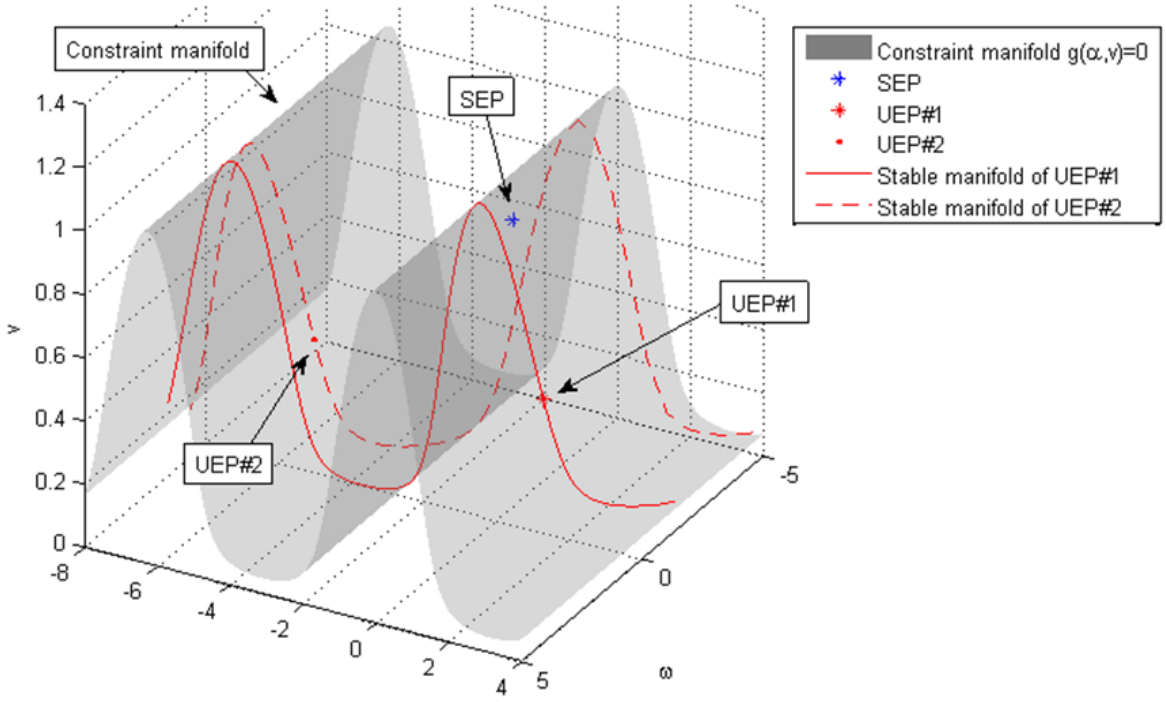

Figure 2.1 The constraint manifold of the DAE system (2.6). Both unstable equilibrium points (0, 1.2660, 0.4193) and (0, -5.0172, 0.4193), marked in red, lie on the stability boundary of the stable equilibrium point (0,0.4291,0.9613), marked in blue.

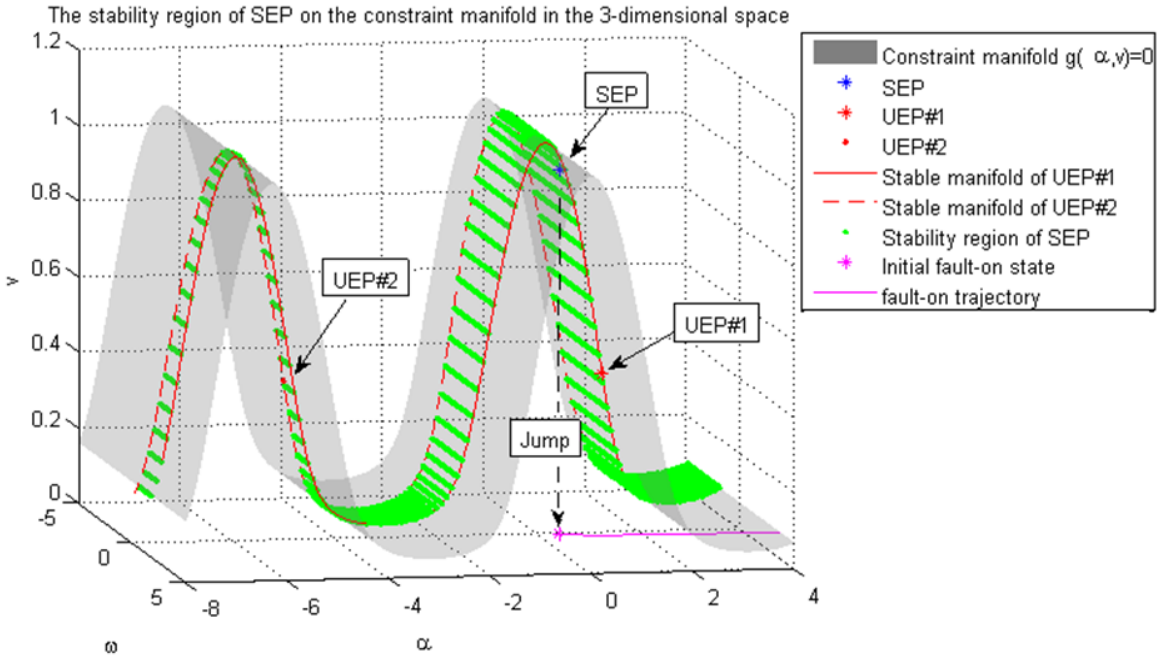

Figure 2.2 The fault-on trajectory of the DAE system (2.7). The fault trajectory travels along the constraint manifold of the fault-on system, which differs from the constraint manifold of the post-fault system.

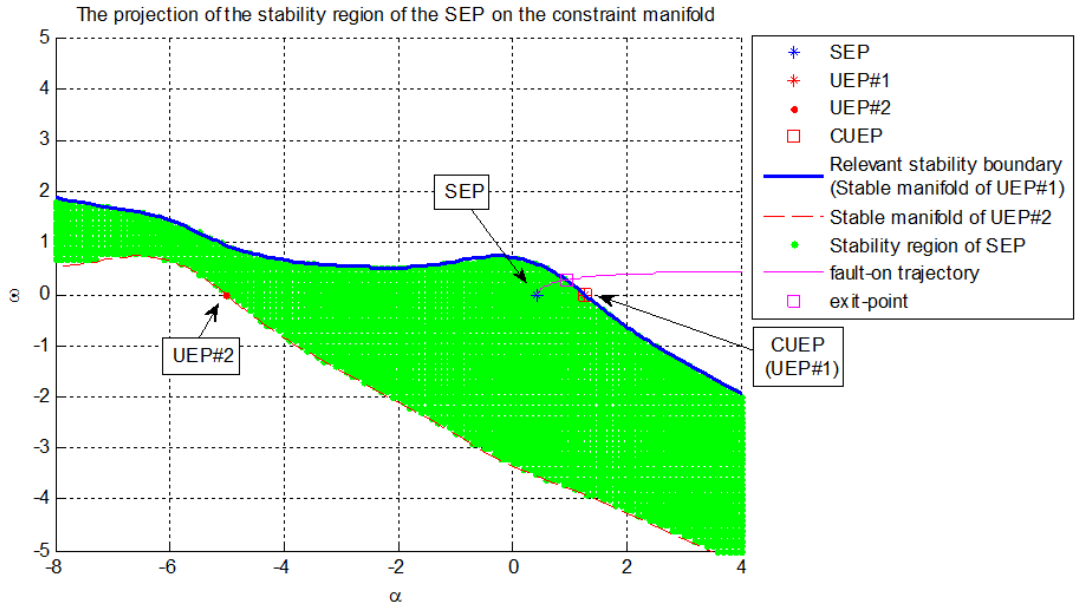

Figure 2.3 The projected fault-on trajectory of the DAE system (2.7) along the constraint manifold of the post-fault system (2.6)

The fault-on system dynamics are governed by the following set of differential algebraic equations:

$$\begin{aligned} \dot{\omega} &= -\frac{1}{M_g} D_g \omega - \frac{1}{M_g} f(\alpha, V) \\ \dot{\alpha} &= -\frac{1}{D_l} f(\alpha, V) + \omega \\ 0 &= V \end{aligned} \tag{2.7}$$

We assume that the post-fault system is equal to the pre-fault system. The constraint manifold of the fault-on system is the plane $\omega\alpha$. The disturbance trajectory instantaneously jumps on this manifold and travels along it. Figure 2.2 illustrates the fault-on trajectory of this system.

The projected fault-on trajectory of the DAE system (2.7) along the constraint manifold of the post-fault system (2.6) is depicted in Figure 2.3, as well as the corresponding exit point and the controlling UEP, which in this case is the UEP (0, 1.2660, 0.4193). The relevant stability region is also highlighted in this figure in a thick blue line. It is composed of the stable manifold of the controlling UEP.

We compare the stability region of the DAE system with the stability region of the corresponding singularly perturbed system with different values of epsilons. The comparison is made on the subspace of (ω, α); i.e. the intersection of the stability region and the subspace. As can be seen from Figure 2.4-Figure 2.7, the stability region of the corresponding singularly perturbed system approaches the stability region of the DAE system as the values of epsilon approaches zero and this observation is in a agreement with our theoretical development. When epsilon gets smaller at the value of 0.005, the stability region of the corresponding singularly perturbed system captures that of the DAE system more accurately as we can see in Figure 2.7.

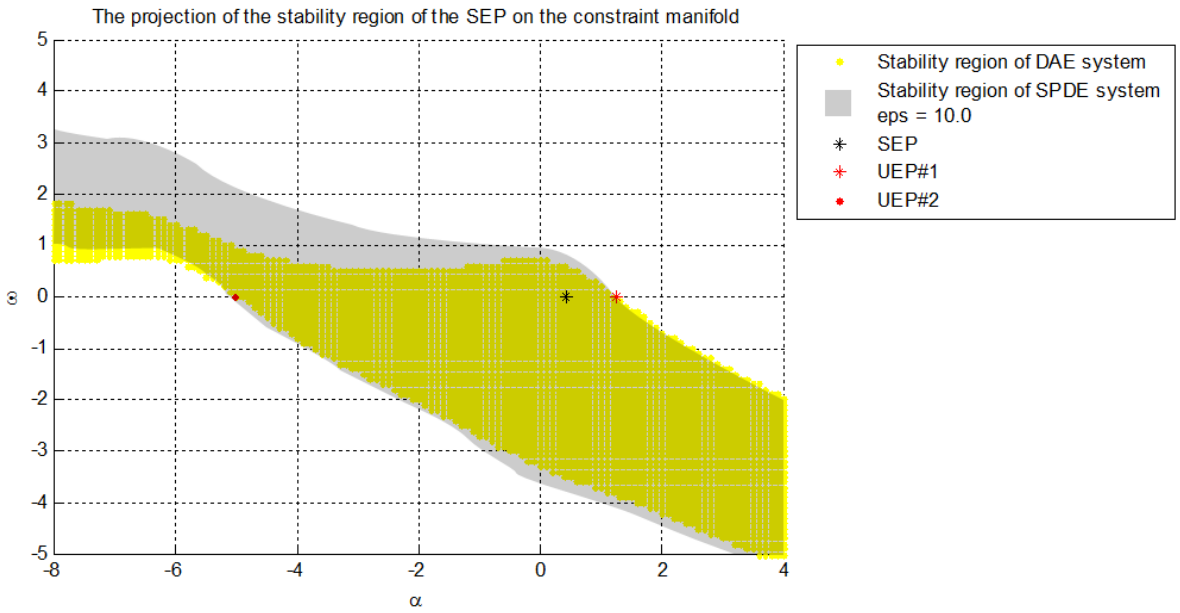

Figure 2.4 An illustration of a large mismatch of the stability regions of DAE and SPS systems when the chosen value of epsilon is too large, eps = 10.

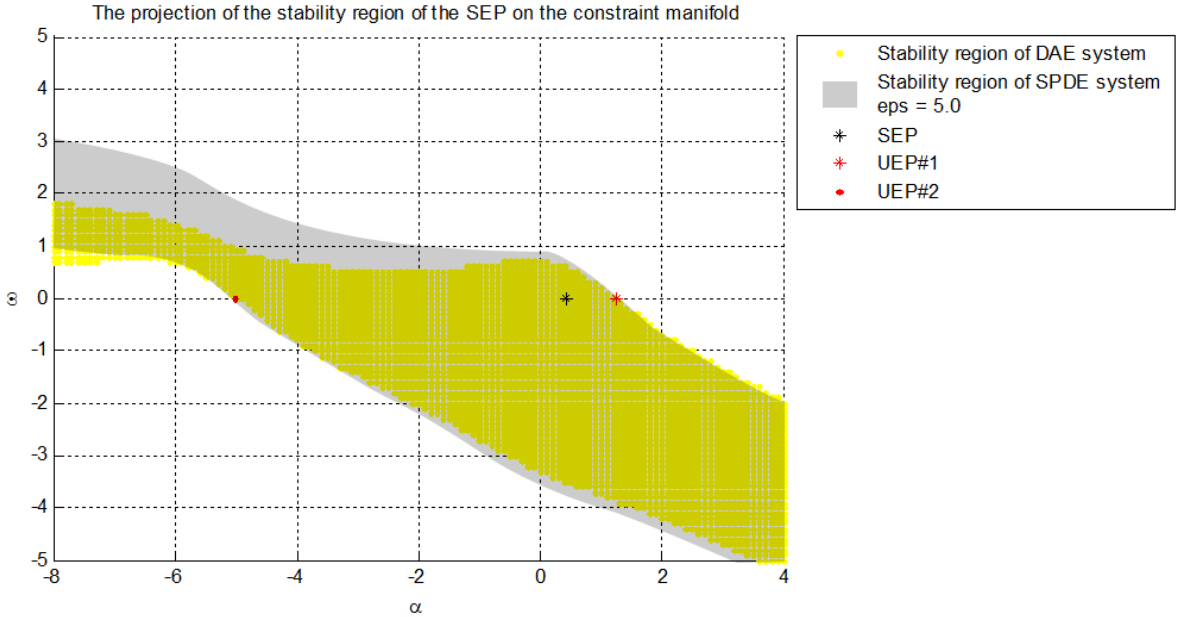

Figure 2.5 The stability region (on $\omega = 0$ and $g(x, y) = 0$) of the singularly perturbed system with epsilon = 5.0 is closer to that of the corresponding DAE system.

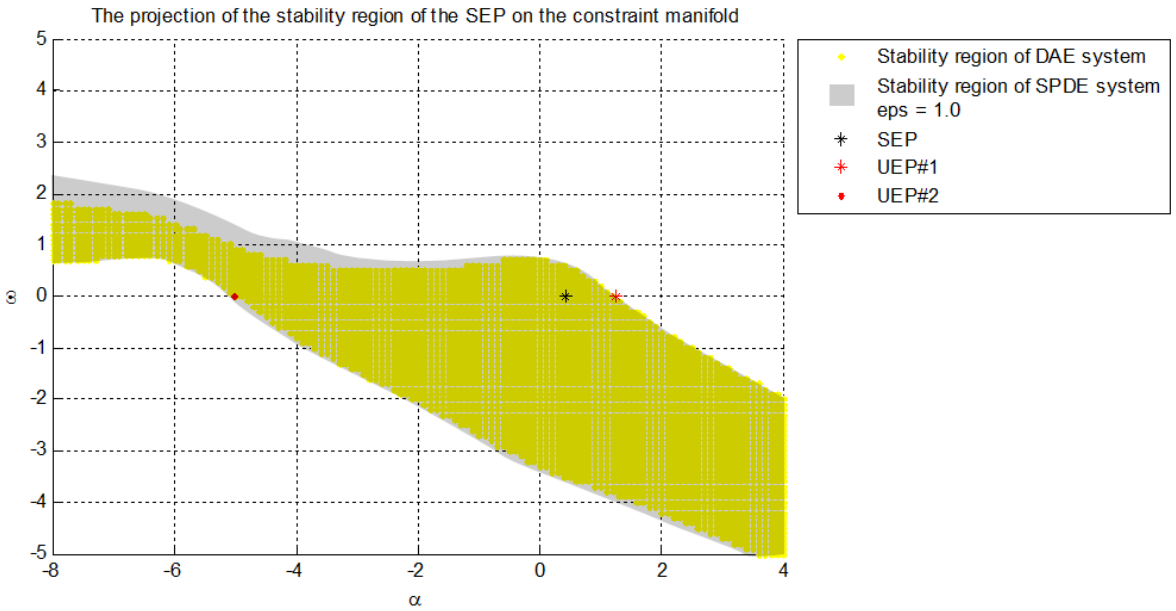

Figure 2.6 The stability region (on $\omega = 0$ and $g(x, y) = 0$) of the singularly perturbed system with epsilon = 1.0 is closer to that of the corresponding DAE system.

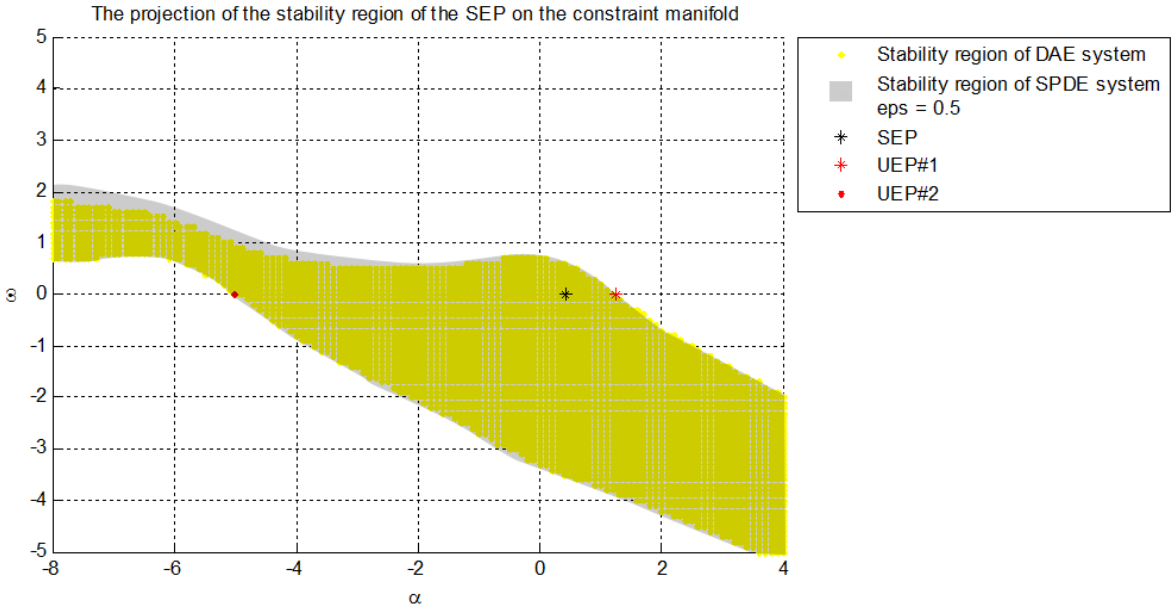

Figure 2.7 The stability region (on $\omega = 0$ and $g(x, y) = 0$) of the singularly perturbed system with epsilon = 0.5 is very close to that of the corresponding DAE system.

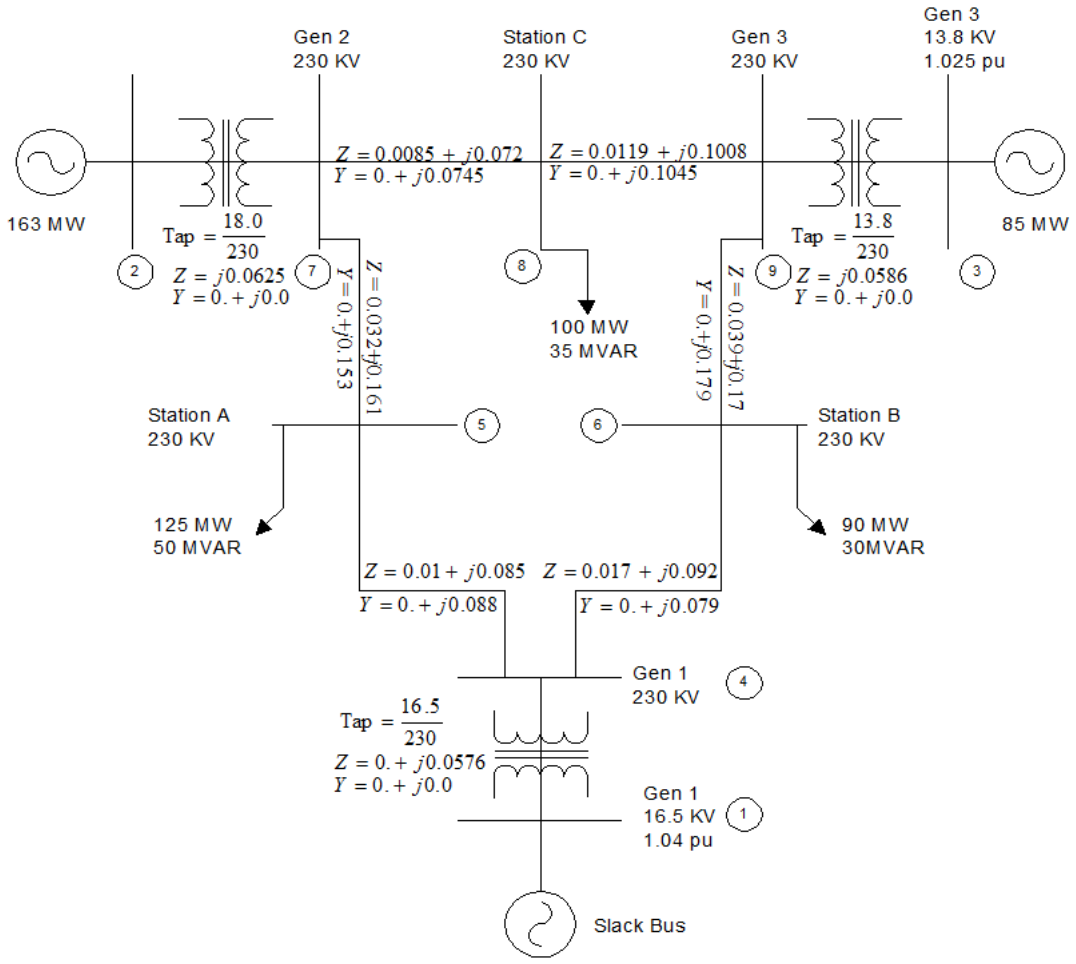

Figure 2.8 The one-line diagram of the (pre-fault) 3-machine, 9-bus system; the value of Y is half the line charging.

2.4.2 Example 2 [2]

Consider the 3-machine, 9-bus system, shown in Figure 2.8, and which is modeled by the DAE system (2.8).

$$\begin{aligned} \dot{\delta}_i &= \omega_i \\ M_i\dot{\omega}_i &= P_{mi} - P_{ei}(\delta,\theta,V) - d_i\omega_i \qquad i = 1,2,3 \\ 0 &= F(\delta,\theta,V) \end{aligned} \tag{2.8}$$

We consider a uniform damping factor $d_i / M_i = 0.1$ with $[d_1, d_2, d_3]$ = [0.0125, 0.0034, 0.0016]. A short-circuit occurs near bus 8 on the line between bus 8 and bus 7 at time 0 seconds for a period of 8 cycles of 60Hz. The system trajectory jumps from the SEP onto the fault-on constraint manifold.

The SEP of the pre-fault system, and the constraint manifold of the fault-on system and that of the post-fault system are depicted in Figure 2.9 and Figure 2.10. During the fault-on period, the fault-on trajectory moves along the fault-on constraint manifold. At the same time, the projected fault-on trajectory moves on a (stable) post-fault constraint manifold, see Figure 2.9 and Figure 2.10.

The projected fault-on trajectory intersects with the stability boundary of the post-fault system at the exit point. The CUEP is the unstable equilibrium point on the stability boundary whose stable manifold contains the exit point, see Figure 2.10. If the fault is cleared before the projected fault-on trajectory intersects with the stability boundary (i.e. the projected fault-on trajectory still lies inside the stability region of the post-fault system), then the fault-on trajectory will jump onto the post-fault constraint manifold and the initial condition of the corresponding post-fault trajectory lies inside the stability region of the post-fault and will converge to the SEP of the post-fault system.

If the fault is cleared after the projected fault-on trajectory intersects with the stability boundary, then the fault-on trajectory will jump onto the post-fault constraint manifold and the initial condition of the corresponding post-fault trajectory lies outside the stability region of the post-fault SEP and, hence it will diverge from the SEP. The CCT estimation obtained via an energy function for the post-fault system is 0.4088s.

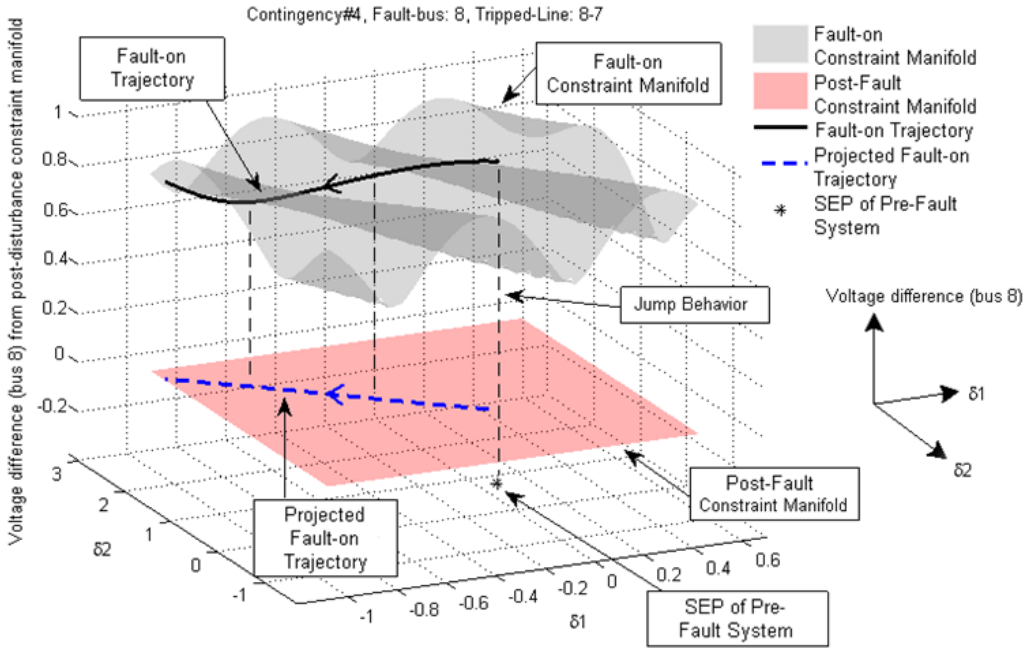

Figure 2.9 After fault occurrence, the system trajectory jumps from the SEP of the pre-fault system into the fault-on constraint manifold. The fault-on trajectory travels on this manifold while the projected fault-on trajectory moves along the post-fault constraint manifold.

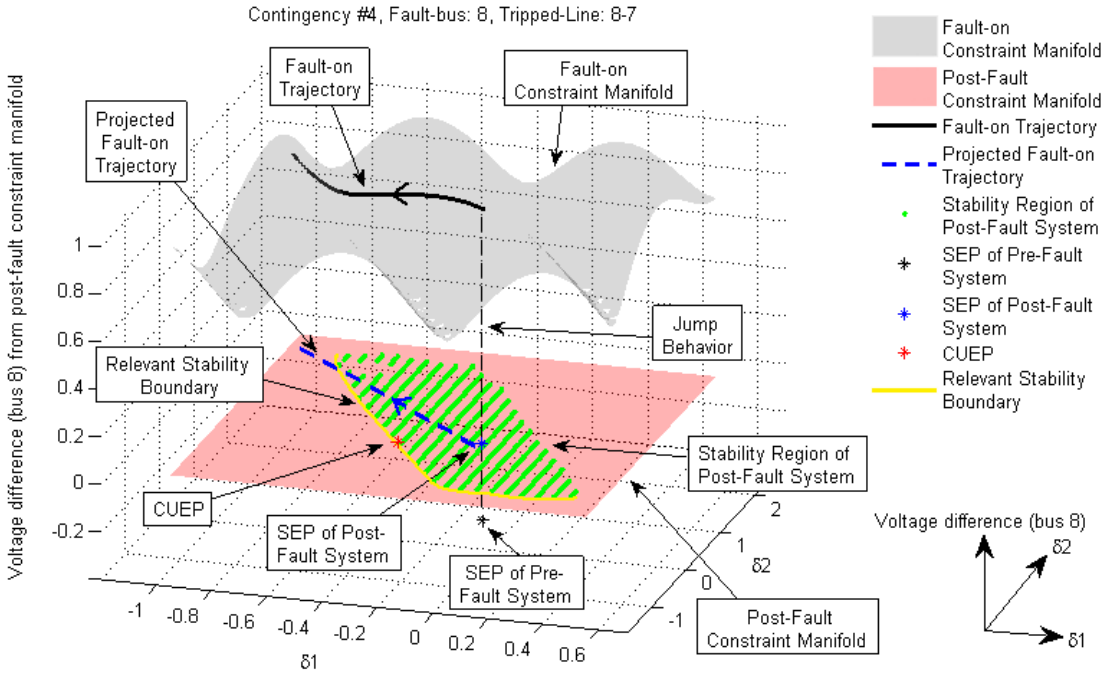

Figure 2.10 The CUEP is the unstable equilibrium point of the post-fault system whose stable manifold is intersected by the projected fault-on trajectory. The relevant stability boundary is the stable manifold of the CUEP.

2.5 Conclusions

The difficulties of defining exit point and CUEP for DAE models were overcome by exploring the relationship between the DAE system and the corresponding singularly perturbed system. A method to compute the CUEP based on a projected fault-on trajectory was illustrated and numerically shown that the CUEP calculated in this form equals the CUEP calculated via the uniform CUEP of the singularly perturbed system. It is expected that the network-preserving CUEP method will play a vital role in the development of direct methods for transient stability analysis of more comprehensive power system models, including those that contain dynamic loads or renewable generation penetration.

CHAPTER 3

Development of the BCU Method for Power System Models with Dynamic Loads

3.1 Introduction

When the BCU method was first developed in [13], it was initially applied to a simple classical model [1] (or network-reduction model) that can be mathematically expressed by a system of nonlinear ordinary differential equations (ODE). With the availability of analytical (for lossless system) [69] and numerical (for lossy system) [6] energy functions for more detailed models, the BCU method was later extended to incorporate network-preserving power system models as shown in [6]. The sound theoretical basis and foundations of the BCU methodology allow this method to be applicable to any power system models, as long as the required static and dynamic properties (Properties S1-S2 and D1-D3 in [6] and [14]) are satisfied. Up to now, several load models such as constant impedance, constant power, constant current, and the composite of the three (or ZIP) have been incorporated into the BCU method. These load models however still cannot be considered as an accurate representation of the real world loads for which 60% of the total power demand typically belongs to induction motors or dynamic loads. Unlike most composite ZIP load models, the response of dynamic loads to voltage and frequency changes may not always be fast, and this may lead to some dynamic behaviors that can only be observed and detected when more comprehensive dynamic load models are included in the system model [76-77]. As a result, it is crucial that the BCU method should be extended further to include dynamic load models.

In this chapter, we developed a BCU method for power systems with dynamic load models (induction motors). Two main tasks are required in this development: (1) the construction of a numerical energy function for power systems with dynamic loads, (2) the derivation and implementation of the corresponding BCU method for power systems with dynamic loads. Section 3.2.1 provides a literature survey on the construction of energy functions and dynamic load modeling for power system transient stability analysis. The electrical circuits and models of the induction motors used in our research are explained in Section 3.2.2. Section 3.2.3 presents a guideline for constructing numerical energy functions and deriving the corresponding BCU method. Section 3.3 contains the complete expression of a network-preserving model with dynamic loads which is later used to construct numerical energy functions for power systems with induction motors. The derivation of the BCU method for power systems with induction motors is given in Section 3.4. The new BCU method is tested on two adapted WSCC9 systems and the numerical results are shown in Section 3.5. Section 3.6 gives the conclusions.

3.2 Preliminaries

3.2.1 Literature survey

The construction of analytical energy functions has been the central problem in the direct transient stability analysis of power systems [3, 4, 5, 47, 72, 75, 76]. The direct methods were initially developed for network-reduction models [1, 13, 49], in which loads are expressed as constant impedances. The network-reduction models however have been heavily criticized for their inaccuracy in capturing actual dynamic behaviors and phenomena in power systems. This is due to the fact that only a constant impedance load model and reduced transmission network can be considered in this model. This consequently leads to an exclusion of the dynamic behaviors at

PQ(load) buses, and the loss of the full network topology. The network-preserving models were proposed in [70] to overcome some of the shortcomings of the network-reduction model. The energy functions for network-preserving model was then developed for both lossless [69] and lossy [6] power systems, and also utilized in energy function-based direct methods [6]. Employing the network-preserving power system models for direct transient stability analysis has the following advantages: (1) it allows more realistic representations of power system components, such as load behaviors, (2) it allows the use of sparse matrix techniques to quickly solve nonlinear algebraic equations involved in direct methods, and (3) it offers a way to physically explain each mathematical term in the energy function [69].

The past research on the construction of an energy function for network-preserving transient stability models can be found in [66, 67, 69, 70, 71] however none of these works considers dynamic loads in the system model. An attempt to construct Lyapunov functions for power systems with dynamic reactive power loads has been made in [73], but it does not consider the dynamics of detailed induction motors. Dynamic loads or induction motors have been shown to have significant effects on the overall system transient stability [76-78]. The modeling and identifications of dynamic loads have been extensively researched in [81, 83, 87-91]. The effect of dynamic loads on power system stability and dynamics was studied in [84-86] which illustrates various phenomena that do not exist in the simpler static load models.

3.2.2 Induction motor models

Three induction motor models are considered in our development of the extended BCU method: (1) a simplified model (Order I model), (2) a squirrel-cage model (Order III model) and (3) a double squirrel-cage model (Order V model). These three models are pure mechanical

models whose equivalent circuits are illustrated in Figure 3.1, Figure 3.2, and Figure 3.3 respectively. More details on each of the induction motor model can be found in [1] and [93]. The Order I model represents an induction motor model in a very simple mathematical form. It is suited for applications in which simplicity of the system model or computational speed is highly prioritized. The Order III model or squirrel-cage is a very common induction motor model. The Order V or double squirrel-cage is a special arrangement that allows higher value of motor efficiency. It will be shown that as the order number increases, the numbers of associated equations and variables for the model also increase.

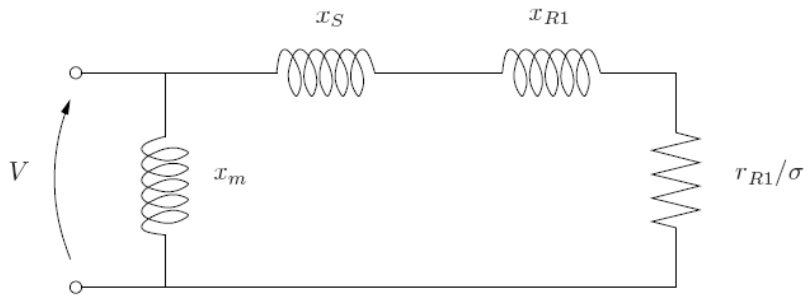

Figure 3.1 Order I induction motor (simplified model): electrical circuit

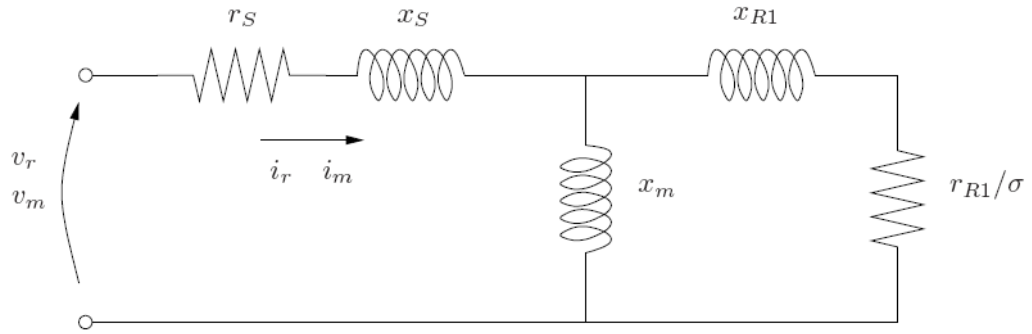

Figure 3.2 Order III induction motor (single or squirrel cage model): electrical circuit

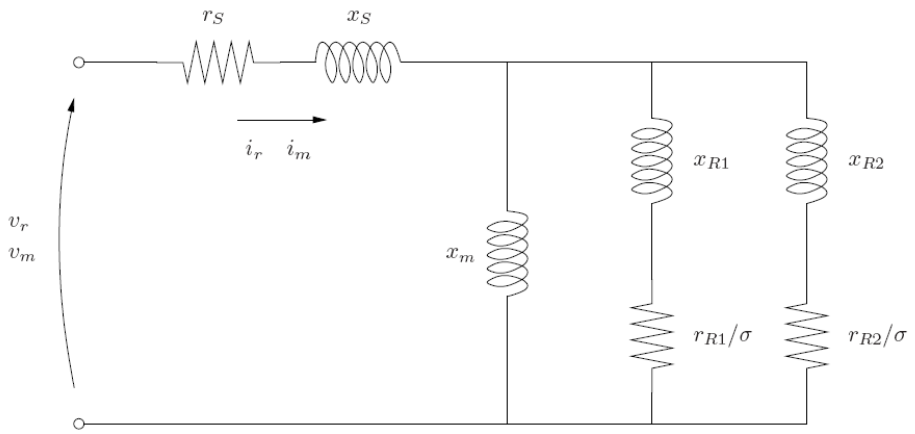

Figure 3.3 Order V induction motor (double squirrel-cage model): electrical circuit

Order I Model (a simplified model)

The following composite load model is the expression used for the torque-speed characteristic [93].

$$T_m = a + b\omega + c\omega^2 \tag{3.1}$$

The torque is slip dependent and the relationship between the slip σ and the angular speed ω in p.u. is $\sigma = 1 - \omega$. We can then express the torque-slip characteristic as follows:

$$T_m = \alpha + \beta\sigma + \gamma\sigma^2 \tag{3.2}$$

where

$$\begin{aligned} \alpha &= a + b + c \\ \beta &= -b - 2c \\ \gamma &= c \end{aligned} \tag{3.3}$$

In the first order induction motor model, only the mechanical state variable, slip σ, is considered and the dynamic of the slip can be described as follows:

$$\dot{\sigma} = \frac{1}{2H_m}\left(T_m(\sigma) - \frac{r_{R1}V^2/\sigma}{\left(r_S + r_{R1}/\sigma\right)^2 + \left(x_S + x_{R1}\right)^2} \right) \tag{3.4}$$

The real and reactive power injections are:

$$P = -\frac{r_{R1}V^2/\sigma}{\left(r_S + r_{R1}/\sigma\right)^2 + \left(x_S + x_{R1}\right)^2}$$
$$Q = -\frac{V^2}{x_m} - \frac{\left(x_S + x_{R1}\right)V^2}{\left(r_S + r_{R1}/\sigma\right)^2 + \left(x_S + x_{R1}\right)^2} \tag{3.5}$$

Order III Model (single or squirrel-cage model)

The equivalent electrical circuit used for the squirrel-cage (Order III) induction motor is presented in Figure 3.2. The equations are formulated in terms of the real (r) and imaginary (m) axis, with respect to the network reference angle. In a synchronously rotating reference frame, the link between the network and the stator machine voltages are as follows [93]:

$$v_r = -V\sin\theta$$
$$v_m = V\cos\theta \tag{3.6}$$

The real and reactive power absorbed by the induction motor are:

$$P = -\left(v_r i_r + v_m i_m\right)$$
$$Q = -\left(v_m i_r - v_r i_m\right) \tag{3.7}$$

The differential equations in terms of the voltage behind the stator resistance r_S can be described as follows:

$$\dot{e}'_r = \Omega_b \sigma e'_m - \left(e'_r + \left(x_0 - x'\right)i_m\right)/T'_0$$
$$\dot{e}'_m = -\Omega_b \sigma e'_r - \left(e'_m + \left(x_0 - x'\right)i_r\right)/T'_0 \tag{3.8}$$

The link between voltages, currents and state variables is as follows:

$$v_r - e'_r = r_S i_r - x' i_m$$
$$v_m - e'_m = r_S i_m - x' i_r \tag{3.9}$$

where x_0, x' and T_0' can be obtained from the motor parameters:

$$\begin{aligned} x_0 &= x_s + x_m \\ x' &= x_s + \frac{x_{R1} x_m}{x_{R1} + x_m} \\ T_0' &= \frac{x_{R1} + x_m}{\Omega_b r_{R1}} \end{aligned} \tag{3.10}$$

The slip dynamic for squirrel-cage induction motors can be described as follows:

$$\dot{\sigma} = \left(T_m(\sigma) - T_e\right) / \left(2H_m\right) \tag{3.11}$$

where the electrical torque is:

$$T_e = e_r' i_r + e_m' i_m \tag{3.12}$$

Order V Model (double squirrel-cage model)

The equivalent electrical circuit used for the double squirrel-cage (Order V) induction motor model is displayed in Figure 3.3. The machine real and imaginary axis are defined with respect to the network reference angle, and equations (3.6) and (3.7) also apply in Order V model. Two voltages behind the stator resistance r_S describe the cage dynamics as follows [93]:

$$\begin{aligned} \dot{e}_r' &= \Omega_b \sigma e_m' - \left(e_r' + \left(x_0 - x'\right) i_m\right) / T_0' \\ \dot{e}_m' &= -\Omega_b \sigma e_r' - \left(e_m' + \left(x_0 - x'\right) i_r\right) / T_0' \\ \dot{e}_r'' &= -\Omega_b \sigma \left(e_m' - e_m''\right) + \dot{e}_r' - \left(e_r' - e_m'' - \left(x' - x''\right) i_m\right) / T_0'' \\ \dot{e}_m'' &= \Omega_b \sigma \left(e_r' - e_r''\right) + \dot{e}_m' - \left(e_m' - e_r'' + \left(x' - x''\right) i_r\right) / T_0'' \end{aligned} \tag{3.13}$$

The links between voltages and currents are:

$$\begin{aligned} v_r - e_r'' &= r_S i_r - x'' i_m \\ v_m - e_m'' &= r_S i_m + x'' i_r \end{aligned} \tag{3.14}$$

where the parameters can be determined from the circuit resistance and reactances. They are given by (3.10) in the Order III model and:

$$x'' = x_S + \frac{x_{R1}x_{R2}x_m}{x_{R1}x_{R2} + x_{R1}x_m + x_{R2}x_m}$$
$$T_0'' = \frac{x_{R2} + x_{R1}x_m / \left(x_{R1} + x_m\right)}{\Omega_b r_{R2}} \tag{3.15}$$

The differential equation describing the slip dynamics is the same (3.11) as in Order III model, while the equation for electrical torque is as follows:

$$T_e = e_r'' i_r + e_m'' i_m \tag{3.16}$$

3.2.3 A guideline for constructing a numerical energy function and the corresponding BCU method

A numerical energy function for lossy power system stability models can be constructed by two methods. The first method is based on the first integral principle while the other is based on a two-step procedure [3, 6]. The numerical energy function derived by these methods all contain path-dependent terms which need to be evaluated by a numerical approximation scheme. Two approximation schemes are employed in our development: ray-approximation scheme and the trapezoidal approximation schemes. For more detail on these approximation schemes, see [6]. It is suggested to use the trapezoidal scheme to avoid a numerical ill-conditioned problem during the approximation of a path-dependent term.

A guideline for constructing a numerical energy function for power system with dynamic loads and the corresponding BCU method is presented as follows:

Step 1: Derive a new DAE (or ODE) system that includes dynamic load models.

Step 2: Apply the first integral principle or two-step procedure to construct a numerical energy function for the new DAE (or ODE) derived in step 1.

Step 3: Check the validity of the numerical energy function. This energy function value should be non-increasing along a stable trajectory.

Step 4: Derive a numerical expression of the BCU reduced-state artificial system using the energy function constructed in step 2.

Step 5: Implement a new numerical BCU method as suggested in Chapter 1 or [6].

3.3 Construction of Numerical Energy Functions for Power system Models with Induction Motors

The development of new numerical energy functions for power systems with dynamic loads (Order I and Order III induction motors) is completed by following the guideline given in Section 3.2.3. We first present a complete network-preserving power system model that includes an induction motor model, and then show the numerical work on the construction of a new numerical energy function.

3.3.1 Network-preserving model with Order I induction motor

In order to construct a numerical energy function for a power system, as suggested in [6], the derivation of the full network-preserving power system model must be made. In this section, we derive a complete network-preserving model with dynamic loads (Order I or simplified induction motors). The formulation includes two-axis generator models, first-order excitation system, dynamic load models (Order I induction motor), and the slip dynamic of the induction motors. Bus n+1 is considered as a reference frame. Bus 1,…, n are PV bus and bus n+2,…, n+m+1 are PQ buses.

Two-axis generator dynamics for i = 1,…, n

$$
\begin{aligned}
\dot{\delta}_i &= \omega_i \\
M_i\dot{\omega}_i &= -D_i\omega_i + P_{mi} - P_{ei} \\
T'_{doi}\dot{E}'_{qi} &= -\frac{x_{di}}{x'_{di}}E'_{qi} - \frac{x_{di}-x'_{di}}{x'_{di}}V_i\cos(\delta_i-\theta_i) + E_{fi} \\
T'_{qoi}\dot{E}'_{di} &= -\frac{x_{qi}}{x'_{qi}}E'_{di} - \frac{x_{qi}-x'_{qi}}{x'_{qi}}V_i\sin(\delta_i-\theta_i)
\end{aligned}
\tag{3.17}
$$

where $$P_{ei} = \frac{1}{x'_{di}}E'_{qi}V_i\sin\left(\delta_i-\theta_i\right) + \frac{1}{x'_{qi}}E'_{di}V_i\cos\left(\delta_i-\theta_i\right) + \frac{x'_{di}-x'_{qi}}{2x'_{di}x'_{qi}}V_i^2\sin\left[2\left(\delta_i-\theta_i\right)\right]$$

First-order exciter dynamics for i = 1,…, n

$$T_{vi}\dot{E}_{fi} = -E_{fi} + \mu_i k_i V_i\cos\left(\delta_i-\theta_i\right) - l_i \tag{3.18}$$

PV-bus Power flow equations for i = 1,…, n

$$
\begin{aligned}
0 &= \sum_{j\neq i}^{n+1} V_iV_j\left(C_{ij}\cos\theta_{ij} + B_{ij}\sin\theta_{ij}\right) \\
&+ \sum_{l=n+2}^{n+m+1} V_iV_l\left(C_{il}\cos\theta_{il} + B_{il}\sin\theta_{il}\right) \\
&- \frac{1}{x'_{di}}E'_{qi}V_i\sin\left(\delta_i-\theta_i\right) - \frac{1}{x'_{qi}}E'_{di}V_i\cos\left(\delta_i-\theta_i\right) \\
&- \frac{x'_{di}-x'_{qi}}{2x'_{di}x'_{qi}}V_i^2\sin\left[2\left(\delta_i-\theta_i\right)\right]
\end{aligned}
\tag{3.19}
$$

$$
\begin{aligned}
0 &= \sum_{j\neq i}^{n+1} V_iV_j\left(C_{ij}\sin\theta_{ij} - B_{ik}\cos\theta_{ij}\right) \\
&+ \sum_{l=n+2}^{n+m+1} V_iV_l\left(C_{il}\sin\theta_{il} - B_{il}\cos\theta_{il}\right) \\
&+ \frac{V_i^2}{x'_{di}} - \frac{1}{x'_{di}}E'_{qi}V_i\cos\left(\delta_i-\theta_i\right) - \frac{1}{x'_{qi}}E'_{di}V_i\sin\left(\delta_i-\theta_i\right) \\
&- \frac{x'_{di}-x'_{qi}}{2x'_{di}x'_{qi}}V_i^2\left[\cos 2\left(\delta_i-\theta_i\right)-1\right]
\end{aligned}
\tag{3.20}
$$

PQ-bus Power flow equations (ZIP with order I induction motor) for k = n+2,…, n+m+1

$$P_{Lnewi}^{(0)}\left[\alpha_{Pi}+\beta_{Pi}\left(\frac{V_i}{V_i^{(0)}}\right)+\gamma_{Pi}\left(\frac{V_i}{V_i^{(0)}}\right)^2\right]+\left(\frac{r_{R1}V_i^2/\sigma_i}{\left(r_S+r_{R1}/\sigma\right)^2+\left(x_S+x_{R1}\right)^2}\right)$$
$$=\sum_{j=1}^{n+m+1}V_kV_j\left(C_{kj}\cos\theta_{kj}+B_{kj}\sin\theta_{kj}\right) \tag{3.21}$$

$$Q_{Lnewi}^{(0)}\left[\alpha_{Qi}+\beta_{Qi}\left(\frac{V_i}{V_i^{(0)}}\right)+\gamma_{Qi}\left(\frac{V_i}{V_i^{(0)}}\right)^2\right]$$
$$+\left(\frac{V^2}{x_m}+\frac{\left(x_S+x_{R1}\right)V_i^2}{\left(r_S+r_{R1}/\sigma\right)^2+\left(x_S+x_{R1}\right)^2}\right) \tag{3.22}$$
$$=\sum_{j=1}^{n+m+1}V_kV_j\left(C_{kj}\sin\theta_{kj}-B_{kj}\cos\theta_{kj}\right)$$

Slip dynamics (induction motor) for k = n+2,…, n+m+1

$$\dot{\sigma}_k=\frac{1}{2H_{mk}}\left(\alpha_k+\beta_k\sigma_k+\gamma_k{\sigma_k}^2-\frac{r_{R1k}{V_k}^2/\sigma_k}{\left(r_{Sk}+r_{R1k}/\sigma_k\right)^2+\left(x_{Sk}+x_{R1k}\right)^2}\right) \tag{3.23}$$

The set of equations (3.17)-(3.23) construct a complete network-preserving power system model with dynamic loads (Order I induction motor). The additional terms associated with the induction motor are present in the ZIPM load model in (3.21) and (3.22), and the slip dynamics in (3.23).

3.3.2 A numerical energy function for Order I induction motor model

We next show the derivation of a numerical energy function constructed from the new network preserving model derived in the previous section. This represents a numerical energy function for power systems with Order I induction motors. The expression of ZIP load models added by Order I induction motors can be described as follows:

$$P_{Lnewi} = P_{Lnewi}^{(0)}\left[\alpha_{Pi} + \beta_{Pi}\left(\frac{V_i}{V_i^{(0)}}\right) + \gamma_{Pi}\left(\frac{V_i}{V_i^{(0)}}\right)^2\right] + \left(\frac{r_{R1}V_i^2/\sigma_i}{\left(r_S + r_{R1}/\sigma\right)^2 + \left(x_S + x_{R1}\right)^2}\right)$$

$$Q_{Lnewi} = Q_{Lnewi}^{(0)}\left[\alpha_{Qi} + \beta_{Qi}\left(\frac{V_i}{V_i^{(0)}}\right) + \gamma_{Qi}\left(\frac{V_i}{V_i^{(0)}}\right)^2\right] + \left(\frac{V^2}{x_m} + \frac{\left(x_S + x_{R1}\right)V_i^2}{\left(r_S + r_{R1}/\sigma\right)^2 + \left(x_S + x_{R1}\right)^2}\right) \quad (3.24)$$

for i = 1,...,$n+m$

* P_{Li} are zero at PV buses.

The slip dynamics must be considered and its expression is:

$$2H_{mi}\dot{\sigma}_i = \alpha_i + \beta_i\sigma_i + \gamma_i\sigma_i^2 - \frac{r_{R1i}V_i^2/\sigma_i}{\left(r_{Si} + r_{R1i}/\sigma_i\right)^2 + \left(x_{Si} + x_{R1i}\right)^2} \quad (3.25)$$

for i = 1,...,$n+m$

* No slip dynamics at PV buses

The derivation of a numerical energy for the new system is performed by using the first integral principle described in [3, 6]. The final energy function W_{Motor1} developed in this section will be composed of various parts: (1) energy function associated with swing equations W_{Swing}, (2) energy function associated with power flow equations W_{PF}, (3) energy function associated with rotor circuit equations W_{Rotor}, and (4) energy function associated with slip equations W_{slip}. Summing all four parts, we get:

$$W_{Motor1} = W_{Swing} + W_{PF} + W_{Rotor} + W_{Slip} \quad (3.26)$$

Since the new system model with induction motors developed in this thesis is a direct extension from the network preserving-model presented in [6, p.85], most of the terms in W_{Motor1} have been already derived and can be found in [6, pp.100-104]. The expressions for W_{Swing} and

W_{Rotor} are identical to those in [6] while W_{PF} needs to be updated due to the extra power demands from the induction motors as shown in (3.24). The expression of W_{Slip} is new and needs to be derived. In this chapter, we only present the new numerical expressions we developed for the updated W_{PF}, and W_{Slip}. For the full expression of other parts that have been derived, please see [6].

As we can see in (3.24), the new expression of load models are voltage and slip dependent. As a result, it is not possible to derive an analytic expression of the first integral in this case. However we can approximate it by treating it as a path dependent integral described as follows:

$$\sum_{i}^{n+m}\int_{0}^{t} P_{Lnewi}\left(V_i,\sigma_i\right)\dot{\theta}_i \mathrm{d}t = \sum_{i}^{n+m}\int_{\theta_i^s}^{\theta_i} P_{Lnewi}\left(V_i,\sigma_i\right)\mathrm{d}\theta_i \tag{3.27}$$

Multiply the slip dynamics equations by $\frac{d\sigma_i}{dt}$ and sum over the n+m machines, we get the following:

$$\begin{aligned} 2H_{mi}\dot{\sigma}_i\frac{d\sigma_i}{dt} = {} & \alpha_i\frac{d\sigma_i}{dt} + \beta_i\sigma_i\frac{d\sigma_i}{dt} + \gamma_i{\sigma_i}^2\frac{d\sigma_i}{dt} \\ & - \frac{r_{R1i}V_i^2/\sigma_i}{\left(r_{Si}+r_{R1i}/\sigma_i\right)^2+\left(x_{Si}+x_{R1i}\right)^2}\frac{d\sigma_i}{dt} \\ & \text{for i} = 1,...,n+m \end{aligned} \tag{3.28}$$

After summing the above expression over all the equations and integrating, we get the first integral terms for the slip dynamics.

$$\begin{aligned} \sum_{i=1}^{n+m}\int 2H_{mi}\dot{\sigma}_i\frac{d\sigma_i}{dt}dt = \sum_{i=1}^{n+m}\int \Bigg(& \alpha_i\frac{d\sigma_i}{dt} + \beta_i\sigma_i\frac{d\sigma_i}{dt} + \gamma_i{\sigma_i}^2\frac{d\sigma_i}{dt} \\ & - \frac{r_{R1i}V_i^2/\sigma_i}{\left(r_{Si}+r_{R1i}/\sigma_i\right)^2+\left(x_{Si}+x_{R1i}\right)^2}\frac{d\sigma_i}{dt} \Bigg) dt \\ & \text{for i} = 1,...,n+m \end{aligned} \tag{3.29}$$

$$\sum_{i=1}^{n+m}\int 2H_{mi}\dot{\sigma}_i^{\,2}dt-\sum_{i=1}^{n+m}\left(\alpha_i(\sigma_i-\sigma^s{}_i)+\beta_i\left(\frac{\sigma_i^{\,2}-\sigma_i^{s2}}{2}\right)+\gamma_i\left(\frac{\sigma_i^{\,3}-\sigma_i^{s3}}{3}\right)\right)$$
$$-\sum_{i=1}^{n+m}\int\left(\frac{r_{R1i}V_i^2/\sigma_i}{\left(r_{Si}+r_{R1i}/\sigma_i\right)^2+\left(x_{Si}+x_{R1i}\right)^2}\right)d\sigma_i=0 \qquad (3.30)$$
$$\text{for i = 1,...,}n+m$$

We have now derived five new energy function terms that are associated with the updated W_{PF} and W_{Slip} as follows:

$$U_{new1}^{Motor1}=\text{ due to active load }=\sum_{i}^{n+m}\int_{\theta_i^s}^{\theta_i}P_{Lnewi}\left(V_i,\sigma_i\right)\mathrm{d}\theta_i \qquad (3.31)$$

$$U_{new2}^{Motor1}=\text{ due to reactive load }=\sum_{i}^{n+m}\int_{\theta_i^s}^{\theta_i}Q_{Lnewi}\left(V_i,\sigma_i\right)\mathrm{d}\theta_i \qquad (3.32)$$

$$U_{new3}^{Motor1}=\text{ due to time variation of }\frac{d\sigma}{dt}=\sum_{i=1}^{n+m}\int 2H_{mi}\dot{\sigma}_i^{\,2}dt \qquad (3.33)$$

$$U_{new4}^{Motor1}=\text{ due to slip (path independent)}$$
$$=-\sum_{i=1}^{n+m}\left(\alpha_i(\sigma_i-\sigma^s{}_i)+\beta_i\left(\frac{\sigma_i^{\,2}-\sigma_i^{s2}}{2}\right)+\gamma_i\left(\frac{\sigma_i^{\,3}-\sigma_i^{s3}}{3}\right)\right) \qquad (3.34)$$

$$U_{new5}^{Motor1}=\text{ due to slip (path dependent)}$$
$$=-\sum_{i=1}^{n+m}\int\left(\frac{r_{R1i}V_i^2/\sigma_i}{\left(r_{Si}+r_{R1i}/\sigma_i\right)^2+\left(x_{Si}+x_{R1i}\right)^2}\right)d\sigma_i \qquad (3.35)$$

As shown in [6, p.103], the energy function shown in (3.26) can now be rearrange as follows:

$$W_{Motor1}=W_k+\sum_{i=1}^{23}U_i+\sum_{i=1}^{5}U_{newi}^{Motor1} \qquad (3.36)$$

where W_k is the kinetic energy, $U_1 - U_{23}$ are energy function terms found in [6], and $U_{new1} - U_{new5}$ are the new terms we derived in (3.31)-(3.35). This completes the derivation of a numerical energy function for power system models with Order I induction motors.

3.3.3 A numerical energy function for Order III induction motor model

Following the same procedure presented in Section 3.3.2, we first derive a new ZIPM load model when Order III induction motors are considered.

$$\begin{aligned} P_{Lnewi}^{Motor3} &= P_{Lnewi}^{Motor3(0)} \left[\alpha_{Pi} + \beta_{Pi} \left(\frac{V_i}{V_i^{(0)}} \right) + \gamma_{Pi} \left(\frac{V_i}{V_i^{(0)}} \right)^2 \right] \\ &\quad + \left(\frac{V_i^2 \left(r_S - x' \sin 2\theta_i \right) + V_i \sin\theta_i \left(r_S e'_{ri} + x' e'_{mi} \right) - V_i \cos\theta_i \left(x' e'_{ri} + r_S e'_{mi} \right)}{r_S{}^2 + x'^2} \right) \\ Q_{Lnewi}^{Motor3} &= Q_{Lnewi}^{Motor3(0)} \left[\alpha_{Qi} + \beta_{Qi} \left(\frac{V_i}{V_i^{(0)}} \right) + \gamma_{Qi} \left(\frac{V_i}{V_i^{(0)}} \right)^2 \right] \\ &\quad + \left(\frac{V_i^2 x' \cos 2\theta_i - V_i \cos\theta_i \left(r_S e'_{ri} + x' e'_{mi} \right) - V_i \sin\theta_i \left(x' e'_{ri} + r_S e'_{mi} \right)}{r_S{}^2 + x'^2} \right) \end{aligned} \tag{3.37}$$

$$\text{for i} = 1,\ldots,n+m$$

* P_{Li} are zero at PV buses.

The slip dynamics must also be considered and its expression is:

$$\begin{aligned} 2H_{mi}\dot{\sigma}_i &= \alpha_i + \beta_i \sigma_i + \gamma_i \sigma_i{}^2 \\ &\quad - \left(\frac{-2x' e'_{mi} e'_{ri} - r_S \left(e'_{ri}{}^2 + e'_{mi}{}^2 \right) - V_i \sin\theta_i \left(r_S e'_{ri} + x' e'_{mi} \right) + V_i \cos\theta_i \left(x' e'_{ri} + r_S e'_{mi} \right)}{r_S{}^2 + x'^2} \right) \end{aligned} \tag{3.38}$$

$$\text{for i} = 1,\ldots,n+m$$

* No slip dynamics at PV buses

The dynamics for the voltages behind the stator resistance r_S can be described as follows:

$$\begin{aligned}\dot{e}'_{ri} &= \Omega_b \sigma_i e'_{mi} - \left(e'_{ri} + \left(x_0 - x' \right) \left(\frac{x' \left(-V_i \sin\theta_i - e'_r \right) + r_S \left(V_i \cos\theta_i - e'_{mi} \right)}{r_S^2 - x'^2} \right) \right) / T'_0 \\ \dot{e}'_{mi} &= -\Omega_b \sigma_i e'_{ri} - \left(e'_{mi} + \left(x_0 - x' \right) \left(\frac{r_S \left(-V_i \sin\theta_i - e'_r \right) + x' \left(V_i \cos\theta_i - e'_{mi} \right)}{r_S^2 - x'^2} \right) \right) / T'_0 \end{aligned} \tag{3.39}$$

Using the first integral principle and same guideline presented in the previous section, we can derive the new numerical energy function terms associated with the new equations shown in (3.37)-(3.39). The new energy function terms are as follows:

$$U_{new1}^{Motor3} = \text{ due to active load } = \sum_i^{n+m} \int_{\theta_i^s}^{\theta_i} P_{Lnewi}^{Motor3} \left(V_i, \sigma_i \right) \mathrm{d}\theta_i \tag{3.40}$$

$$U_{new2}^{Motor3} = \text{ due to reactive load } = \sum_i^{n+m} \int_{\theta_i^s}^{\theta_i} Q_{Lnewi}^{Motor3} \left(V_i, \sigma_i \right) \mathrm{d}\theta_i \tag{3.41}$$

$$U_{new3}^{Motor3} = \text{ due to time variation of } \frac{d\sigma}{dt} = \sum_{i=1}^{n+m} \int 2H_{mi} \dot{\sigma}_i^{\,2} dt \tag{3.42}$$

$$\begin{aligned} U_{new4}^{Motor3} &= \text{ due to slip (path independent)} \\ &= -\sum_{i=1}^{n+m} \left(\alpha_i (\sigma_i - \sigma^s{}_i) + \beta_i \left(\frac{\sigma_i^{\,2} - \sigma_i^{s2}}{2} \right) + \gamma_i \left(\frac{\sigma_i^{\,3} - \sigma_i^{s3}}{3} \right) \right) \end{aligned} \tag{3.43}$$

$$\begin{aligned} U_{new5}^{Motor3} &= \text{ due to slip (path dependent)} \\ &= -\sum_{i=1}^{n+m} \int \left(\frac{-2x' e'_{mi} e'_{ri} - r_S \left(e'^{\,2}_{ri} + e'^{\,2}_{mi} \right) - V_i \sin\theta_i \left(r_S e'_{ri} + x' e'_{mi} \right) + V_i \cos\theta_i \left(x' e'_{ri} + r_S e'_{mi} \right)}{r_S^{\,2} + x'^2} \right) d\sigma_i \end{aligned} \tag{3.44}$$

$$\begin{aligned} U_{new6}^{Motor3} &= \text{ due to voltage (real part) behind } r_{Si} \\ &= -\sum_{i=1}^{n+m} \int \left(\Omega_b \sigma_i e'_{mi} - \left(e'_{ri} + \left(x_0 - x' \right) \left(\frac{x' \left(-V_i \sin\theta_i - e'_r \right) + r_S \left(V_i \cos\theta_i - e'_{mi} \right)}{r_S^2 - x'^2} \right) \right) / T'_0 \right) de'_{ri} \end{aligned} \tag{3.45}$$

$$\begin{aligned} U_{new7}^{Motor3} &= \text{ due to voltage (imaginary part) behind } r_{Si} \\ &= -\sum_{i=1}^{n+m} \int \left(-\Omega_b \sigma_i e'_{ri} - \left(e'_{mi} + \left(x_0 - x' \right) \left(\frac{r_S \left(-V_i \sin\theta_i - e'_r \right) + x' \left(V_i \cos\theta_i - e'_{mi} \right)}{r_S^2 - x'^2} \right) \right) / T'_0 \right) de'_{mi} \end{aligned} \tag{3.46}$$

Combining the new energy function terms derived in (3.40)-(3.46) with other available terms in [6], the numerical energy function for power systems with Order III induction motors can be described as follows:

$$W_{Motor3} = W_k + \sum_{i=1}^{23} U_i + \sum_{i=1}^{7} U_{newi}^{Motor3} \tag{3.47}$$

3.4 Compact Representation of the System Models and the Derivation of the BCU Reduced-State Artificial Systems for Power System with Dynamic Loads

The potential energy function terms for induction motor models in (3.36) and (3.47) can be combined as follows:

$$\hat{U}_{Motor1} = \sum_{i=1}^{23} U_i + \sum_{i=1}^{5} U_{newi}^{Motor1} \tag{3.48}$$

$$\hat{U}_{Motor3} = \sum_{i=1}^{23} U_i + \sum_{i=1}^{7} U_{newi}^{Motor3} \tag{3.49}$$

The compact representation of the original network preserving model with Order I induction motors can then be expressed as follows:

$$\begin{aligned}
0 &= -\frac{\partial}{\partial \theta_i}\hat{U}_{Motor1}\left(\delta,\theta,V,E'_q,E'_d,\sigma\right) \\
0 &= -\frac{1}{V_i}\frac{\partial}{\partial V_i}\hat{U}_{Motor1}\left(\delta,\theta,V,E'_q,E'_d,\sigma\right) \\
\dot{\delta}_i &= \omega_i \\
M_i\dot{\omega}_i &= -\frac{\partial}{\partial \delta_i}\hat{U}_{Motor1}\left(\delta,\theta,V,E'_q,E'_d,\sigma\right) \\
0 &= -\frac{\partial}{\partial E'_{qi}}\hat{U}_{Motor1}\left(\delta,\theta,V,E'_q,E'_d,\sigma\right) \\
0 &= -\frac{\partial}{\partial E'_{di}}\hat{U}_{Motor1}\left(\delta,\theta,V,E'_q,E'_d,\sigma\right) \\
0 &= -\frac{\partial}{\partial \sigma_i}\hat{U}_{Motor1}\left(\delta,\theta,V,E'_q,E'_d,\sigma\right)
\end{aligned} \tag{3.50}$$

The corresponding BCU reduced-state artificial system for Order I induction motor model can be derived and described as follows:

$$
\begin{aligned}
0 &= -\frac{\partial}{\partial \theta_i}\hat{U}_{Motor1}\left(\delta,\theta,V,E'_q,E'_d,\sigma\right)\\
0 &= -\frac{1}{V_i}\frac{\partial}{\partial V_i}\hat{U}_{Motor1}\left(\delta,\theta,V,E'_q,E'_d,\sigma\right)\\
\dot{\delta}_i &= -\frac{\partial}{\partial \delta_i}\hat{U}_{Motor1}\left(\delta,\theta,V,E'_q,E'_d,\sigma\right)\\
0 &= -\frac{\partial}{\partial E'_{qi}}\hat{U}_{Motor1}\left(\delta,\theta,V,E'_q,E'_d,\sigma\right)\\
0 &= -\frac{\partial}{\partial E'_{di}}\hat{U}_{Motor1}\left(\delta,\theta,V,E'_q,E'_d,\sigma\right)\\
0 &= -\frac{\partial}{\partial \sigma_i}\hat{U}_{Motor1}\left(\delta,\theta,V,E'_q,E'_d,\sigma\right)
\end{aligned}
\tag{3.51}
$$

The compact representation of the original network preserving model with Order III induction motors can then be expressed as follows:

$$
\begin{aligned}
0 &= -\frac{\partial}{\partial \theta_i}\hat{U}_{Motor3}\left(\delta,\theta,V,E'_q,E'_d,\sigma,e'_m\right)\\
0 &= -\frac{1}{V_i}\frac{\partial}{\partial V_i}\hat{U}_{Motor3}\left(\delta,\theta,V,E'_q,E'_d,\sigma,e'_r,e'_m\right)\\
\dot{\delta}_i &= \omega_i\\
M_i\dot{\omega}_i &= -\frac{\partial}{\partial \delta_i}\hat{U}_{Motor3}\left(\delta,\theta,V,E'_q,E'_d,\sigma,e'_r,e'_m\right)\\
0 &= -\frac{\partial}{\partial E'_{qi}}\hat{U}_{Motor3}\left(\delta,\theta,V,E'_q,E'_d,\sigma,e'_r,e'_m\right)\\
0 &= -\frac{\partial}{\partial E'_{di}}\hat{U}_{Motor3}\left(\delta,\theta,V,E'_q,E'_d,\sigma,e'_r,e'_m\right)\\
0 &= -\frac{\partial}{\partial \sigma_i}\hat{U}_{Motor3}\left(\delta,\theta,V,E'_q,E'_d,\sigma,e'_r,e'_m\right)\\
0 &= -\frac{\partial}{\partial e'_{ri}}\hat{U}_{Motor3}\left(\delta,\theta,V,E'_q,E'_d,\sigma,e'_r,e'_m\right)\\
0 &= -\frac{\partial}{\partial e'_{mi}}\hat{U}_{Motor3}\left(\delta,\theta,V,E'_q,E'_d,\sigma,e'_r,e'_m\right)
\end{aligned}
\tag{3.52}
$$

The corresponding BCU reduced-state artificial system for Order III are described as follows:

$$
\begin{aligned}
0 &= -\frac{\partial}{\partial \theta_i}\hat{U}_{Motor3}\left(\delta,\theta,V,E'_q,E'_d,\sigma,e'_m\right)\\
0 &= -\frac{1}{V_i}\frac{\partial}{\partial V_i}\hat{U}_{Motor3}\left(\delta,\theta,V,E'_q,E'_d,\sigma,e'_r,e'_m\right)\\
\dot{\delta}_i &= -\frac{\partial}{\partial \delta_i}\hat{U}_{Motor3}\left(\delta,\theta,V,E'_q,E'_d,\sigma,e'_r,e'_m\right)\\
0 &= -\frac{\partial}{\partial E'_{qi}}\hat{U}_{Motor3}\left(\delta,\theta,V,E'_q,E'_d,\sigma,e'_r,e'_m\right)\\
0 &= -\frac{\partial}{\partial E'_{di}}\hat{U}_{Motor3}\left(\delta,\theta,V,E'_q,E'_d,\sigma,e'_r,e'_m\right)\\
0 &= -\frac{\partial}{\partial \sigma_i}\hat{U}_{Motor3}\left(\delta,\theta,V,E'_q,E'_d,\sigma,e'_r,e'_m\right)\\
0 &= -\frac{\partial}{\partial e'_{ri}}\hat{U}_{Motor3}\left(\delta,\theta,V,E'_q,E'_d,\sigma,e'_r,e'_m\right)\\
0 &= -\frac{\partial}{\partial e'_{mi}}\hat{U}_{Motor3}\left(\delta,\theta,V,E'_q,E'_d,\sigma,e'_r,e'_m\right)
\end{aligned}
\tag{3.53}
$$

3.5 Numerical Examples

We next present numerical results from running the extended BCU method with induction motor model on two adapted WSCC9 test systems. A detailed description on how to implement a numerical BCU method can be found in Chapter 1 or [6].

3.5.1 Example 1: Adapted WSCC9 with one induction motor

We present simulation results from running the new BCU method on an adapted WSCC9 system [2] as shown in Figure 3.4. In this example, the constant power load model at bus 7 is entirely replaced by an induction motor. The induction motor is formulated by the Order I or simplified model. The motor parameters are as follows: rS = 0.01, xS = 0.15, rR1 = 0.05, xR1 =

0.15, rR2 = 0.001, xR2 = 0.04, xm = 5, Hm = 3, a = 1, b = 0, and c = 0. The classical generator model is used in this first test system.

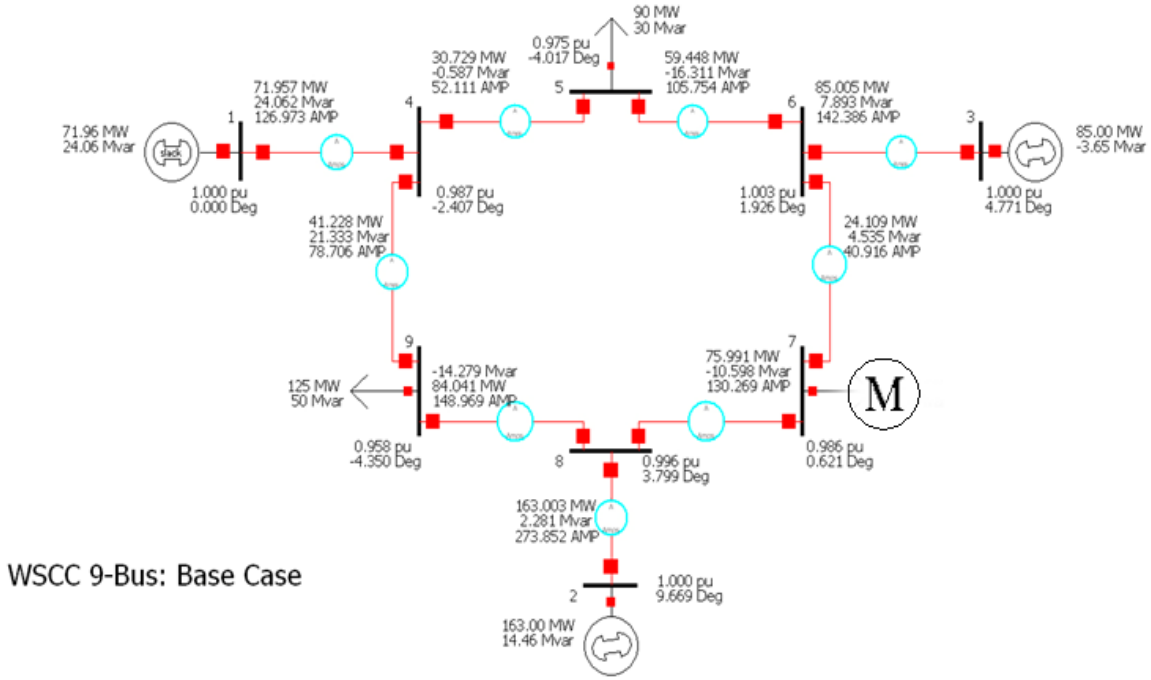

Figure 3.4 Adapted WSCC9 with Order I induction motor at bus 7

Table 3.1 contains the post-fault SEPs of five different contingencies associated with the first adapted WSCC9 test system with Order I induction motor at bus 7. Table 3.2 shows the corresponding controlling unstable equilibrium points or CUEPs of the same five contingencies in Table 3.1. The CUEPs are computed by the new BCU method developed in this chapter. The results shown in Table 3.3 display successful direct assessments by the new BCU method on 8 different contingencies. It can be seen that the critical clearing time or CCTs computed by the BCU method are all conservative (smaller) when compared to the actual CCTs which are computed by time-domain simulations. The average relative error for the estimated critical clearing times computed by the BCU method is 7.03%. Using the visualization technique proposed in [46], we plot the stability regions of the post-fault system associated with

contingency#1 and contingency#3. The stability regions are plotted in the state space as depicted in Figure 3.5 and Figure 3.6. This result shows that the approximations of relevant stability boundary via energy function surface passing through CUEPs are always conservative in the direction of fault-on trajectories.

Table 3.1: Post-fault SEPs of the first adapted WSCC9 with Order I induction motor

Post-fault SEP	C#1	C#2	C#3	C#4	C#5
δ1	-0.1575	-0.1575	-0.1219	-0.1219	-0.1325
δ2	0.4487	0.4487	0.4292	0.4292	0.3397
δ3	0.2829	0.2830	0.0451	0.0451	0.3187
ω1	0	0	0	0	0
ω2	0	0	0	0	0
ω3	0	0	0	0	0
σ1	0.0548	0.0549	0.0830	0.0830	0.0498
θ1	-0.1132	-0.1132	-0.0786	-0.0786	-0.0874
θ2	0.3138	0.3138	0.2971	0.2971	0.2087
θ3	0.1704	0.1704	-0.0756	-0.0756	0.2090
θ4	-0.0717	-0.0717	-0.0373	-0.0373	-0.0449
θ5	-0.0726	-0.0726	0.0530	0.0530	0.0172
θ6	-0.0038	-0.0038	-0.0674	-0.0674	0.1685
θ7	0.2419	0.2419	0.2295	0.2295	0.1417
θ8	0.1586	0.1586	-0.2279	-0.2279	0.1203
θ9	0.1353	0.1353	-0.1166	-0.1166	0.1757
V1	1.0618	1.0618	1.0526	1.0526	1.0586
V2	1.0301	1.0301	1.0578	1.0578	1.0579
V3	1.0395	1.0395	0.9744	0.9744	1.0634
V4	1.0685	1.0685	1.0506	1.0506	1.0623
V5	1.0766	1.0766	1.0576	1.0576	1.0713
V6	1.0712	1.0712	1.0363	1.0363	1.1148
V7	1.0272	1.0272	1.0690	1.0690	1.0690
V8	1.0149	1.0149	0.8787	0.8787	1.0556
V9	1.0495	1.0495	0.9638	0.9638	1.0809

C#1: Fault bus is 5, Tripped line is 7-5 C#2: Fault bus is 7, Tripped line is 7-5
C#3: Fault bus is 7, Tripped line is 8-7 C#4: Fault bus is 8, Tripped line is 8-7
C#5: Fault bus is 4, Tripped line is 4-6

Table 3.2: CUEPs of the adapted WSCC9 with induction motor

CUEP	C#1	C#2	C#3	C#4	C#5
δ1	-0.7158	-0.7158	-0.4925	-0.7054	-0.7537
δ2	1.9317	1.9317	1.9862	1.7772	1.8138
δ3	1.5146	1.5146	-0.3551	1.7609	1.6651
ω1	0	0	0	0	0
ω2	0	0	0	0	0
ω3	0	0	0	0	0
σ1	0.7832	0.7832	1.2245	0.6889	0.5301
θ1	-0.6987	-0.6987	-0.4833	-0.6748	-0.7537
θ2	1.7469	1.7469	1.7331	1.5688	1.8138
θ3	1.3194	1.3194	-0.5050	1.6066	1.6651
θ4	-0.6720	-0.6720	-0.4701	-0.6247	-0.7039
θ5	-0.7700	-0.7700	-0.2151	-0.2018	-0.3417
θ6	-0.2487	-0.2487	-0.5560	-0.6991	1.4563
θ7	1.6142	1.6142	1.4300	1.3719	1.5858
θ8	1.4342	1.4342	-0.6544	1.4134	1.5499
θ9	1.2065	1.2065	-0.5630	1.5398	1.5928
V1	0.8420	0.8420	0.87389	0.8277	0.8172
V2	0.8496	0.8496	0.6369	0.7258	0.6906
V3	0.6685	0.6685	0.8845	0.8156	0.7909
V4	0.6391	0.6391	0.7009	0.6120	0.5914
V5	0.6069	0.6069	0.4126	0.3430	0.2807
V6	0.3892	0.3892	0.7415	0.5899	0.6807
V7	0.7610	0.7610	0.4597	0.5797	0.5300
V8	0.6587	0.6587	0.8146	0.6430	0.6033
V9	0.5657	0.5657	0.8468	0.7561	0.7239

*See Table 3.1 for the descriptions of all contingencies

Table 3.3: CCT comparisons (BCU vs. Time-domain), WSCC with induction motor

Contingency	Actual CCT (Time-domain)	Estimated CCT (BCU)	Relative Error%
C#1	0.22341	0.20365	-8.84472
C#2	0.12025	0.11358	-5.54678
C#3	0.28501	0.25365	-11.0031
C#4	0.07658	0.07539	-1.55393
C#5	0.11475	0.11356	-1.03704
C#6	0.26387	0.2536	-3.89207
C#7	0.20228	0.20113	-0.56852
C#8	0.13609	0.10366	-23.8298

C#1: Fault bus is 5, Tripped line is 7-5 C#2: Fault bus is 7, Tripped line is 7-5
C#3: Fault bus is 7, Tripped line is 8-7 C#4: Fault bus is 8, Tripped line is 8-7
C#5: Fault bus is 4, Tripped line is 4-6 C#6: Fault bus is 6, Tripped line is 4-6
C#7: Fault bus is 8, Tripped line is 8-9 C#8: Fault bus is 9, Tripped line is 8-9

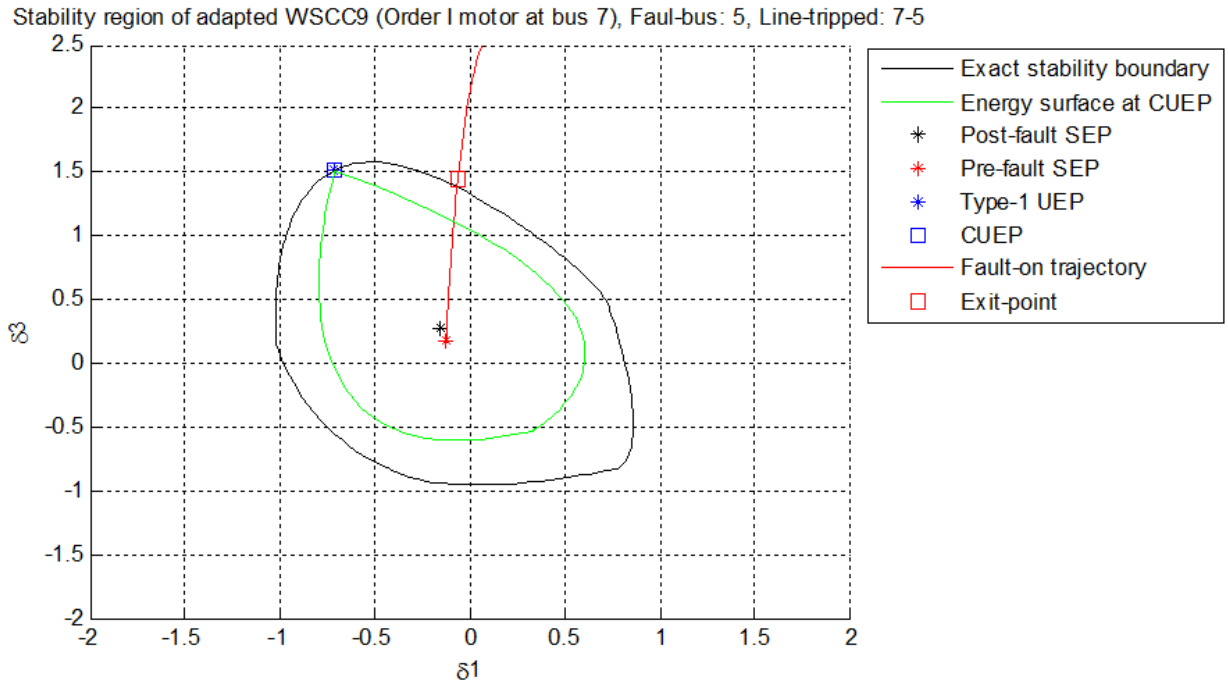

Figure 3.5 The stability region of an adapted WSCC9 with Order I induction motor at bus 7. Contingency # 1 with bus 5 shorted during fault and line 7-5 is tripped. The conservative estimation of relevant stability boundary by the BCU method is also illustrated.

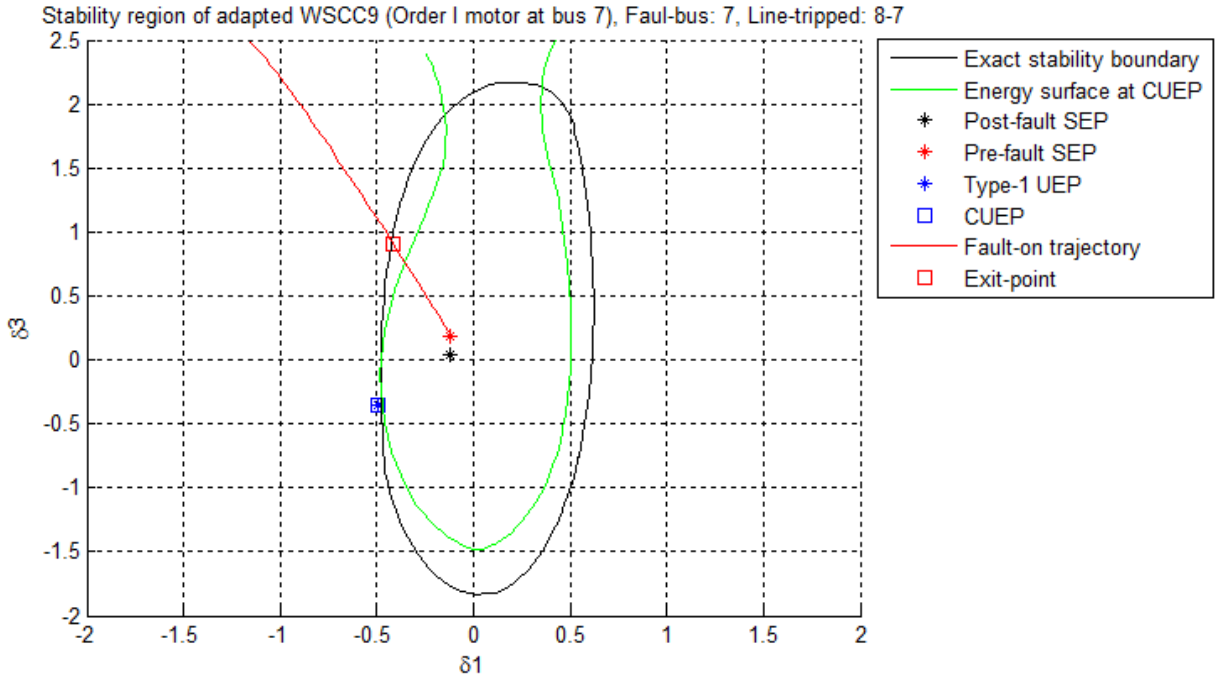

Figure 3.6 The stability region of an adapted WSCC9 with Order I induction motor at bus 7. Contingency # 3 with bus 7 shorted during fault and line 8-7 is tripped. The conservative estimation of relevant stability boundary by the BCU method is also illustrated.

3.5.2 Example 2: Adapted WSCC9 with ZIPM loads

The simulation results from running the new BCU method on the second adapted WSCC9 system (Figure 3.7) are presented. The constant power loads at bus 5, 7 and 9 are entirely replaced by ZIPM loads with a 60:10:10:20 ratio. The induction motor is formulated by an Order I model. The motor parameters are as follows: rS = 0.01, xS = 0.15, rR1 = 0.05, xR1 = 0.15, rR2 = 0.001, xR2 = 0.04, xm = 5, Hm = 3, a = 1, b = 0, and c = 0. The classical generator model is used in this second test system.

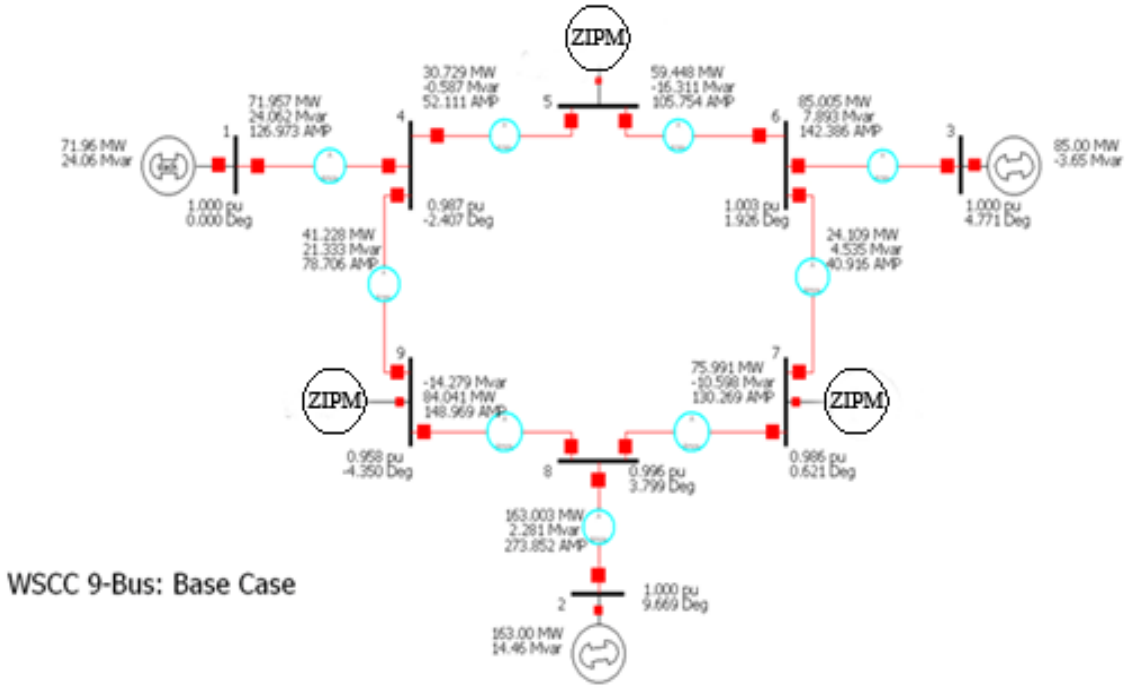

Figure 3.7 Adapted WSCC9 with ZIPM loads on bus 5, 7 and 9

The post-fault SEPs of 5 different contingencies for the second test system are shown in Table 3.4. Based on the same 5 contingencies, the CUEPs are computed by the proposed extended BCU method and presented in Table 3.5. The actual CCTs and estimations by the BCU methods on 8 different contingencies are shown in Table 3.6. Unlike the results we obtained in the first test system, it can be seen that Table 3.5 and Table 3.6 contain cases in which the new

BCU method fails to compute a CUEP. In these cases, the fault-on trajectory runs into an impasse surface (as illustrated in Figure 3.8) before it can detect an exitpoint. In other words. the impasse surface is encountered before the energy function along the fault-on trajectory reaches a local maximum. As a result, the exit-point cannot be identified and therefore the CUEP cannot be computed. In the successful cases, the results in Table 3.6 show all conservative estimations of CCT with an average error of 10.7%. A visualization of the post-fault stability region and a stability boundary approximation by the BCU method is depicted in Figure 3.9.

Table 3.4: Post-fault SEPs of the adapted WSCC9 with ZIPM loads

Post-fault SEP	**C#1**	**C#2**	**C#3**	**C#4**	**C#5**
δ1	-0.18585	-0.18585	-0.13655	-0.13655	-0.10573
δ2	0.422081	0.422081	0.417844	0.417844	0.359956
δ3	0.323474	0.323474	0.072714	0.072714	0.34905
ω1	0	0	0	0	0
ω2	0	0	0	0	0
ω3	0	0	0	0	0
σ1	0.042149	0.042149	0.073866	0.073866	0.05522
σ2	0.123781	0.123781	0.163108	0.163108	0.23753
σ3	0.069679	0.069679	0.176742	0.176742	0.165395
θ1	-0.08528	-0.08528	-0.04057	-0.04057	-0.03841
θ2	0.34391	0.34391	0.332383	0.332383	0.225288
θ3	0.210531	0.210531	-0.05684	-0.05684	0.254202
θ4	-0.03283	-0.03283	0.011443	0.011443	-0.00807
θ5	-0.11979	-0.11979	0.012396	0.012396	0.045221
θ6	-0.00468	-0.00468	-0.07607	-0.07607	0.203121
θ7	0.200607	0.200607	0.19746	0.19746	0.105108
θ8	0.145776	0.145776	-0.23771	-0.23771	0.144474
θ9	0.175161	0.175161	-0.13085	-0.13085	0.209284
V1	1.03107	1.03107	1.018657	1.018657	1.080118
V2	1.046995	1.046995	1.025607	1.025607	1.020101
V3	1.089288	1.089288	1.024295	1.024295	1.080054
V4	1.061768	1.061768	1.099093	1.099093	1.096383
V5	1.050609	1.050609	1.066723	1.066723	1.064873
V6	1.055157	1.055157	1.050169	1.050169	1.069479
V7	1.032329	1.032329	1.107602	1.107602	1.029312
V8	0.965264	0.965264	0.866579	0.866579	1.044323
V9	1.039512	1.039512	0.98747	0.98747	1.107424

*See Table 3.1 for the descriptions of all contingencies

Table 3.5: CUEPs of the adapted WSCC9 with ZIPM loads

CUEP	C#1	C#2	C#3	C#4	C#5
δ1	-0.72486	-0.66668	-0.47908	-	-0.75978
δ2	1.938955	1.777174	2.015379	-	1.78278
δ3	1.502299	1.752075	-0.37516	-	1.69322
ω1	0	0	0	-	0
ω2	0	0	0	-	0
ω3	0	0	0	-	0
σ1	0.819916	0.667689	1.26835	-	0.527345
σ2	0.491571	0.217766	0.840688	-	0.101961
σ3	0.10731	0.494303	0.171013	-	0.313082
θ1	-0.73031	-0.68391	-0.47837	-	-0.77214
θ2	1.747602	1.545104	1.758341	-	1.858581
θ3	1.307567	1.587938	-0.5249	-	1.619442
θ4	-0.69243	-0.62249	-0.48462	-	-0.70016
θ5	-0.79441	-0.18617	-0.18263	-	-0.30297
θ6	-0.22333	-0.72046	-0.52869	-	1.443512
θ7	1.582596	1.365874	1.403351	-	1.633899
θ8	1.481931	1.462976	-0.70061	-	1.585778
θ9	1.163728	1.504782	-0.57358	-	1.575581
V1	0.801744	0.873833	0.867929	-	0.855932
V2	0.801547	0.677716	0.587095	-	0.705661
V3	0.680657	0.810339	0.873389	-	0.764242
V4	0.674296	0.591222	0.694389	-	0.590007
V5	0.598863	0.298449	0.427472	-	0.266339
V6	0.406466	0.585268	0.731173	-	0.716128
V7	0.797349	0.530968	0.45521	-	0.532452
V8	0.650043	0.679662	0.775649	-	0.623386
V9	0.528558	0.781661	0.812495	-	0.710119

*See Table 3.1 for the descriptions of all contingencies

Table 3.6: CCT comparisons (BCU vs. Time-domain), WSCC with ZIPM loads

Contingency	Actual CCT (Time-domain)	Estimated CCT (BCU)	Relative Error%
C#1	0.268709	0.254872	-5.14944
C#2	0.163765	0.160293	-2.12011
C#3	0.056748	0.043501	-23.3436
C#4	-	-	-
C#5	0.085174	0.072364	-15.0398
C#6	-	-	-
C#7	0.196563	0.187354	-4.68501
C#8	0.128206	0.11039	-13.8964

*See Table 3.3 for the descriptions of all contingencies

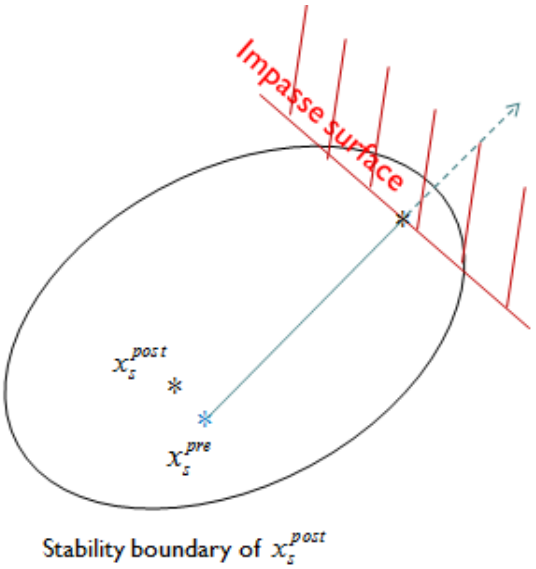

Figure 3.8 An illustration of an impasse surface which can be encountered during the simulation procedure of the BCU method.

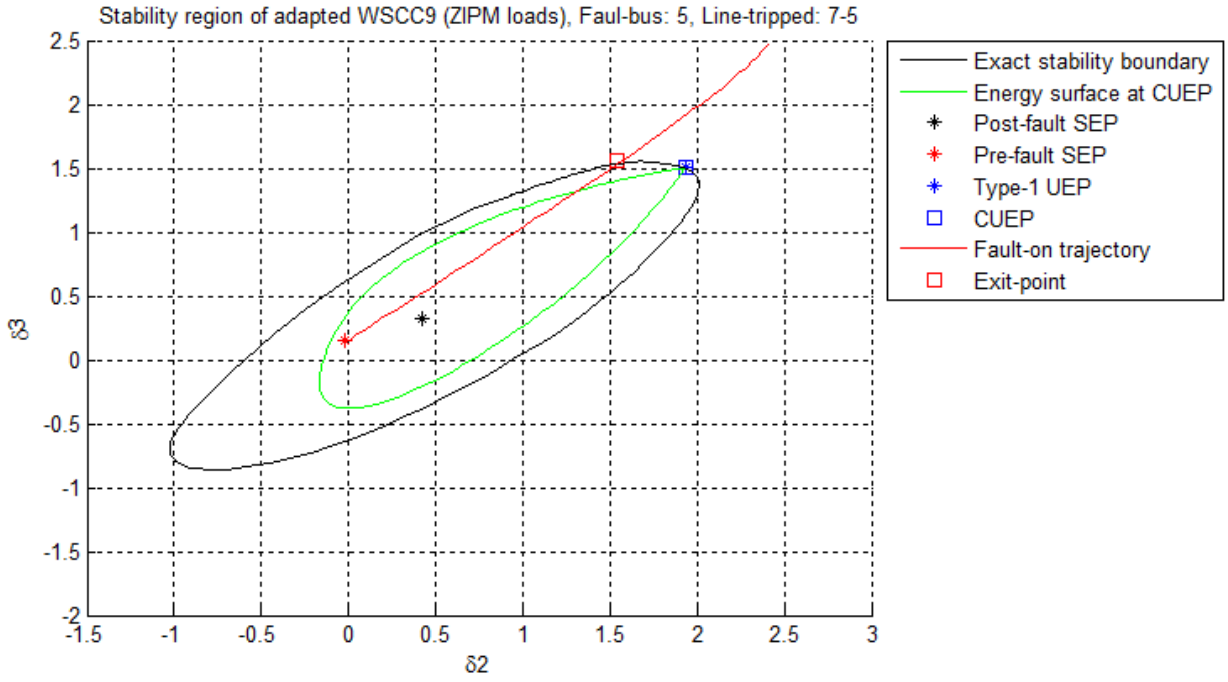

Figure 3.9 The stability region of an adapted WSCC9 with ZIPM loads at all PQ buses. Contingency # 1 with bus 5 shorted during fault and line 7-5 is tripped. The conservative estimation of relevant stability boundary by the BCU method is also illustrated.

3.6 Conclusions

In this chapter, an extension of the BCU method was developed for power systems with induction motors. Based on the first integral principle, we constructed numerical energy functions for power system models with Order I and Order III induction motors, and then employed it to derive the corresponding BCU methods with dynamic load capability. The numerical results on two adapted WSCC9 systems show successful computations of the CUEPs, which consequently lead to the successful conservative direct assessments of transient stability. It must be noted that in some cases where a ZIPM load model is considered, our method was forced to stop prematurely due to the encounter of impasse surface. This numerical issue must be addressed in future work.

CHAPTER 4

A CUEP-Based Enhancement Control Scheme for Large-Scale Power Systems

4.1 Introduction

In the past few decades, the demand for power system dynamic security has significantly increased as the economics and deregulations have forced more power systems to be operated near their stability limits. The past research work in the area of power system dynamic security has focused on transient stability assessment and control. In the aspect of transient stability assessment, time domain simulations, direct methods based on transient energy function [5, 6, 12, 13, 47, 49, 50, 94] and other techniques [51-56] can be employed to obtain stability assessment results.

There are two levels of control where a power system stability can be enhanced. The first level is device-based type of control which involves insertions of various devices capable of improving system stability. These devices include HVDC [146, 147], static exciter [98], SVCs [149] and FACTS devices [95, 100-104, 106-109, 111]. The extra reactive power provided by SVC's and FACTS devices help damp machine rotor angle swing and results in improved system stability. The second level is operation-based control which can be categorized into two subtypes: corrective control and preventive control. The corrective control actions are conducted in the power system control center and include such functions as power flow monitoring and adjustments. The general concept is based on a control as an after-the-fault action. The main issue with corrective control for transient stability is that transient instability can occur and lead

to a cascade or a black-out within a few seconds, which is far too short for the system operators to perform any corrective measures.

A preventive control is a control action designed to bring a vulnerable or insecure system into a secure operating state prior to the occurrence of an actual fault. Only adjustments to system configurations or control variables (such as real and reactive generation outputs, transformer tap changers, etc.) are required. Many schemes in the literature have been based on optimal power flow (OPF) such as the works reported in [32-42, 112] where preventive security dispatch OPF was used for system stability enhancement. However, these methods suffer some shortcomings due to: (1) the difficulty with addition of transient stability as a constraint in control optimization problems, and (2) the computational cost of performing mathematical optimization at regular intervals. A less computationally expensive approach via optimal generation rescheduling has been proposed for security enhancement in [113-119, 125, 129] where transient stability is considered as a constraint for pseudo optimality.

In this chapter, we propose an enhancement control scheme that is based on the generation rescheduling of critical machines. Based on the stability-region related framework, we developed a method for identifying and ranking critical machines in power systems. A literature survey on past attempts on operation-based enhancement controls are given in Section 4.1 and Section 4.2.2. The preliminaries, including the descriptions of the mathematical models and the concept of critical machines, are given in section 4.2. In Section 4.3, we provide the definition and characterization of critical machines using knowledge of stability regions and dynamics in power system. A systematic CUEP-based approach for identifying and ranking critical machines is proposed in Section 4.4. Numerical experimental results are then given in section 4.5 to test the effectiveness of the proposed method. A complete CUEP-based

enhancement control scheme for large-scale power system is proposed in section 4.6 along with numerical studies. The conclusion and discussion are given in section 4.7.

4.2 Preliminaries

4.2.1 Network-reduction model and transient stability

Consider a power system with *n* generators and loads interconnected by a transmission network. The dynamics of this power system can be represented by a set of nonlinear differential equations:

$$\dot{x} = f(x) \tag{4.1}$$

where $x \in R^{2n}$ are the state variables. The classical model [1] is used and the loads are modeled as constant impedances. The dynamics of the i-th generator can be represented by the swing equations:

$$\begin{aligned} \dot{\delta}_i &= \omega_i \\ M_i \dot{\omega}_i &= P_{mi} - P_{ei}(\delta) - D_i \omega_i, \quad i = 1, ..., n \end{aligned} \tag{4.2}$$

where D_i and M_i are the damping ratio and inertia constant of machine i. $P_{ei}(\delta) = E_i^2 G_{ii} + E_i(\sum_{k \neq i}^{n} E_k (G_{ik} \cos \delta_{ik} + B_{ik} \sin \delta_{ik}))$ is the electrical power at machine i, E_i is the constant voltage behind direct axis transient reactance, and P_{mi} is the mechanical power. $Y = (Y_{ij})_{n \times n} = (G_{ij} + jB_{ij})_{n \times n}$ is the reduced admittance matrix.

If the center of inertia for all machines is used as the reference (COI format) and uniform damping is assumed, then (4.2) can be transformed into the following system:

$$\begin{aligned} \dot{\tilde{\delta}}_i &= \tilde{\omega}_i \\ \dot{\tilde{\omega}}_i &= (P_{mi} - P_{ei}(\tilde{\delta})) / M_i - P_{COI} / M_T - d_0 \omega_i \\ & \qquad\qquad i = 1, \ldots, n \end{aligned} \tag{4.3}$$

where

$$\tilde{\delta}_i = \delta_i - \delta_0 \qquad \delta_0 = (\sum_k^n M_k \delta_k) / M_T$$
$$\tilde{\omega}_i = \omega_i - \omega_0 \qquad \omega_0 = (\sum_k^n M_k \omega_k) / M_T$$
$$M_T = \sum_k^n M_k \qquad d_0 = D_i / M_i, i = 1, \ldots, n$$
$$P_{COI} = \sum_k^n P_{mk} - \sum_k^n \sum_j^n (E_k E_j G_{kj} \cos \tilde{\delta}_{kj} - E_k E_j B_{kj} \sin \tilde{\delta}_{kj})$$

To analyze the transient stability of a power system, as mentioned in Chapter 1, three stages of systems dynamics must be considered, as illustrated in Figure 1.1. This can be mathematically described as follows:

1. Pre-Fault

In the pre-fault stage, the system is operating at x_s^{pre}. The dynamics of this stage is described by:

$$\dot{x} = F_1(x), \quad t < 0, \quad x \in R^{2n} \tag{4.4}$$

where $x_s^{pre} = x(0)$, and state variables are machine angles and angular speeds.

2. Fault-On

At $t = 0$, the system experiences a large disturbance and enters the fault-on stage whose dynamics are governed by

$$\dot{x} = F_2(x), \quad x(0) = x_s^{pre}, \quad 0 \le t < t_{cl} \tag{4.5}$$

where t_{cl} is the time when the protective system is activated.

3. Post-Fault

When the fault is cleared, the system enters the last stage whose dynamics are described by equation (4.6). In this stage, the system is assumed to have a post-fault SEP at x_s^{post}.

$$\dot{x} = f(x), \quad t \geq t_{cl} \tag{4.6}$$

By using the stability-region framework as elaborated in Chapter 1, the mathematical expression for checking the transient stability of the post-fault system is:

$$x(t_{cl}) \in A(x_s^{post}) \tag{4.7}$$

4.2.2 Critical machines and generation rescheduling

Several research studies in [16, 105, 113, 118-119, 122-125] have shown that each generator in a power system can be characterized by its level of relevance and dependence to the overall system transient stability. Some generators can withstand moderate external influences or changes (i.e. power outputs) without significantly affecting the overall system stability. Some machines, on the contrary, are much more susceptible to disturbances, and may cause a significant drop or increase in system stability even when a small change is applied to their configurations. Through the time-domain simulation analysis in [105, 122-123], it can be observed that when a transient instability occurs, these vulnerable or "critical" generators tend to lose their synchronisms first and rapidly separate from the rest of the machines, see Figure 4.1. These machines can be described as being under stress (with reference to system transient stability), and normally a decrease in MW output of these critical machines is likely to improve transient stability of the power system [16, 105, 125]. The main challenge in applying this concept to a practical enhancement control scheme is, "How do we accurately and efficiently identify these critical machines?". Current available methods for identifying critical machines are

based on the observation of system trajectories, heuristics-based approaches [105, 114, 117], and sensitivity-based approaches [16, 118]. Although the results from these methods seem promising, none of them provides a rigorous definition and characterizations of the critical machines. The lack of a rigorous definition of critical machine, as a result, constrains most of these methods to rely only on observations and heuristics approaches. Sensitivity based approaches, while having a sound and systematic way of computing energy margin sensitivities with respect to generation changes, can be computationally expensive to perform.

4.3 Definitions and Characterizations of Critical machines

The general observations of system trajectories in [105, 122-123] have indicated that the critical machines are the group of machines whose rotor angles separate first from the rest of machines and then rapidly diverges. It is crucial to clarify that "first" in this context is in reference to both post-fault integration time and fault clearing time. To elaborate this point, please see the right subfigure of Figure 4.1. Looking only at this figure, we can see that machine # 16 is the first to lose synchronism which occurs at around 0.5 second. This illustrates the first loss of synchronism with respect to the post-fault integration time. The reference to the fault clearing time, on the other hand, can be illustrated by considering both subfigures, which shows that machine # 16 is the first to lose synchronism, occurring at a fault clearing time slightly larger than 0.28 sec (the actual CCT or critical clearing time is 0.285 second). This demonstrates two different types of transitions when the post-fault trajectory moves from being stable to unstable, one with respect to the post-fault integration time, and the other with the fault clearing time. To conclude, as we increase the fault clearing time past CCT, the first group of generators that is observed to lose their synchronism will be considered critical.

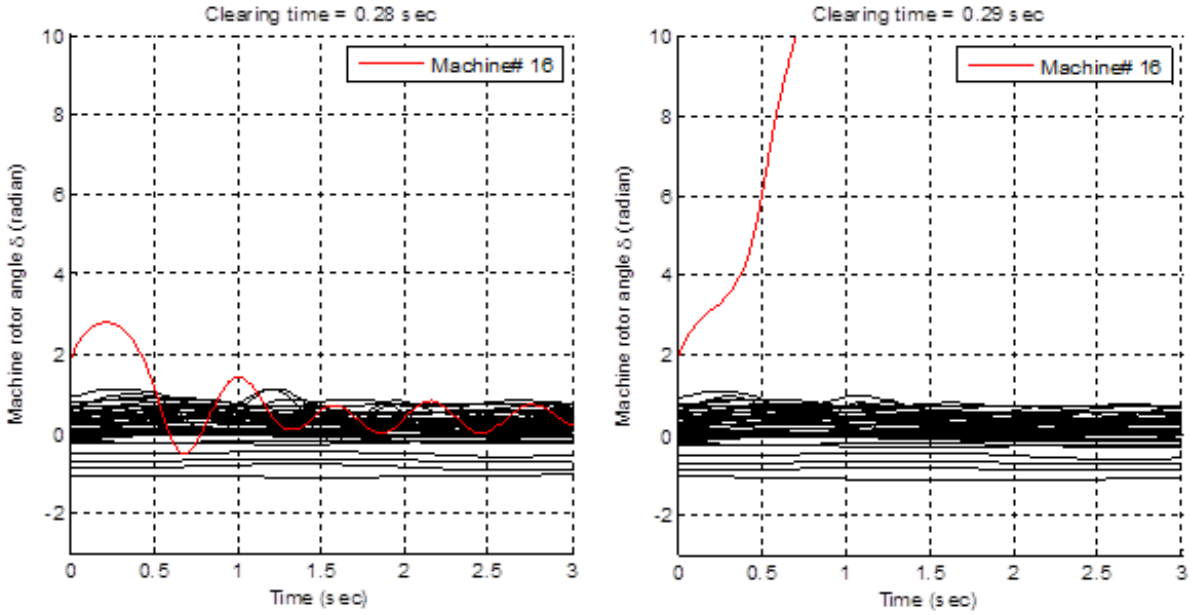

Figure 4.1 An illustration of a critical machine in IEEE145 with 50 generators. Bus# 100 is shorted during fault and line 100-72 is tripped to clear fault. When clearing time is 0.28 sec the post-fault trajectories are stable. Increasing the clearing time to 0.29 sec causes one machine (#16) rotor angle to separate from the group and rapidly diverges.

This leads to the requirement of studying the post-fault system dynamics near the stability boundary in the direction of fault-on trajectory, and therefore the definitions of critically (un)stable post-fault trajectory are given as follows:

Definition 4.3.1 (Critically stable post-fault trajectory)

A critically stable post-fault trajectory is a post-fault system trajectory whose initial point lies just inside the stability boundary of the post-fault SEP. A critically stable post-fault trajectory is considered to be in the direction of a fault-on trajectory if its initial point also lies on the fault-on trajectory (with fault clearing time slightly smaller than CCT).

Definition 4.3.2 (Critically unstable post-fault trajectory)

A critically unstable post-fault trajectory is a post-fault system trajectory whose initial point lies just outside the stability boundary of the post-fault SEP. A critically unstable post-fault trajectory is considered to be in the direction of a fault-on trajectory if its initial points also lies on the fault-on trajectory (with fault clearing time slightly larger than CCT).

The definition 4.3.1 implies that a critically stable post-fault trajectory has a starting point that satisfies the expression (4.7) and hence asymptotically converges to the post-fault SEP. On the other hand, a critically unstable post-fault trajectory has a starting point that does not satisfy (4.7) and therefore either diverges or converges to a different SEP. As mentioned earlier, to find the set of machines that lose synchronism first, it is required that we study the critically unstable post-fault trajectory in the direction of the fault-on trajectory. Based on this concept, the definition of critical machines can be provided as follows:

Definition 4.3.3 (Critical machines with respect to transient stability)

Given a critically unstable post-fault trajectory in the direction of fault-on trajectory (with clearing time slightly larger than CCT), the set of machines whose rotor angles separate from the rest of the machines are the critical machines.

Generally two different types of machine synchronism loss can be observed in the generator swing curves generated by time-domain based software. The distinct behaviors between the two types of synchronism loss are depicted in Figure 4.2 and Figure 4.3. Figure 4.2 shows the case where only one machine loses its synchronism and its corresponding rotor

quickly separates from the rest within a few seconds. Figure 4.3 displays the case where a multiple-machine loss of synchronism occurs. A large number of generators lose their synchronism simultaneously and creates a separation between two comparably-sized groups of generators. The characterizations of the critical machines are given as follows:

1) Critical machines are the set of machines that lose synchronism first, with respect to both post-fault integration time and fault clearing time.
2) Critical machines can be identified from a critically unstable post-fault trajectory in the direction of fault on trajectory.
3) The set of critical machines tend to be either very small in size (one or two) or very large (about half of the machines in the system)
4) Applying a decrease to the generation output on critical machines usually results in an improvement in system transient stability.

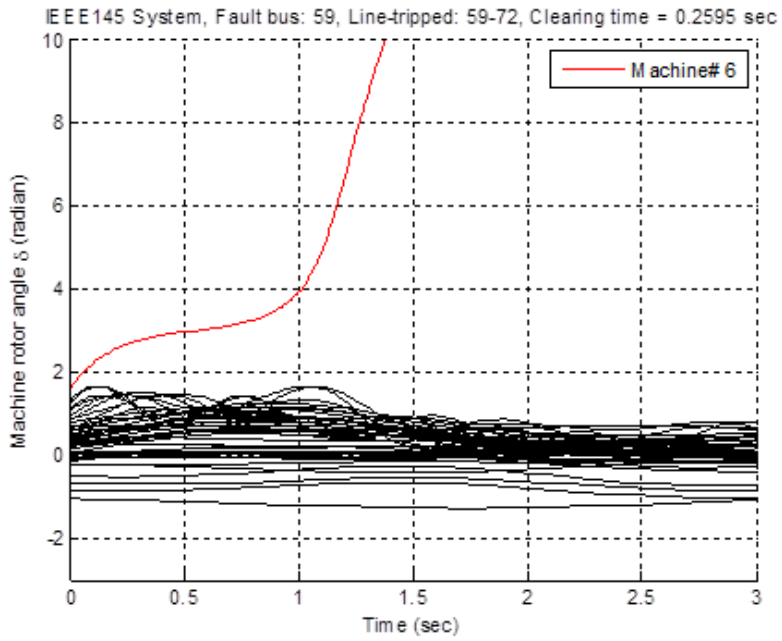

Figure 4.2 Single-machine loss of synchronism

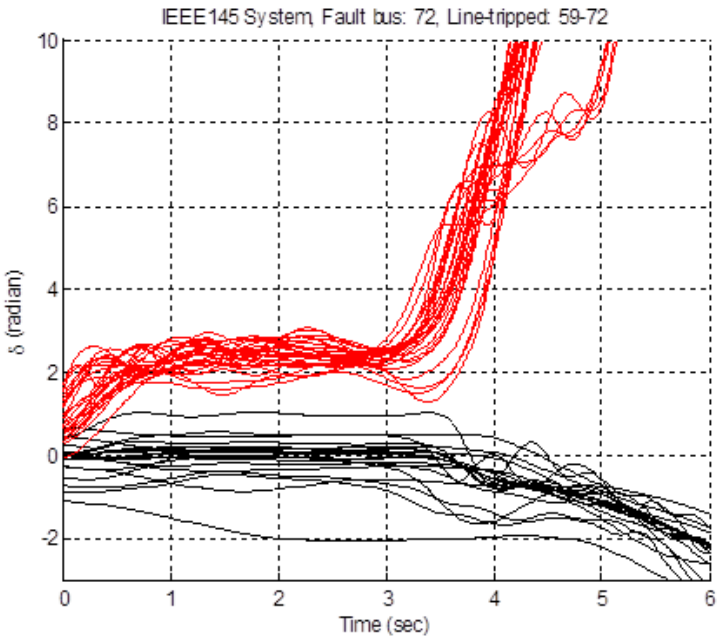

Figure 4.3 Multiple-machine loss of synchronism

4.4 CUEP-based Approach for Identifying and Ranking Critical Machines

It has been shown in [105, 122, 125], that reducing the power outputs of critical machines can significantly improve the system overall transient stability. By incorporating this key guideline into a generation rescheduling scheme, we could design a simple and efficient algorithm for an operation-based enhancement control. The task of computing accurate or exact critical machines, however, has several technical challenges.

1) The full swing curves must be generated in order to observe angle separations and identify the critical machines. This requires a time-domain simulation in the post-fault stage, which is computationally expensive and slow.

2) To identify the exact critical machines, it is required that we compute the critically unstable post-fault trajectory, a trajectory with an initial point lying just outside the stability region. This involves the task of computing the exact stability boundary itself, and therefore requires multiple runs of time-domain simulations.

3) The critical machines are fault dependent, which means that each contingency has a different set of critical machines and requires separate computations. This can be computationally undesirable when practical power systems, which are usually subject to large contingency lists, are considered.

To overcome these computational challenges associated with time-domain simulations, we propose a CUEP-based approach for fast identification and ranking of critical machines. Our approach is based on the stability-region framework in [6, 13] and the integration of the CUEP method into the task of finding critical machines.

It has been established that, in order to compute the critical machines in a power system, a critically unstable post-fault trajectory in the direction of fault-on trajectory must be computed. In other words, using the Definition 2.3.4 (relevant stability boundary), the system dynamics outside the stability region near the relevant stability boundary is needed for identifying critical machines. The study in [6, 7, 9] shows that the dynamics near an equilibrium point in a dynamical system is governed by the stable and unstable manifolds. Applying this key concept to the relevant stability boundary, we may assume that the post-fault dynamics near the relevant stability boundary are governed by the stable and unstable manifold of the CUEP as shown in the Figure 4.4.

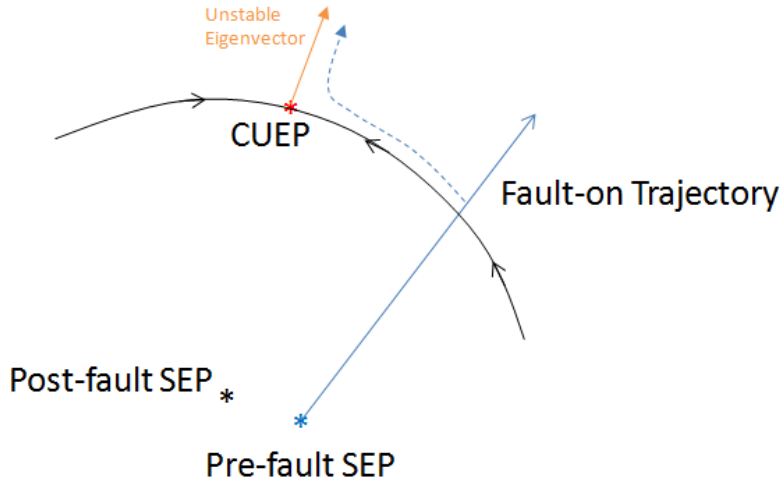

Figure 4.4 The dynamics near the relevant stability boundary

The 1-dimensional unstable manifold of the controlling UEP can then be utilized as a "predictor" to the behavior of the unstable trajectory with a fault clearing time slightly larger than CCT. By performing linearization at the CUEP, the unstable eigenvector of the CUEP can be computed and used instead of the actual unstable manifold for post-fault dynamics prediction, which is more difficult and computationally expensive to compute. The conceptual CUEP-based approach for indentifying and ranking critical machines is as follows:

Given: A contingency with a specified fault-on trajectory and a specified post-fault SEP.

Method: Fast identification and ranking of critical machines

Step 1: Compute the CUEP, x_{CUEP}, of the post-fault system by BCU method [13].

Step 2: Compute the unstable eigenvector(eigenvector corresponding to the eigenvalue with positive real part) at CUEP.

Step 3: Analyze the sign of all components in the unstable eigenvector, and determine the set of critical machines.

Step 4: Analyze the magnitude of all components in the unstable eigenvector, and determine the ranking of machines.

Output: The set of critical machines and ranking of all machines in the system

4.5 Experimental Results

An experimental study is conducted to test the effectiveness and reliability of the proposed CUEP-based approach in identifying and ranking critical machines. Although our framework is based on the well-established theories of stability regions and boundaries [9], the concept of using the unstable manifold of a CUEP, or the corresponding linearized form, as a predictor of the dynamics near relevant stability boundaries is fairly new in the power system literature. Therefore, a thorough experimental investigation is conducted to address the following points:

1) Accuracy of the method in identifying critical machines.
2) Accuracy of the method in ranking critical machines.
3) Effectiveness of the generation rescheduling (based on our rankings) in improving system transient stability

Table 4.1 displays an example of all unstable eigenvector components at a CUEP. The test system is IEEE 145-bus system with constant impedance load model and uniform damping of 0.1. Bus 7 is shorted during fault and line 7-6 is tripped to clear the fault. We can see that only two components (machine# 20 and machine#26) have different signs than the rest, which

according to our predictor, indicates that these two machines are heading towards a different direction than the rest of the machines in the system. When compared to the actual critically unstable post-fault trajectories in the direction of fault-on trajectory in Figure 4.5, the results from our CUEP-based approach match perfectly, as we can observe the rotor angles of machine#20 and #26 are the first to separate from the rest at approximately 4 seconds after the fault is cleared.

Table 4.1: Unstable eigenvector components at CUEP for IEEE145, fault bus is 7 and tripped line is 7-6

Machine	Unstable Eigenvector Component	Machine	Unstable Eigenvector Component
1	-0.028443218	26	**0.086547818**
2	-0.015793744	27	-0.005334443
3	-0.016531533	28	-0.05436711
4	-0.017245319	29	-0.056627207
5	-0.018281657	30	-0.059380572
6	-0.008617586	31	-0.057344028
7	-0.026449223	32	-0.051146504
8	-0.013407089	33	-0.028467887
9	-0.0182035	34	-0.025295965
10	-0.030359916	35	-0.018722806
11	-0.036232103	36	-0.049622151
12	-0.009281323	37	-0.051624615
13	-0.013869813	38	-0.051892653
14	-0.005200714	39	-0.048785046
15	-0.015933339	40	-0.052642076
16	-0.008846032	41	-0.052164134
17	-0.005097949	42	-0.052676523
18	-0.057878286	43	-0.052616318
19	-0.011389872	44	-0.052680081
20	**0.097410128**	45	-0.052636997
21	-0.009084563	46	-0.053095411
22	-0.009184021	47	-0.052751491
23	-0.023995197	48	-0.053703005
24	-0.019245936	49	-0.052374009
25	-0.018666241	50	-0.052705697

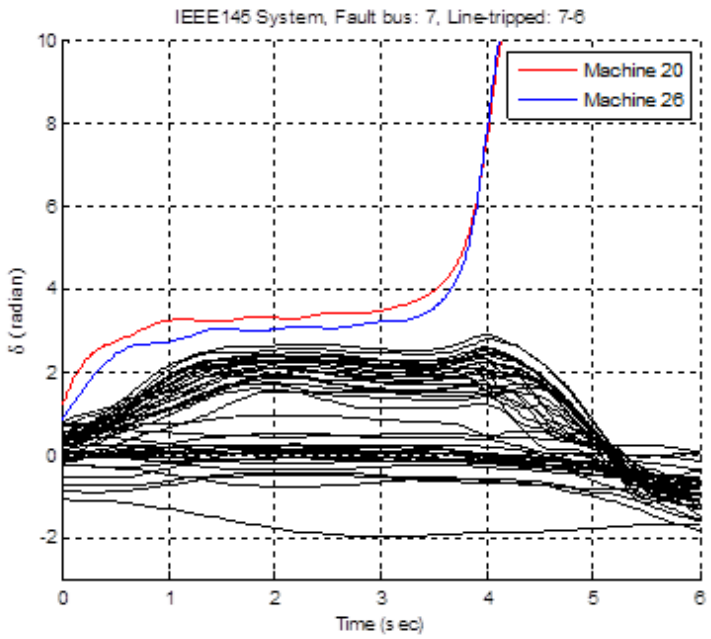

Figure 4.5 Swing curves of a two-machine loss of synchronism.
Fault bus is 7, and line 7-6 is tripped to clear fault.

Table 4.2 presents a numerical study on the IEEE145 system with a consideration of 11 different contingencies. The table presents a comparison of critical machines found by the traditional time-domain approach (by observing critically unstable post-fault trajectory), and our proposed approach using unstable eigenvectors at the CUEP. The results show that the critical machines identified by the unstable eigenvector at CUEP are very accurate when compared to the time-domain approach, especially on the cases with small numbers of critical machines. For the cases with multiple critical machines, the results from the first method are found to be the subsets of those obtained by the time-domain simulation.

The concern regarding the accuracy of the proposed approach in identifying critical machines has been addressed as the numerical results in Table 4.1, Table 4.2, and Figure 4.5 show that the proposed CUEP-based eigenvector predictor can accurately indentify critical machines without having to compute the full swing curves through time-domain simulations.

Table 4.2: Comparison of unstable machines determined by eigen properties and time-domain approach

Contingency	Number	Unstable Machines (by negative components of unstable eigenvector at controlling UEP)	Unstable Machine (by time-domain simulation)
C#1	2	20, 26	20, 26
C#2	2	20, 26	20, 26
C#3	1	6	6
C#4	20	2, 5, 6, 8, 12, 13, 14, 16, 17, 19, 20, 21, 22, 23, 24, 26, 27, 33, 34, 35	1, 2, 3, 4, 5, 6, 7, 8, 9, 10, 11, 12, 13, 14, 15, 16, 17, 19, 20, 21, 22, 23, 24, 25, 26, 27, 33, 34, 35
C#5	1	28	28
C#6	1	29	29
C#7	20	2, 5, 6, 8, 12, 13, 14, 16, 17, 19, 20, 21, 22, 23, 24, 26, 27, 33, 34, 35	1, 2, 3, 4, 5, 6, 7, 8, 9, 10, 11, 12, 13, 14, 15, 16, 17, 19, 20, 21, 22, 23, 24, 25, 26, 27, 33, 34, 35
C#8	1	16	16
C#9	20	2, 5, 6, 8, 12, 13, 14, 16, 17, 19, 20, 21, 22, 23, 24, 26, 27, 33, 34, 35	1, 2, 3, 4, 5, 6, 7, 8, 9, 10, 11, 12, 13, 14, 15, 16, 17, 19, 20, 21, 22, 23, 24, 25, 26, 27, 33, 34, 35
C#10	1	8	8
C#11	1	27	27

C#1: Fault bus is 7, line tripped is 7-6, C#2: Fault bus is 6, line tripped is 7-6
C#3: Fault bus is 59, line tripped is 59-72, C#4: Fault bus is 72, line tripped is 59-72
C#5: Fault bus is 115, line tripped is 115-116, C#6: Fault bus is 116, line tripped is 115-116
C#7: Fault bus is 72, line tripped is 72-100, C#8: Fault bus is 100, line tripped is 72-100
C#9: Fault bus is 75, line tripped is 75-91, C#10: Fault bus is 91, line tripped is 75-91
C#11: Fault bus is 112, line tripped is 112-69

The derivation of machine rankings based on our proposed CUEP-approach will be next evaluated and presented in the following section. The first set of ranking is obtained based on the magnitude that each generator output affects the stability region of the post-fault system. To obtain this ranking, each generator is monitored after two types of adjustments are applied: increase in MW outputs and decrease in MW outputs. The most critical machine is expected to cause the largest shrinkage of the post-fault stability region after an increase in MW output while

the least critical one is expected to cause the largest expansion or the least shrinkage of the stability boundary. The total loads of the system stays constant during the evaluations, meaning that the outputs of all other generators will be adjusted to compensate (equally distributed) the change of the monitored machine. Table 4.3 shows the ranking obtained from this procedure on the IEEE 145-bus 50-machine system. Fault bus is 7 and fault line is 7-6. There are two critical machines where 200 MW increase in generation output causes the stability boundary to shrink (or a decrease in CCT). One is machine 20 and the other is machine 26. Other amounts of MW shifting (i.e. 50 MW, 100 MW and 500 MW) were also tried. The rankings obtained from 50 MW and 100 MW are identical to that of 200 MW, but the result from 500 MW case starts to deviate from the former three. This indicates that the ranking retains its order only within a certain range of adjustments from the original configuration. Negative MW shifting was also performed and it gave the exact opposite ranking as the positive shifting. In other words, an increase in MW on critical machines causes the stability boundary to shrink but a decrease in MW helps expand the stability boundary, which improves the overall transient stability of the system.

Table 4.4 presents three sets of rankings obtained by using three different criteria: 1) CUEP-SEP distance change following 200MW shift, 2) CUEP-SEP vector, and 3) unstable eigenvector at the CUEP. The test system is, once again, the IEEE 145-bus system. Fault bus is 7 and line 7-6 is tripped to clear fault. The CUEP-SEP distance change represents a criterion that is based on a simple measurement of the size of stability region. Using this criterion, the machine that causes the largest decrease in CUEP-SEP distance following a 200MW increase will be considered as the most critical. The criterion based on the CUEP-SEP vector is an experimental approach to test if the CUEP-SEP vector, which is very cheap to compute, can be used in place

of the unstable eigenvector at CUEP to identify critical machines. Using this criterion, the CUEP-SEP vector components are used for ranking based on their signs and magnitudes. Figure 4.9 illustrates how the rankings can be computed. The last criterion is based on our proposed scheme, using the unstable eigenvector at CUEP to identify critical machines and obtain rankings. The components of the unstable eigenvector at CUEP are used to rank the machines based on their signs and magnitudes as shown in Figure 4.9.

Table 4.3: First ranking obtained by monitoring the critical clearing time (CCT) following 200MW shifting

Machine	CCT	Difference	Ranking	Machine	CCT	Difference	Ranking
Original	0.16103				0.16103		
1	0.16159	0.00056	22	**26**	0.15138	**-0.00965**	**2**
2	0.16124	0.00021	4	**27**	0.16141	0.00038	9
3	0.16163	0.0006	29	**28**	0.16169	0.00066	45
4	0.16165	0.00062	32	**29**	0.16174	0.00071	46
5	0.16164	0.00061	31	**30**	0.16179	0.00076	48
6	0.16154	0.00051	15	**31**	0.16176	0.00073	47
7	0.16668	0.00565	50	**32**	0.16158	0.00055	20
8	0.16157	0.00054	18	**33**	0.16153	0.0005	14
9	0.16167	0.00064	41	**34**	0.16145	0.00042	10
10	0.16159	0.00056	23	**35**	0.16133	0.0003	5
11	0.15897	0.00059	27	**36**	0.16154	0.00051	17
12	0.15542	0.00036	6	**37**	0.1616	0.00057	24
13	0.16118	0.00015	3	**38**	0.16161	0.00058	26
14	0.16139	0.00036	7	**39**	0.16158	0.00055	21
15	0.16161	0.00058	25	**40**	0.16165	0.00062	33
16	0.1615	0.00047	11	**41**	0.16166	0.00063	36
17	0.1614	0.00037	8	**42**	0.16167	0.00064	42
18	0.16184	0.00081	49	**43**	0.16166	0.00063	37
19	0.16153	0.0005	13	**44**	0.16166	0.00063	38
20	0.14244	**-0.01859**	**1**	**45**	0.16166	0.00063	39
21	0.16154	0.00051	16	**46**	0.16167	0.00064	43
22	0.16152	0.00049	12	**47**	0.16165	0.00062	34
23	0.16158	0.00055	19	**48**	0.16167	0.00064	44
24	0.16162	0.00059	28	**49**	0.16163	0.0006	30
25	0.16166	0.00063	35	**50**	0.16166	0.00063	40

Table 4.4: Three sets of rankings derived from three different schemes

Machine	CCT	Benchmark (Time-domain) change in CCT	Ranking	SEP-CUEP Distance change	Ranking	CUEP-SEP Vector	Ranking	Eigenvector 1-50	Ranking
1	0.16159	0.00056	22	0.1622	28	0.932626	23	0.028443	26
2	0.16124	0.00021	4	0.6995	40	1.33572	32	0.015794	14
3	0.16163	0.0006	29	0.5257	31	1.332306	31	0.016532	16
4	0.16165	0.00062	32	0.5954	33	1.315365	30	0.017245	17
5	0.16164	0.00061	31	0.6618	34	1.366449	34	0.018282	19
6	0.16154	0.00051	15	0.8517	50	1.598127	47	0.008618	6
7	0.16668	0.00565	50	0.8432	24	1.066556	27	0.026449	25
8	0.16157	0.00054	18	0.7512	45	1.428149	36	0.013407	12
9	0.16167	0.00064	41	0.6798	36	1.521883	38	0.018204	18
10	0.16159	0.00056	23	0.1556	27	0.937584	24	0.03036	28
11	0.15897	0.00059	27	0.8435	25	0.568787	22	0.036232	29
12	0.15542	0.00036	6	0.8444	26	1.543203	40	0.009281	10
13	0.16118	0.00015	3	0.6985	38	1.383417	35	0.01387	13
14	0.16139	0.00036	7	0.8244	49	1.619863	48	0.005201	4
15	0.16161	0.00058	25	0.7001	41	1.539413	39	0.015933	15
16	0.1615	0.00047	11	0.8005	47	1.570652	42	0.008846	7
17	0.1614	0.00037	8	0.7015	42	1.572827	44	0.005098	3
18	0.16184	0.00081	49	-0.2396	23	0.418501	21	0.057878	49
19	0.16153	0.0005	13	0.8008	48	1.557579	41	0.01139	11
20	0.14244	-0.01859	1	-1.4355	1	2.268343	50	-0.09741	1
21	0.16154	0.00051	16	0.7568	46	1.587637	46	0.009085	8
22	0.16152	0.00049	12	0.7476	44	1.583199	45	0.009184	9
23	0.16158	0.00055	19	0.3091	30	1.202679	28	0.023995	23
24	0.16162	0.00059	28	0.5424	32	1.347783	33	0.019246	22
25	0.16166	0.00063	35	0.6782	35	1.51893	37	0.018666	20
26	0.15138	-0.00965	2	-1.0109	2	2.113246	49	-0.08655	2
27	0.16141	0.00038	9	0.6993	39	1.570912	43	0.005334	5
28	0.16169	0.00066	45	-0.3336	15	-0.03091	9	0.054367	46
29	0.16174	0.00071	46	-0.3258	18	0.091006	14	0.056627	47
30	0.16179	0.00076	48	-0.3125	21	0.206075	17	0.059381	50
31	0.16176	0.00073	47	-0.3233	19	0.140746	15	0.057344	48
32	0.16158	0.00055	20	-0.3806	3	0.234133	18	0.051147	32
33	0.16153	0.0005	14	0.2252	29	0.997465	25	0.028468	27
34	0.16145	0.00042	10	0.6805	37	1.052873	26	0.025296	24
35	0.16133	0.0003	5	0.7258	43	1.255958	29	0.018723	21
36	0.16154	0.00051	17	-0.3684	4	0.366518	20	0.049622	31
37	0.1616	0.00057	24	-0.3670	5	0.147101	16	0.051625	33
38	0.16161	0.00058	26	-0.3552	6	0.079247	12	0.051893	34
39	0.16158	0.00055	21	-0.3031	22	0.269738	19	0.048785	30
40	0.16165	0.00062	33	-0.3377	10	-0.17944	7	0.052642	39
41	0.16166	0.00063	36	-0.3417	8	-0.18496	6	0.052164	35
42	0.16167	0.00064	42	-0.3369	12	-0.20236	5	0.052677	40
43	0.16166	0.00063	37	-0.3200	20	-0.52889	1	0.052616	37
44	0.16166	0.00063	38	-0.3340	14	-0.26647	3	0.05268	41
45	0.16166	0.00063	39	-0.3312	17	-0.34654	2	0.052637	38
46	0.16167	0.00064	43	-0.3372	11	-0.10343	8	0.053095	44
47	0.16165	0.00062	34	-0.3414	9	-0.00636	11	0.052751	43
48	0.16167	0.00064	44	-0.3331	16	0.085207	13	0.053703	45
49	0.16163	0.0006	30	-0.3480	7	-0.00745	10	0.052374	36
50	0.16166	0.00063	40	-0.3353	13	-0.22913	4	0.052706	42

It can be observed in Table 4.4 that all three approaches generate different rankings than the one generated by the time-domain approach in Table 4.3. Since the time-domain based rankings is based the actual CCT change caused by each generator, it is considered as the benchmark in our comparison. Figure 4.6-4.8 provide direct comparisons between each set of rankings and the benchmark by the time-domain approach. The diagonal black straight line represents the perfect match with the benchmark. It is clear from these figures that the set of rankings obtained by the unstable eigenvector at CUEP are the most accurate among all three sets of rankings.

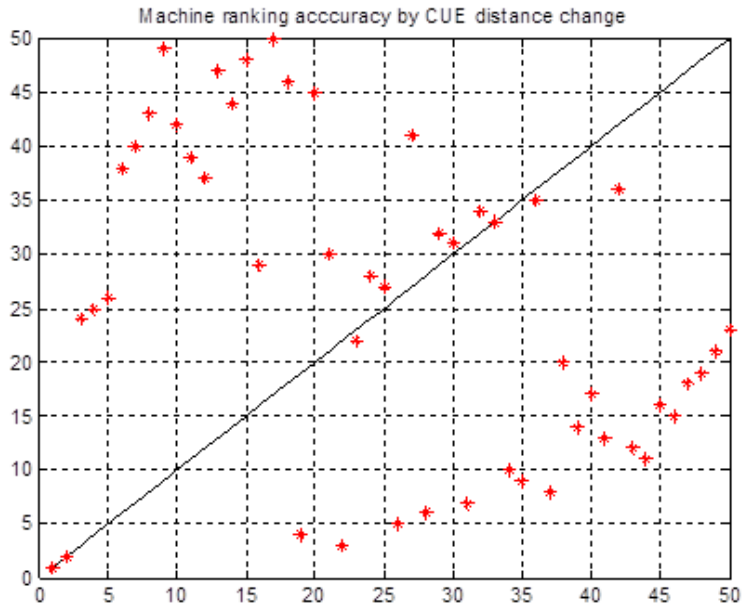

Figure 4.6 Ranking of CUEP-SEP distance approach vs. Benchmark

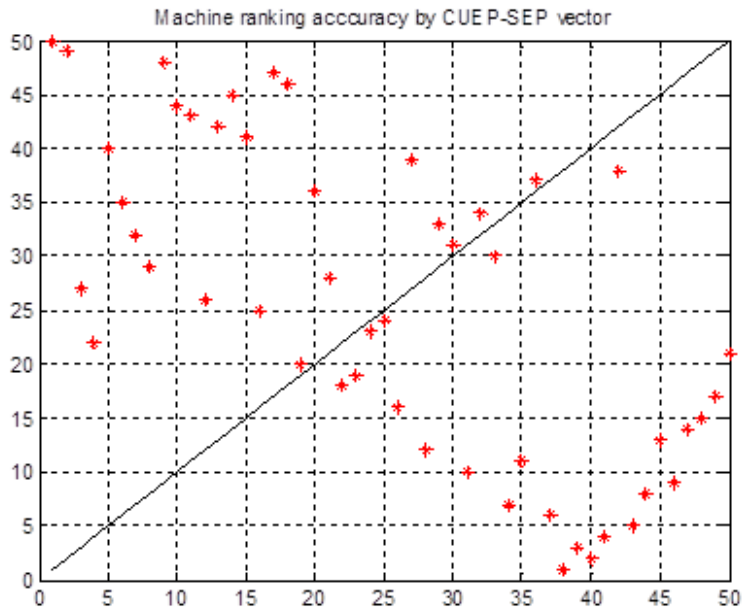

Figure 4.7 Ranking of CUEP-SEP vector approach vs. Benchmark

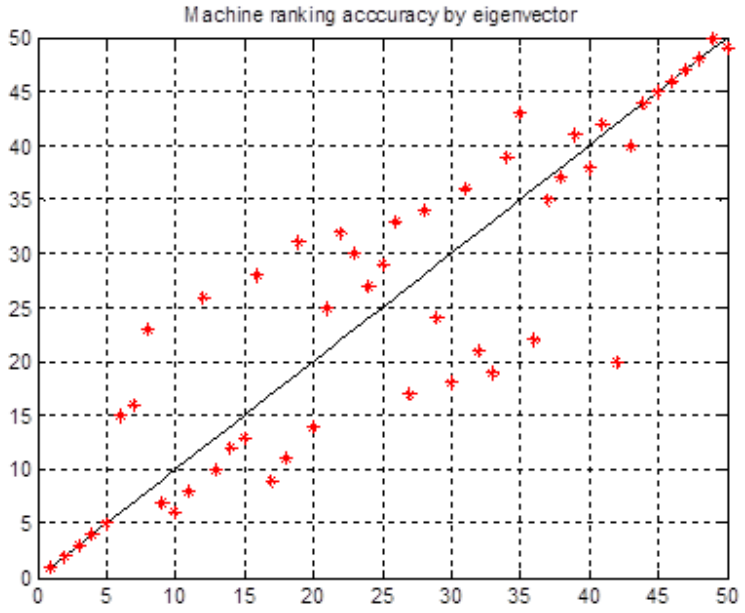

Figure 4.8 Ranking of unstable eigenvector at controlling UEP approach vs. Benchmark

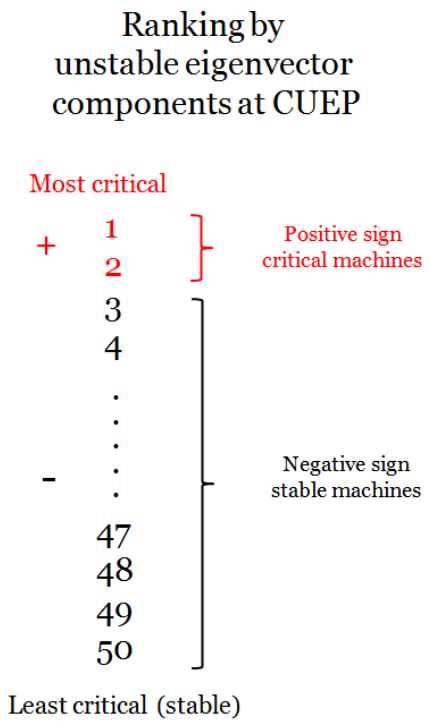

Figure 4.9 Ranking by unstable eigenvector components at CUEP
(or CUEP-SEP vector components)

The numerical comparison in Figure 4.6-4.8 shows that the machine rankings obtained from our CUEP-based approach are fairly accurate when compared to the ranking generated by the benchmark time-domain approach. The main advantage of our method over the time-domain approach is the speed in obtaining the rankings, which makes it much more practical in real world applications.

To improve transient stability via the rankings obtained by our method, the critical machines must be rescheduled to produce less MW outputs, while some non-critical machines have to compensate by increasing their outputs. This process will be referred as *a MW shift*. Figure 4.10 shows the characteristic of critical clearing time CCT as a MW shift is performed. The figure shows the result after an enhancement control, using 1-50 pair (minimal amount of control) to shift power. It also shows that the graph reaches a maximum at 1500 MW shift and

starts to decrease afterwards. This indicates that an over-shifting of MW can also lead to poor CCT improvements. Therefore, a fast assessment tool such as the BCU method should be employed in the algorithm to monitor the CCT at each step of shifting. If a decrease in CCT is detected, the process should stop as the maximum CCT has been obtained. Figure 4.11 shows the performances when other non-critical machines are considered. The performance of rank 31-50 non-critical machines are displayed by black lines, while the results from rank 21-30 and 11-20 non-critical machines are represented by blue and red respectively.

It can be observed that the top 20 most stable or non-critical machines which are represented by black lines have comparable CCT improvement. However, when the lower ranked machines are used for MW shift, we start to get poor results in CCT improvement. This emphasizes the importance of choosing top 20 most non-critical (safe) machines to compensate the critical machines when performing MW shifting.

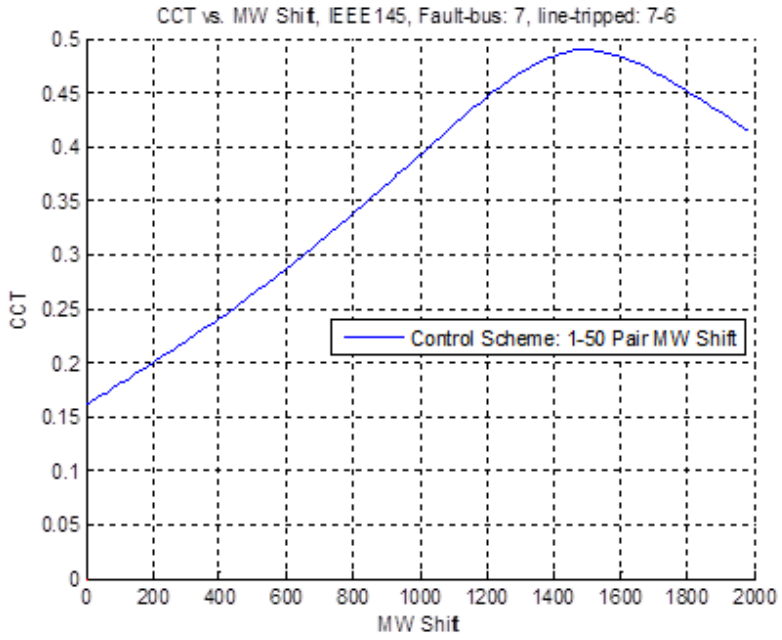

Figure 4.10 MW shift vs. CCT on contingency#1, pair 1-50

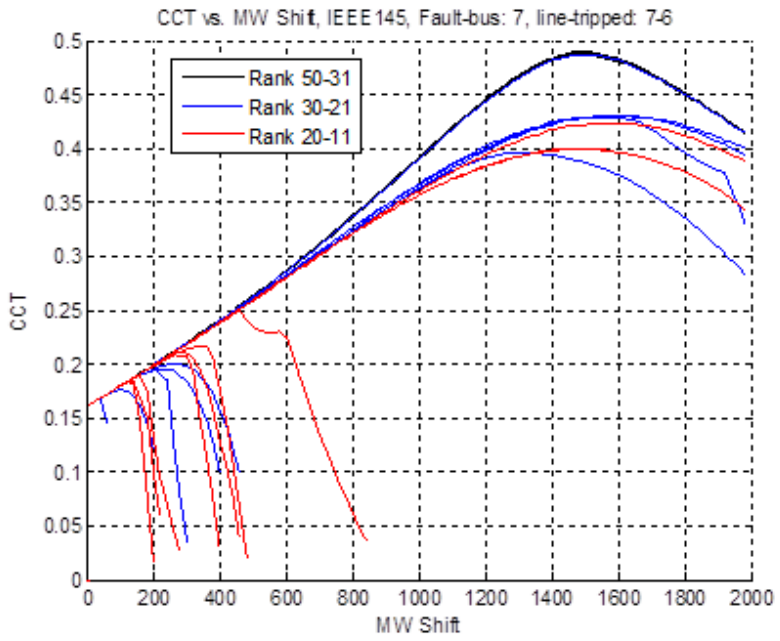

Figure 4.11 MW shift vs. CCT on contingency#1, pair 1-50 through 1-11

4.6 A CUEP-based Enhancement Control Scheme

A CUEP-based enhancement control scheme is proposed in this section. The control scheme is based on the machine ranking computed from the unstable eigenvector at the CUEP. The control scheme can be employed to reconfigure the power dispatch so that the stability of the post fault system can be greatly improved.

Main Control Scheme Generation outputs rescheduling

1. Decrease MW output of critical machines
2. Increase MW output of non-critical(safe) machines to compensate

In order to provide the same amount of MW outputs, some machines need to increase their outputs to compensate the decrease in MW output on the critical machine. Table 4.5 shows the control scheme selection criteria.

The control scheme can be chosen differently depending on the priority according to the system operators. If minimum MW adjustments are of most important, then the rank-one-fifty pair should be used as it usually gives the fastest increase of CCT. On the other hand, if the minimum cost is desired, the system operators can select the pair that are the cheapest and then move on to the next once the first peak is reached. The running time may be longer but the total cost of final configurations will also be cheaper.

Figure 4.12 presents the flow chart of our proposed enhancement control scheme. The main objective of this algorithm is to improve system transient stability as much as the specified control scheme allows. The control scheme box is left undetermined as it can be adjusted to fit the users' preferences. In other words, the users need to specify the pairs to be MW shifted based on their priorities. The program terminates when the largest improvement in CCT has been reached. As a result, the final result should give a new generation dispatch in which transient stability is significantly improved. This algorithm has been implemented and run on IEEE 145-bus system with ten different contingencies. The results can be found in Table 4.6.

Table 4.5: Different control scheme criteria and control actions

Scheme Criteria	**Machine to Decrease MW**	**Machine to Increase MW**
1. Minimal number of controls (machines)	1 most critical machine	1 non-critical machine (Bottom 20 safest machines)
2. Maximum transient stability	All critical machines	Several non-critical machines (Bottom 20, safest machine)
3. Multiple contingencies	At least one of the critical machines from each contingency	At least one of the non-critical machines from each contingency (Bottom 20, safest machine)
4. Most economical	Generation costs are considered during rescheduling.	

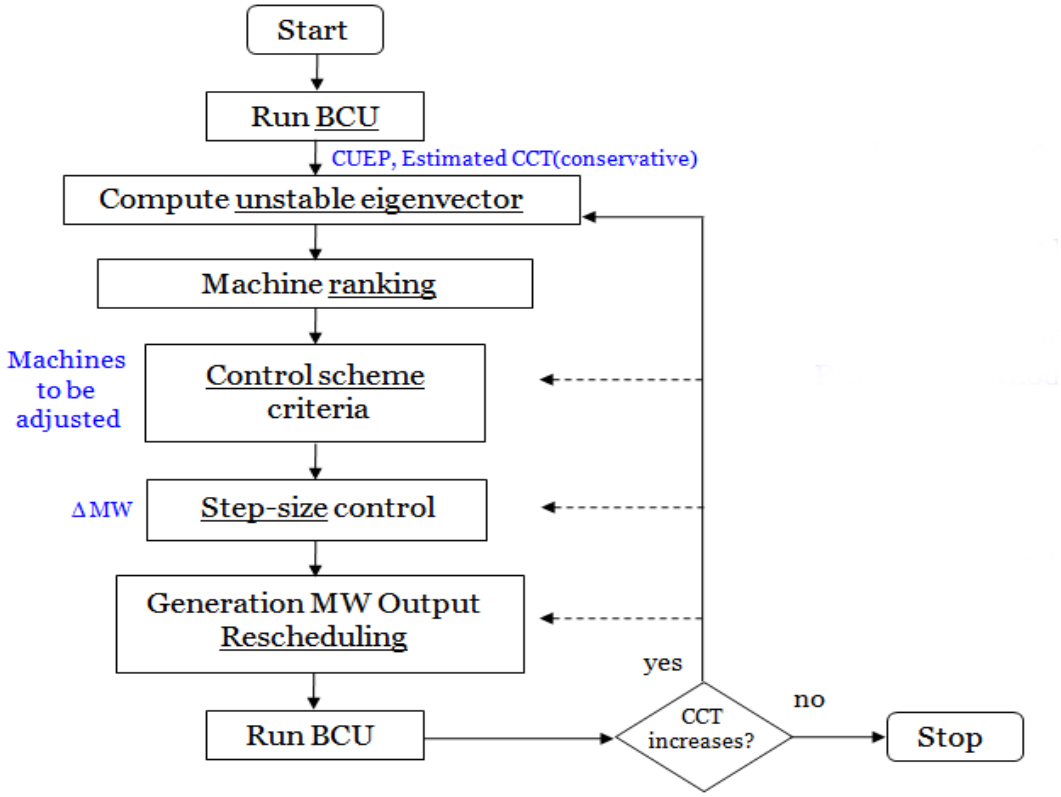

Figure 4.12 Flow chart of the algorithm for transient stability enhancement

Table 4.6: CCT improvements in IEEE 145-bus system by MW shifting of rank-one-fifty pair

Contingency #	Fault- bus: fault-line	Original CCT	Maximum CCT after enhancement controls	% Improvement
1	7: 7, 6	0.16103	0.48921	203.8 %
2	59: 59, 72	0.25914	0.43190	66.67 %
3	112: 112, 69	0.27209	6.0462	2122.13%
4	91: 91, 75	0.29763	0.53721	80.5%
5	6: 6, 1	0.17822	4.39887	2368.22%
6	12: 12, 14	0.33291	0.53222	59.87%
7	6: 6, 10	0.26490	3.29890	1145.34%
8	33: 33, 49	0.21777	0.41671	91.35%
9	69: 69, 32	0.13749	0.31002	125.49%
10	105: 105, 73	0.19812	0.26773	35.14%
11	59: 59, 103	0.23701	5.67811	2295.726%
12	66: 66, 8	0.30105	2.33595	675.93%

4.7 Conclusions

A new CUEP-based method for large-scale power system transient stability enhancement is developed and tested in this chapter. The method consists of three main procedures: (1) fast CUEP computations and CCT analysis by the BCU method, (2) identification and ranking of critical machines via a CUEP-based approach, and (3) control actions by generation output rescheduling. Unlike other existing methods, our method identifies and ranks critical machines using a stability-region based framework which considers the actual dynamics near the relevant stability boundary.

Numerical tests were conducted on 12 different contingencies of the IEEE 145-bus 50-generator system. The numerical results show great accuracy regarding the identification and rankings of critical machines, fast computational speed, and significant improvement in system transient stability.

The main features and advantages of our proposed methods are listed as follows:

1) Fast identification and ranking of critical machine, especially when using in conjunction with a BCU method.
2) Accurate identification and ranking of critical machines, based on system actual dynamics.
3) Does not rely on the fault assumption that the mode of CUEP does not change after generation rescheduling.
4) Inexpensive and simple derivation of control actions.
5) Can be applied to more detailed power system models

It should be pointed out that the direct application of a transient stability enhancement control using generation-rescheduling only addresses the dynamic security problem, whereas in some practical situations, we are required to take into account other types of limits (i.e., thermal, voltage, etc.) and economics. Thus, in the next Chapter 5, we present critical numerical studies on the existing transient stability-constrained optimal power flow (TSCOPF) methods, exploring their strengths, weaknesses, and also the possibility for further improvement. In Chapter 6, we propose a novel TSCOPF method as an alternative control measure that is more suitable for transient stability enhancement/preventive control problems with additional conditions and constraints.

CHAPTER 5

Evaluation Study of the Incorporation of Transient Stability Constraints into Optimal Power Flow

An extensive study of a widely used fixed-threshold proxi for expressing transient stability constraints in optimal power flow is conducted. The purpose of this work is to examine the accuracy and reliability of this proxi in enforcing transient stability constraints into OPF problems. An evaluation method is proposed for computing the exact threshold value of a power system. It is shown via numerical studies that the exact threshold value of the proxi for each system and contingency is in fact not a constant. It can vary from 80 to 190 degrees, depending on several factors such as contingencies, loading conditions and network topology. Further numerical study shows that using the same threshold value for every system, as suggested in the literature, can lead to both severe underestimate and overestimate assessments. A stability-region framework for TSCOPF is proposed to provide a more accurate expression of transient stability constraints in OPF.

5.1 Introduction

The consideration of transient stability constraints in optimal power flow (OPF) problems has become increasingly important in modern power systems. Transient stability constrained OPF (TSCOPF) is a nonlinear optimization problem subject to a set of algebraic and differential equations. Solving a TSCOPF problem can be challenging due to (i) the differential-equation constraints in an optimization problem, (ii) the lack of a true analytical expression for transient stability in OPF. To handle the dynamics in TSCOPF, the set of differential equations can be

approximated or converted into equivalent algebraic equations before they are included in an OPF formulation. The direct discretization of the differential equations was proposed in [32], and utilized in [34]-[41]. This technique however is subject to inaccuracy and convergence issues due to the approximation and the introduction of large numbers of variables and equations for each time step. Therefore, the functional transformation technique was proposed in [33] to handle differential equations by converting the infinite-dimensional TSCOPF into a finite-dimensional optimization problem. Mathematically, the transient stability of a power system does not have an analytical expression that can be directly incorporated in an OPF formulation. To avoid this difficulty, many researchers use a predefined and fixed threshold for rotor angles as a mean to determine transient stability of the system, see for example [32]-[42]. The value of the thresholds used in the literature usually varies from 100° to 120°, but the explanation on how it is selected is still lacking or nonexistent. Although this proxi may suffice as a simplified criterion, it is not an exact expression of transient stability in power system. Therefore, the results from using this proxi in TSCOPF may be subject to compromises and errors.

In this chapter, we provide a detailed numerical investigation of the widely used fixed-threshold proxi on its performance in enforcing transient stability constraints in TSCOPF. The question of accuracy and reliability from using this fixed-threshold proxi will be addressed through extensive time-domain simulation studies. The computations and analysis of the exact threshold values under different test systems, loading conditions, network topology and contingencies is conducted. To obtain the exact threshold values, this chapter presents an exact method using the framework of stability region. A stability-region framework for TSCOPF is also established to provide a more accurate expression of transient stability constraints in the TSCOPF formulation.

Our evaluation study shows that the exact threshold value is not a constant, as assumed in the literature, and can vary from 80 to 190 degrees. This leads to the following issues related to the current fixed-threshold proxi: (i) the current common threshold values of 100º-120º can be very conservative as the correct value can be as large as 190º, (ii) the common threshold values can also be very optimistic as the correct value can be as small as 80º in some systems, (iii) the exact threshold value is not a constant and depends on contingencies, loading conditions and network topology, and (iv) the integration time of 2 to 5 seconds can be problematic for the cases with multi-swing instability. It is numerically shown that using the same fixed threshold value can lead to both severe underestimate and overestimate transient stability assessments. Instead of using the same predetermined and fixed thresholds in the inequalities of every system and contingency, we suggest using adaptive limits that depend on the overall system dynamics.

5.2 TSCOPF Problem Formulations

The TSCOPF problem can be formulated by incorporating a set of transient stability constraints into the conventional OPF formulation, which can be described as follows:

5.2.1 Conventional OPF formulation

$$\text{Min} \quad f(P_g) \tag{5.1}$$

$$\text{S.T} \quad P_g - P_L - P(V,\theta) = 0 \tag{5.2}$$

$$Q_g - Q_L - Q(V,\theta) = 0 \tag{5.3}$$

$$|S(V,\theta)| - S^{\max} \le 0 \tag{5.4}$$

$$V^{\min} \le V \le V^{\max} \tag{5.5}$$

$$P_g^{\min} \le P_g \le P_g^{\max} \tag{5.6}$$

$$Q_g^{\min} \le Q_g \le Q_g^{\max} \tag{5.7}$$

Where $f(\cdot)$ is an objective function; P_g and Q_g are the vectors of generator active and reactive power outputs, respectively; $P_g^{\max}$ and $P_g^{\min}$ are the upper and lower bounds of real power output while $Q_g^{\max}$ and $Q_g^{\min}$ are the bounds for reactive power output; P_L and Q_L are real and reactive power loads; $P(V,\theta)$ and $Q(V,\theta)$ are the real and reactive network injections; $S(V,\theta)$ is a vector of apparent power across the transmission lines whose thermal limits are restricted by $S^{\max}$; V and θ are the vectors of bus voltage magnitudes and angles with associated lower and upper limits of $V^{\min}$ and $V^{\max}$, respectively. P_g, Q_g, V and θ are the free variables in the problem.

5.2.2 Transient stability constraints

The constraints associated with transient stability consist of swing equations (a set of DAEs) that describe the generator rotor angle deviation after a disturbance and stability limit criteria to determine whether the system is stable.

A. Swing equations

The classical model of a synchronous generator is adopted, and loads are modeled as constant impedances. The rotor angle deviation of the *i*-th synchronous generator can be expressed by differential equations as follows [1]:

$$\begin{aligned} \dot{\delta}_i &= \omega_i \\ M_i\dot{\omega}_i &= P_{mi} - P_{ei}(\delta) - D_i\omega_i, \quad i = 1,...,n \end{aligned} \tag{5.8}$$

where, $P_{ei}(\delta) = E_i \sum_{k=1}^{n} E_k (G_{ik}\cos\delta_{ik} + B_{ik}\sin\delta_{ik})$ is the electrical power at machine i, E_i is the constant voltage behind direct axis transient reactance. D_i and M_i are the damping ratio and

inertia constant of machine i. and P_{mi} is the mechanical power. $Y = (Y_{ij})_{n\times n} = (G_{ij} + jB_{ij})_{n\times n}$ is the reduced admittance matrix.

B. Stability region

A stability-region framework is proposed to provide a more accurate expression of transient stability constraints in the TSCOPF formulation. Let us consider a general nonlinear dynamical system described by:

$$\dot{x} = f(x) \tag{5.9}$$

An *equilibrium point* is a solution to the equation $0 = f(x)$. An *asymptotically stable equilibrium* point x_s of (5.9) is the point where all the eigenvalues of the Jacobian matrix have negative real parts. The flow or trajectory of the system (5.9) is the solution to (5.9) at time t starting at x, and it is denoted by $\phi(t, x)$. The stability region of an asymptotically stable equilibrium point (SEP) x_s can be expressed as:

$$A(x_s) = \{x : \phi(t, x) \to x_s, \quad \text{as } t \to +\infty\} \tag{5.10}$$

To analyze transient stability due to a fault, the system is considered to go through three stages: pre-fault stage, fault-on stage and post-fault stage. The fundamental issue of transient stability analysis is whether the system trajectory, starting at the post-fault initial state $x(t_{cl})$, will settle down to x_s^{post}. Transient stability analysis is to determine whether the initial point of the post-fault trajectory is located inside the stability region of the equilibrium point x_s^{post}. It can be mathematically expressed by checking the following condition:

$$x(t_{cl}) \in A(x_s^{post}) \tag{5.11}$$

To be practical we let N be the set of the contingencies being considered in a TSCOPF problem, and $A(x_{si}^{post})$ $i \in N$ denotes the stability region of x_{si}^{post} associated with the contingency *i*. Then the mathematical expression of the transient stability constraints in TSCOPF based on the stability-region framework can be described as follows:

$$x_i(t_{cl}) \in A(x_{si}^{post}) \quad \forall i \in N \tag{5.12}$$

In summary, the TSCOPF problem can be formulated as follows:

$$\begin{array}{ll} \text{Min} & (5.1) \\ \text{S.T} & (5.2)\text{-}(5.7) \\ & (5.8) \text{ and } (5.12) \end{array} \tag{5.13}$$

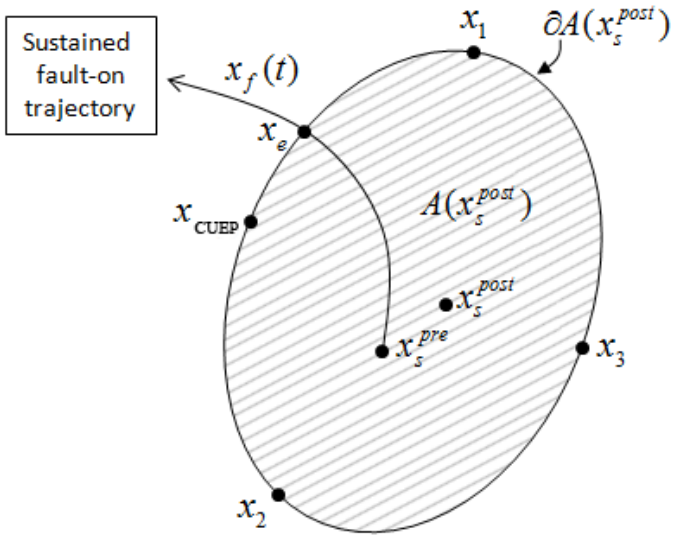

Figure 5.1 The sustained fault-on trajectory $x_f(t)$ moves towards the stability boundary $\partial A(x_s^{post})$ and intersects it at the exit point, x_e. The exit point lies on the stable manifold of the controlling UEP, x_{CUEP}

5.3 Proxi for Transient Stability Constraints and Numerical Issues

Solving a TSCOPF problem as formulated in (5.13) can be very challenging because (i) there are infinite-dimensional variables, equalities and inequalities associated with the swing curves (5.8), and (ii) the expression in (5.12) does not have a closed-form analytical expression. To avoid these two numerical difficulties, many researchers consider the transient stability constraints in TSCOPF through discretized swing curves [32], [34]-[41] and constrain the relative rotor angle within a predefined limit [32]-[42]. By using the implicit trapezoidal rule [32] or Taylor series expansion, differential equations can be discretized and converted into numerically equivalent algebraic equations, which can be easily included in the OPF formulation. The following criterion is widely used in TSCOPF research as a proxi for ensuring system transient stability.

$$\begin{gathered} \left|\delta_i(t)-\delta_{COI}(t)\right|_{\max} \le \delta_{\max} \\ 0 \le t \le t_{\max} \end{gathered} \tag{5.14}$$

where $\delta_i(t)$ is the rotor angle of machine *i* at time *t*. $\delta_{COI}(t)$ is the center of inertia (COI) reference angle. $\delta_{\max}$ is a fixed angle threshold, normally set between 100° - 120°. $t_{\max}$ is the total integration time. In TSCOPF, $t_{\max}$ is typically set to 2-5 seconds. This constraint requires the rotor angle deviation of all machines, with respect to the center of inertia, to be no greater than $\delta_{\max}$ at all time. If the condition is satisfied, the operating point is considered stable.

Although the proxi (5.14) has been commonly used in the TSCOPF formulation, there are several technical and numerical issues that must be addressed:

1. Accuracy and validity of the criterion – The inequality criterion in (5.14) is merely an approximated and simplified form of the real expression of transient stability in (5.12).

Moreover, the predefined thresholds, or $\delta_{\max}$ in (5.14), are heuristically chosen and vary considerably from 90° to 140° in the literature [32]-[42].

2. Computational burden – The discretization of the differential equations introduces a large number of new equations and variables for each time step. The number increases greatly when multiple contingencies or a longer integration duration is being considered.
3. Convergence – A large number of constraints and variables may cause a TSCOPF program to diverge.
4. Scalability – Although in theory this guideline can be extended to consider multiple contingencies or detailed generator models, it is computational impractical due to the extra computational burden.

We will address the issue of accuracy and, to a certain extent, address the issue of computational burden.

5.4 Method for Computing Exact Thresholds

An exact method is proposed to compute the exact thresholds using the framework of stability region. The exact threshold represents the highest value of rotor angle deviation, with reference to the center of inertia (COI), such that the post-fault trajectory remains in the stability region of the post-fault system and converges to the post-fault stable equilibrium point. The method for computing the exact threshold values is presented below.

Given: A contingency with a specified fault-on trajectory and a specified post-fault SEP.

Method: Computing exact threshold values for angle inequalities

Step 1: Compute the exact critical clearing time (CCT) in the direction of fault-on trajectory by using a time-domain method.

Step 2: Perform a time-domain numerical integration starting from an initial point with fault clearing time slightly less than the critical clearing time. This step produces a critically stable post-fault trajectory.

Step 3: Identify the maximum angle deviation $\delta_{\max}^{exact}$ along the critically stable post-fault trajectory, which can be found at the highest or lowest peak of the trajectories.

Output: The exact threshold of the contingency in the context of angle inequality (5.14) is $\delta_{\max}^{exact}$.

One distinguished feature of the proposed method is that it reflects the network topology, loading conditions, etc. and is based on the exact relevant stability boundary of the transient stability models [6]. It has been observed from our numerical results that the peak value of the angle deviations of post-fault trajectories strictly increases as the fault clearing time increases. The simulation results summarized in

Table 5.1 and Figure 5.2 confirm this observation. This observation shows that the highest rotor angle deviation, or the exact threshold, can be obtained from a critically stable post-fault trajectory whose initial point lies just inside the stability boundary of the post-fault system.

Table 5.1: Clearing times and the peaks of post-fault trajectories WSCC9, fault-bus is 9 and line 9-6 is tripped.

Clearing times	Peak* (degree)
0.2429 = CCT	166.16
0.202	100.00
0.20	98.27
0.15	66.58
0.10	45.95
0.07	37.15

* A peak value represents the maximum amplitude of post-fault trajectories

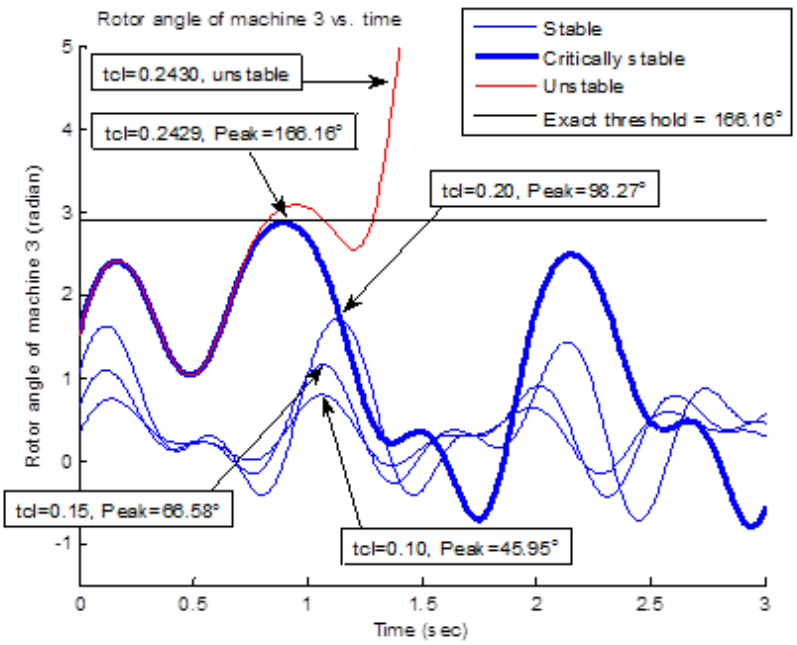

Figure 5.2 The exact threshold value can be obtained at the highest peak of the critically stable post-fault trajectory. The fault-on trajectory crosses the stability boundary at the critical clearing time of 0.2429 second

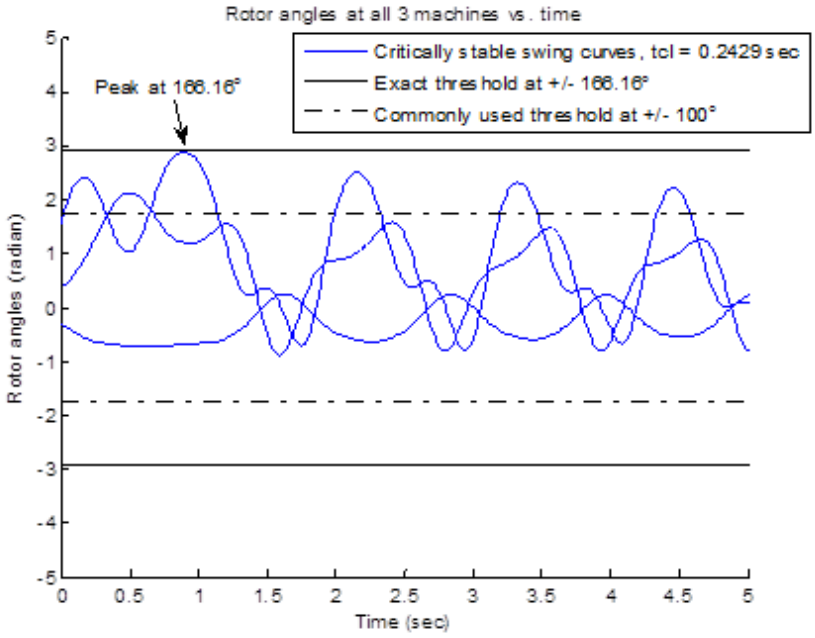

Figure 5.3 Critically stable swing curves when clearing time is 0.2429 second, slightly less than the CCT. The peak of the rotor angles is observed at 2.9 radian or 166.16°.

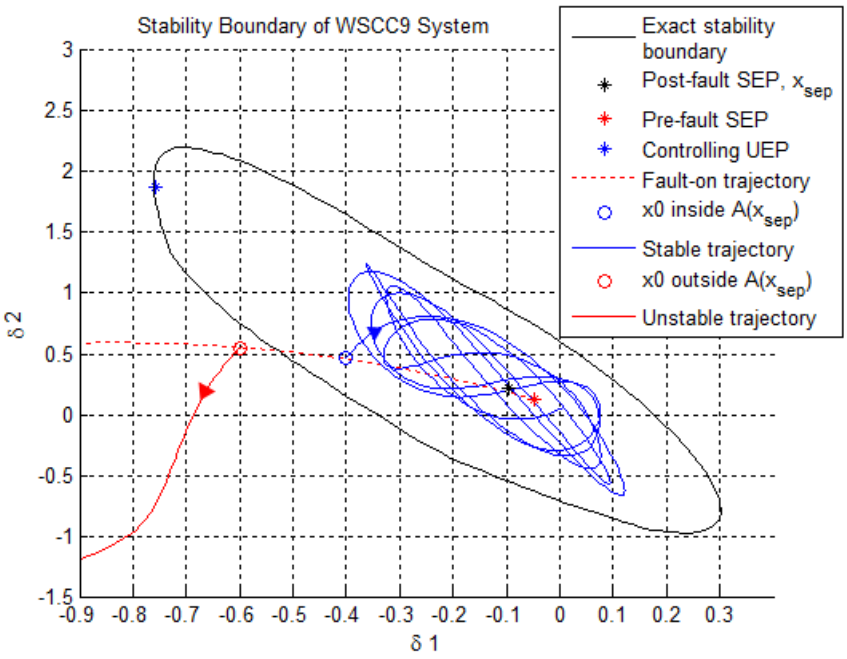

Figure 5.4 A stable trajectory travelling inside the stability region in the state space, while an unstable trajectory lying outside the stability region moves away from it.

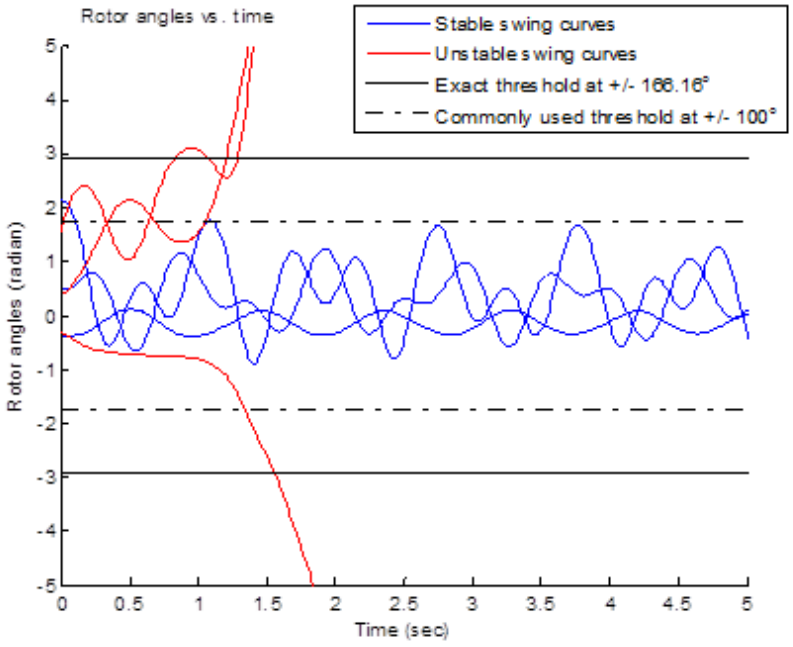

Figure 5.5 The stable swing curves and unstable stable swing curves in Figure 5.4 as a function of time. The exact threshold value of 2.9 radians of 166.16 degrees was found at CCT = 0.2429 second by an exact method, and compared to the commonly used threshold of 100°.

5.5 Proxi from Stability region viewpoint

To address the accuracy issue of using (5.14) in place of (5.12), we present a numerical result showing the performance of the fixed-threshold proxi in estimating the critical clearing times (CCTs). The WSCC9 [2] with constant impedance loads and a uniform damping of 0.1 is considered. Bus 9 is shorted during the fault-on period and line 9-6 is tripped by the protection system. The actual CCT of this system and contingency is 0.2429 second. Figure 5.4 and Figure 5.5 show the same set of post-fault trajectories in different spaces and representations. Figure 5.4 displays post-fault stable and unstable trajectories in the state space, along with the exact stability region of the post-fault SEP. The stable trajectory moves inside the stability region and eventually converges to the post-fault SEP. On the other hand, the unstable trajectory, starting from the outside the stability region, directly diverges to infinity. Figure 5.5 contains the same stable and unstable trajectories as shown in Figure 5.4, however they are represented as swing curves versus time.

Using the proposed exact method, we can obtain a critically stable post-fault trajectory when the fault clearing time is 0.2429 second, and the corresponding exact threshold value of 166.16°, see Figure 5.2 or Figure 5.5. When compared to the exact value, the common fixed-threshold of 100° is very conservative with a relative threshold error of 39.82%. The estimated CCT associated with the 100° threshold is equal to the highest fault-clearing time such that the post-fault trajectories (or the post-fault swing curves) lie entirely in the +/- 100° range. In this contingency, the estimated CCT associated with the 100° threshold is 0.202 second, see Table 5.1. This translates to a 16.84% relative error of estimated CCT by the 100° fixed threshold proxi.

5.6 Numerical Studies on Threshold Values

A time-domain study on the IEEE145 test system [1] was conducted to address the following issues associated with the commonly used fixed-threshold proxi for transient stability constraints in TSCOPF.

1. The predefined threshold value is heuristically selected in the range of 100°-120°, through generalized estimations of swing curves. It will be shown that the exact threshold value of a system can vary from 80° to 190°, depending on several factors such as types of contingency, loading conditions, and network topology. The question is, if the same threshold value is used for every system and contingency, as suggested in the literature, will it affect the accuracy of the proxi in enforcing transient stability in TSCOPF? If it does, how large the errors can be expected?

2. Due to the highly-computational nature of this solution method, longer integration times are undesirable. As can be seen in [32, 36-38], only 2-5 seconds of integration time is chosen and employed to solve TSCOPF problems. This practice may become problematic in the case of multi-swing instability, where the rotor angle separations usually take longer time to occur. We will address this issue and find out the outcomes of using a short integration time along with a fixed-threshold proxi to solve TSCOPF in this situation.

We next show the numerical results on the IEEE145 test system. Loads are modeled as constant impedances and the uniform damping of 0.1 is considered. Bus 7 is shorted during the

fault-on period and line 7-6 is tripped to clear the fault. The actual critical clearing time is 0.1424 second.

5.6.1 Underestimate of threshold and CCT

Figure 5.6 shows a critically stable post-fault trajectory when the fault clearing time is 0.1420 second, slightly lower than the CCT. All 50 machine rotor angles are presented in Figure 5.6. Figure 5.8 displays the displacement from the post-fault SEP to the trajectory. It confirms that this trajectory is stable and asymptotically converges to the post-fault SEP. Figure 5.6 presents an example of a stable trajectory which the TSCOPF criterion in (5.14) with 100° fixed threshold considers unstable. The rotor angles at the following buses are all larger than 100° or 1.7453 radian at some points along the curves: 2, 3, 4, 6, 7, 8, 9, 12, 13, 14, 15, 16, 17, 19, 20, 21, 22, 25, and 26. To confine the whole swing curves in the +/- 100° limits, the fault clearing time has to be significantly reduced to 0.0751 second, see Figure 5.7. We show in

Table **5.1** that the peak value of swing curves strictly increases as the fault clearing time increases. This means that, for this system and contingency, using a 100° threshold is equivalent to restricting the fault clearing time to be equal or less than 0.0751 second. In other words, it is equivalent to having an estimated CCT of 0.0751 second.

Table 5.2 contains the relative errors of CCTs and threshold values when fixed thresholds of 100° or 120° are used in the TSCOPF proxi. This numerical result shows that using a fixed-threshold proxi (i.e. 100°) in TSCOPF can lead to a severe underestimate of the exact threshold and CCT. The relative error for threshold value in this case can be as high as 43.70 %. In the context of optimization problems, this means that a large number of feasible solutions, those that are transiently stable, may be considered unstable and disregarded due to the predetermined threshold value being too small and conservative.

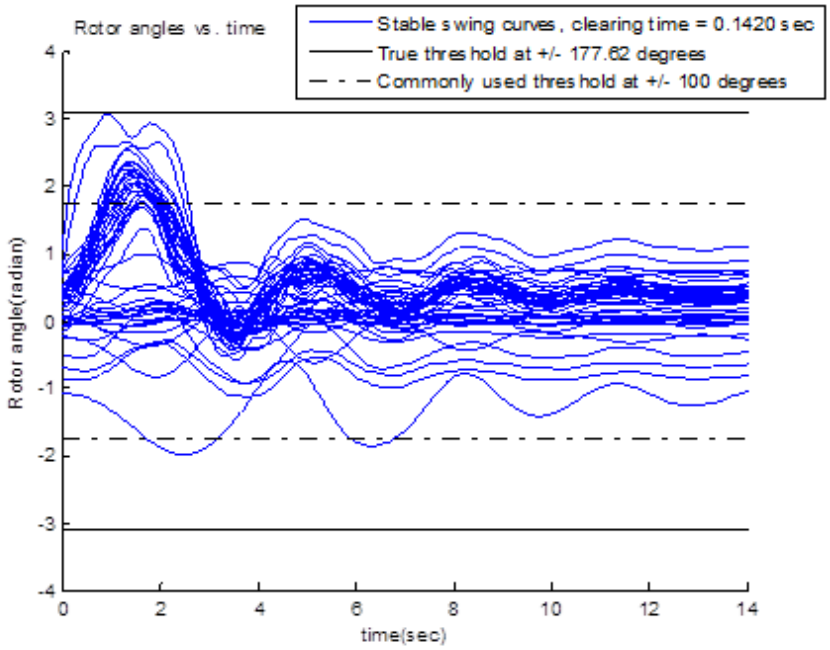

Figure 5.6 At fault clearing time = 0.1420 second, the stable post-fault trajectories are confined in the correct limits of +/- 177.62°.

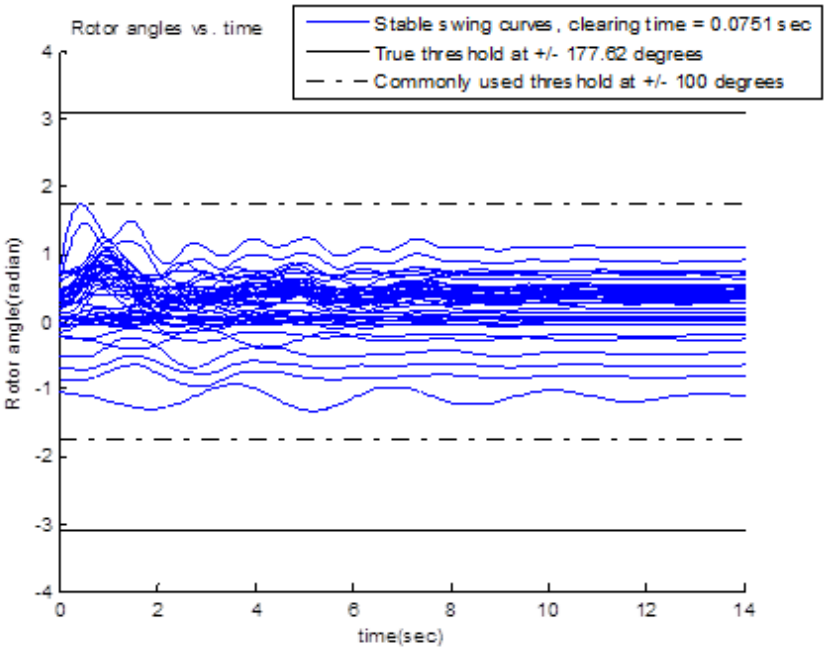

Figure 5.7 At fault clearing time = 0.110 sec, the stable post-fault trajectories are confined in the commonly used limits of +/- 100°.

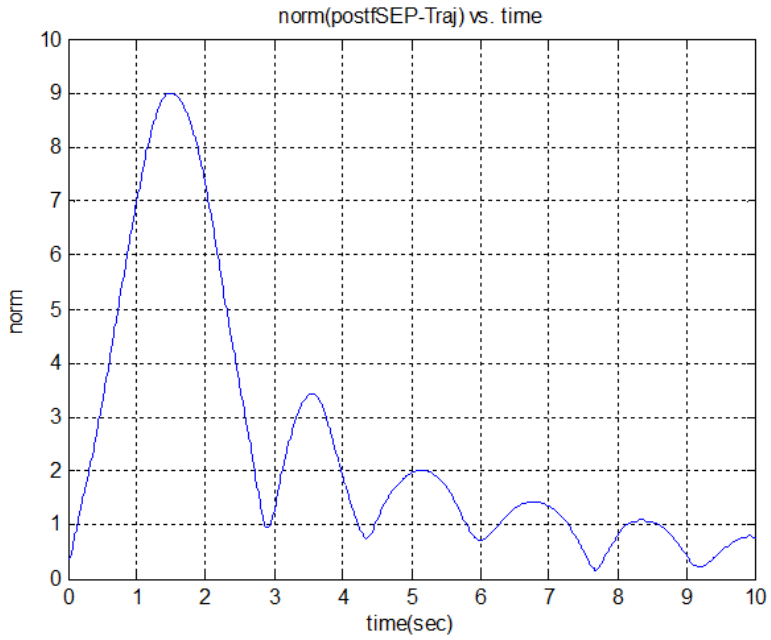

Figure 5.8 Fault clearing time = 0.1420 sec, the post-fault trajectory converges to a post-fault SEP

5.6.2 Overestimate of threshold and CCT

The test system for this example is the IEEE145 with constant impedance loads and a uniform damping of 0.1. Bus 8 is shorted during the fault-on period and line 8-7 is tripped to clear the fault. A high loading condition is considered in this case. The actual CCT is 0.071 second. Using the proposed exact method, we found the exact threshold value of 95°. Figure 5.9 shows a multi-swing unstable swing curve when the fault clearing time is 0.072 second, slightly larger than the actual CCT. It can be observed that the separation of the rotor angles does not occur until after 15 second in the post-fault stage. If the common 100° threshold is considered in (5.14), the violation of the inequality will occur at 17.35 second. This becomes a problem because, as described in section 5.3, the post-fault integration time is normally limited to 2-5 seconds. This means no violation will occur within this period and the angle separation at 17.35 second will not be detected. Using the correct threshold value of 95° will however result in a

correct detection at 2.46 second, see Figure 5.9. This is an example where using a fixed-threshold proxi (i.e. 100°) can lead to an overestimate of CCT, and a false assessment. In the context of optimization problems, this means that some infeasible solutions, those that cause transient instability, may be considered feasible when solving for an optimal solution.

In summary, we present the numerical results to show that if the threshold value in (5.14) is predetermined and fixed for every case and contingency, it may lead to both severe underestimate and overestimate assessments in TSCOPF. It is also shown that using the exact threshold values in, which can be found by the proposed exact method, can eliminate these shortcomings.

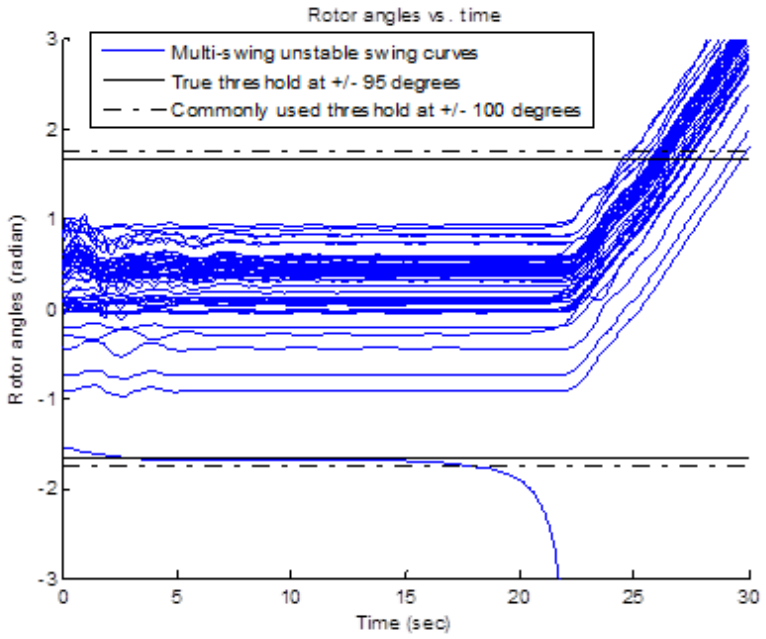

Figure 5.9 A multi-swing unstable post-fault trajectory can take more than 15 seconds before encountering an angle separation.

5.7 Accurate Thresholds Under Different Conditions

It has been shown that the correct threshold value in (5.14) can be different for each system and contingency, and that using a fixed threshold, as suggested in the literature, can lead to an inaccurate proxi for transient stability constraints in TSCOPF. We next examine the exact threshold values under the following different conditions: (i) types of contingencies, (ii) loading conditions, and (iii) severe contingencies. The numerical study on the IEEE145 shows that the exact threshold values vary significantly from 80°-190° under different system conditions. This emphasizes the importance in adjusting $\delta_{\max}$ of (5.14) in accordance to the system's dynamics and contingencies.

A. Type of contingencies

Table 5.3 shows the correct threshold values when different types of contingencies are considered. Since the protection system is normally activated within 5-8 cycles, or 0.0833-0.1333 second after a disturbance, any case with a CCT lower than 0.1 second will be considered insecure. If the CCT lies between 0.1 and 0.2, it will be considered critical. When the CCT is greater than 0.2, that contingency is considered secure. We can see that the threshold values are smallest in the insecure group with the average value of 119.78°, followed by 170.52° of the critical group. The secure group has the highest average value of 176.24°. It can be observed that as the CCT decreases, the threshold tends to decrease in general.

This numerical result shows that true threshold value for each contingency is different and it is related to the value of the critical clearing time. It can be observed that the exact threshold value decreases as CCT decreases.

B. Loading conditions

The effect of loading conditions on the threshold value is studied and presented in Table 5.4. Three contingencies (one from each contingency group) are considered in this study. It can be observed from the results that as loads increase, both CCTs and threshold values strictly decrease. The results are uniform among all three types of contingencies. Note that the insecure contingency contains less data than the other two due to the lowest load margin. The result illustrates how the loading condition has a direct impact on the exact threshold value of each contingency. As loads increase, the exact threshold value also decreases.

C. Severe contingencies

Table 5.5 presents the threshold values of some severe contingencies of IEEE145. Line 17-22 is permanently taken out when the test for other contingencies is run. It can be observed that the exact threshold values of all the cases are below 100°. If the criterion (5.14) is used with a fixed $\delta_{\max} = 100°$, and if the multi-swing instability is taken into consideration, these insecure contingencies may be considered secure by the proxi. To avoid this type of false assessment in TSCOPF, either the integration time must be extended well beyond 5 seconds, or an exact threshold value must be used.

Table 5.2: Relative error percentage of estimated CCTs

	$\delta_{\max} = 100°$	$\delta_{\max} = 120°$
Fixed threshold	100°	120
Exact threshold	177.62°	177.62°
Threshold relative error %	43.70	32.44
Estimated CCT	0.0751	0.1100
Actual CCT	0.1424	0.1424
CCT relative error %	47.26	22.75

Table 5.3: Exact threshold values in different types of contingencies

Contingencies	CCT(sec)	Threshold (degree)
Secure	CCT > 0.2	
59: 59-72	0.2415	174.24
116:115-116	0.2866	192.63
1: 1-2	0.4067	176.47
8: 7-8	1.0596	165.81
11: 9-11	2.4959	172.69
Average threshold = 176.24 degree		
Critical	0.1 < CCT < 0.2	
6: 7-6	0.1671	190.11
7:7-6	0.1424	182.66
104: 7-104	0.1681	195.03
98: 58-98	0.1208	144.10
89: 59-89	0.1402	155.10
Average threshold = 170.52 degree		
Insecure	CCT < 0.1	
17: 17-22	0.0835	139.74
33: 33-34	0.0676	115.22
99: 36-99	0.0419	110.70
2: 2-113	0.0693	113.45
Average threshold = 119.78 degree		

Table 5.4: Exact threshold values in different loading conditions

Loading	CCT(sec)	Threshold (degree)
Secure Contingency: 8:7-8		
Original	1.0596	165.81
+5%	0.7708	164.55
+10%	0.5433	154.13
+15%	0.3686	127.83
+19%	0.166	107.49
+19.5%	0.075	104.11
+20%	0	-
Critical Contingency: 7:7-6		
Original	0.1424	182.66
+5%	0.1167	171.03
+10%	0.0837	145.36
+14%	0.0311	126.28
+15%	0	-
Insecure Contingency: 17:17-22		
Original	0.0835	139.74
+5%	0.0431	119.63
+6%	0.0221	97.92
+7%	0	-

Table 5.5: Exact threshold values in severe contingencies

Contingency	CCT(sec)	Threshold (degree)
Line out: 17-22		
59: 59-72	0.0209	90.46
115: 115-116	0.0198	89.76
1: 1-2	0.0212	92.48
6: 7-6	0.0164	83.23
98: 58-98	0.0173	85.49
89: 59-89	0.0103	79.41
104: 7-104	0.0115	81.69

5.8 TSCOPF Using Different Threshold Values

Through a numerical study on several single-contingency TSCOPF problems, we demonstrate that the TSCOPF solution can be significantly different when different values of threshold in (5.14) are considered. The test system is WSCC9 with a uniform damping of 0.05. The system cost function can be found in [43]. The results show that the objective function values at optimal power flow solutions vary considerably under different fixed threshold values. Figure 5.10 displays the single-contingency TSCOPF solutions associated with three different values of fixed threshold. It can be observed that the objective function can be improved by adjusting the fixed-threshold value in (5.14). The costs are highest when the threshold value is 100°, and gradually decrease as the threshold value is raised. The objective function values appear be the lowest or the best when the threshold value is relaxed to 160°, the highest of the three values we tested. Regarding the system transient stability, the stability requirement is satisfied in all threshold values and contingencies as we can see that the CCTs are all greater than the required 0.20 second. The CCTs however appear to be on the conservative side in all cases, with 100° threshold being the most conservative.

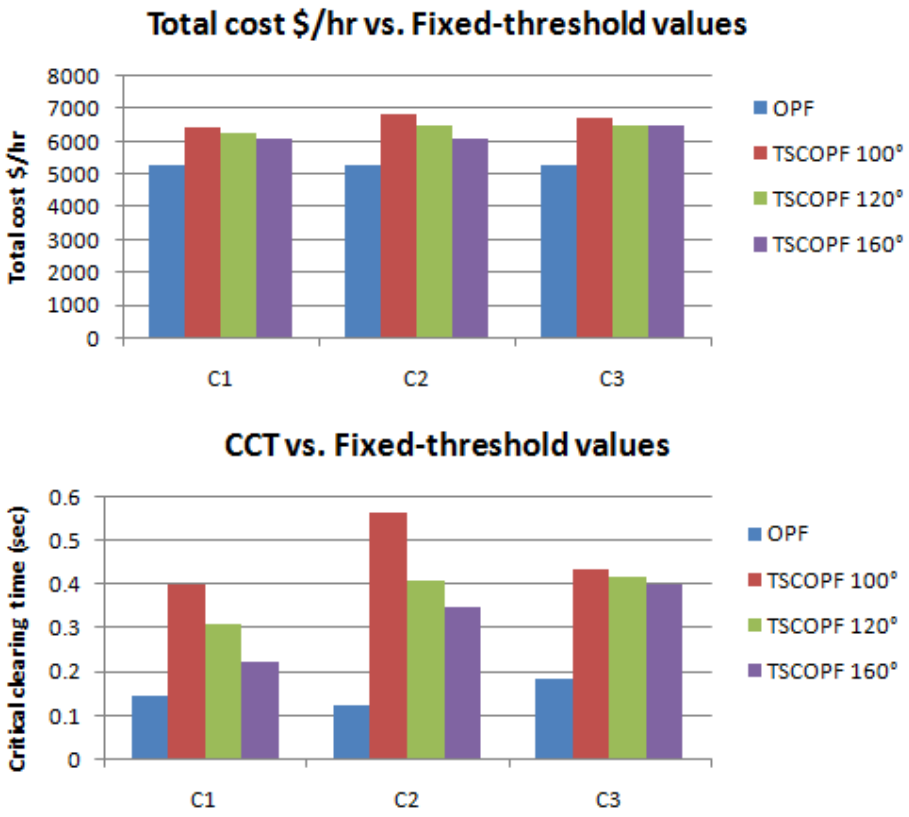

C1 - Fault bus: 9, Tripped-line: 9-6,
C2 - Fault bus: 7, Tripped-line: 7-5
C3 - Fault bus: 9, Tripped-line 9-8.

Figure 5.10 Total generation costs improve as the fixed-threshold value is relaxed (or increased). All CCTs are considerably larger than the required 0.20 second.

This result shows that if the threshold value in (5.14) is chosen without the actual knowledge of system dynamics, it may cause unnecessary conservativeness and degradation of the optimal solution. This demonstrates the importance of adjusting the threshold values in accordance to the dynamics of studied systems. By properly reflecting accurate threshold values, the TSCOPF solutions can be improved without losing system transient stability.

5.9 Conclusions

This chapter provides a critical evaluation of the fixed-threshold proxi for transient stability constraints in TSCOPF. An exact method to determine exact threshold values is developed based on the stability region framework. The proposed method has been applied to derive exact threshold values of power system under different test systems, loading conditions, network topology and contingencies. Our evaluation study shows that the exact threshold values are not constant, as assumed by many researchers [32]-[42], and can vary from 80 to 190 degrees depending on several factors such as types of contingency, loading conditions, and network topology. By using the commonly used fixed-threshold proxi (i.e. 100° or 120°) to express transient stability in TSCOPF, it can lead to severe underestimate assessments as well as overestimate assessments. We also demonstrate that if the threshold value in the proxi is chosen without the actual knowledge of system dynamics, it may lead to unnecessary conservativeness of transient stability and degradations of the optimal solutions.

We emphasize that the current fixed-threshold proxi used in the TSCOPF literature is merely a simplified form of the real expression of transient stability in power systems. Therefore, it may be subject to errors and incorrect assessments. To achieve accurate results in TSCOPF, it is critical that the threshold value is adjusted based on the system dynamics and its loading conditions, and this adjustment should be based on the knowledge of stability regions. The proposed method can meet this requirement.

CHAPTER 6

A Novel BCU-Based OPF Method for Large-Scale Power Systems with Transient Stability Constraints

Transient stability constrained optimal power flow or TSCOPF is a big challenge for power system researchers due to its computational complexity. Even the current best TSCOPF solvers still suffer from the curse of dimensionality, and unacceptable computational time. Moreover, it has been recently shown that the widely used fixed-threshold proxi for enforcing transient stability in TSCOPF can lead to inaccurate assessments as well as degradations of the optimal solutions. In this chapter, we propose a novel BCU-based method to address these issues and to enhance the overall TSCOPF performances. The improvement is achieved through the combination of fast screening by the BCU method, and the computation of accurate system-dependent threshold values. Detailed case studies on several systems up to 678 buses indicate that the proposed BCU-based method can significantly improve (i) the computational speed, (ii) the capability of TSCOPF method to handle large contingency lists, and (iii) the quality of the TSCOPF solutions on both objective function value and transient stability.

6.1 Introduction

Optimal power flow or OPF has been a very important tool in the field of power system operation and planning. Early research on OPF only consider static security constraints in the problem formulation [44], [45], however the resulting dispatches may lead to transient instability under some critical or severe contingencies. To overcome this issue, the transient stability

constrained optimal power flow (TSCOPF) was introduced in [44] and has become a new challenge in the recent years.

TSCOPF can be modeled as a large-scale nonlinear programming problem including the constraints of differential-algebraic equations (DAE). Solving a TSCOPF problem can be challenging due to (i) the differential-equation constraints in an optimization problem, (ii) the lack of a true analytical expression for transient stability in OPF. The direct discretization of the differential equations was proposed in [32], and utilized in [34]-[42]. The functional transformation technique was proposed in [33] to handle differential equations by converting the infinite-dimensional TSCOPF into a finite-dimensional optimization problem. Unfortunately, even the current best TSCOPF solvers still suffer from the curse of dimensionality, unacceptable computational time and memory consumption, especially for large-scale power systems with multiple contingencies [40]. Furthermore, it has been shown in [46] that the widely used fixed-threshold proxi for enforcing transient stability in TSCOPF can lead to both severe underestimated and overestimated assessments as well as degradations of the optimal solutions. To further improve the performance and usability of the discretization-based TSCOPF methods on large-scale practical power systems, it is crucial that the above issues must be addressed and corrected. This paper proposes a novel BCU-based TSCOPF method that overcomes these issues through the combination of a fast screening algorithm by BCU method [13] and a BCU-based computation of accurate system-dependent threshold values.

The BCU method is incorporated in our algorithm to reduce the computational burden by eliminating irrelevant contingencies. It screens out the majority of secure contingencies that do not require control actions, and hence prevents the main TSCOPF solver from considering unnecessary contingencies. A BCU-based approach is proposed to provide an efficient way to

compute system threshold values. Although the method for computing exact threshold values has been proposed in [46], it is based on a time-domain approach which is computationally expensive and impractical for large-scale power systems. To overcome this limitation, a BCU-based scheme is proposed for fast computation of system threshold values. The scheme is tested on several case studies and shown to yield fairly accurate and conservative estimations of the exact threshold values. The CPU times by the proposed BCU-based scheme is shown to be remarkably reduced when compared to the original time-domain-based approach.

The unique features of the proposed BCU-based TSCOPF method are as follows: (uf1) it enables the TSCOPF to solve practical power systems with a large contingency list, (uf2) it provides accurate threshold values which improves the accuracy of transient stability constraints and quality of the TSCOPF solution, (uf3) it can be applied to any discretization- based TSCOPF methods. The numerical results using an interior point method as the main TSCOPF solver show significant improvement in both computational capability and solution quality in all case studies. This promising result shows that the proposed BCU-based method is suitable for solving the solution of large-scale TSCOPF problems that are subject to a large contingency list.

6.2 TSCOPF Problem Formulations

The TSCOPF problem can be formulated as a large-scale nonlinear programming problem associated with DAE constraints [44].

$$\begin{aligned} \min_{\mathbf{x},\mathbf{z}} \quad & f(\mathbf{x},\mathbf{z}) \\ s.t. \quad & \mathbf{H}_0(\mathbf{x},\dot{\mathbf{x}},\mathbf{z}) = 0 \\ & \mathbf{G}_0(\mathbf{x},\dot{\mathbf{x}},\mathbf{z}) \le 0 \end{aligned} \tag{6.1}$$

where vector $\mathbf{x}$ are state variables such as voltage magnitudes and angles, while $\mathbf{z}$ are the control variables such as power outputs, transformer tap ratios, phase shifter positions, etc.

A. Objective function

The objective functions in TSCOPF are generally the same as those in conventional OPF. In this paper, minimization of generation cost functions is considered.

$$f(x) = \sum_{i=1}^{ng} \left(a_i P_{gi}^2 + b_i P_{gi} + c_i \right) \tag{6.2}$$

B. Conventional OPF equality and inequality constraints

1) Power flow equations:

$$\begin{aligned} \mathbf{P_g} - \mathbf{P}_l - P(\mathbf{V}, \boldsymbol{\theta}) = 0 \\ \mathbf{Q_g} - \mathbf{Q}_l - Q(\mathbf{V}, \boldsymbol{\theta}) = 0 \end{aligned} \tag{6.3}$$

where $\mathbf{P_g}$ and $\mathbf{Q_g}$ are the vectors of generator active and reactive power outputs, while $\mathbf{P}_l$ and $\mathbf{Q}_l$ are real and reactive power loads. $\mathbf{V}, \boldsymbol{\theta}$ are the vectors of bus voltage magnitudes and angles.

2) Static security constraints:

$$\begin{aligned} \mathbf{P_g}^{\min} \le \mathbf{P_g} \le \mathbf{P_g}^{\max} \\ \mathbf{Q_g}^{\min} \le \mathbf{Q_g} \le \mathbf{Q_g}^{\max} \\ \mathbf{V}^{\min} \le \mathbf{V} \le \mathbf{V}^{\max} \\ \left| \mathbf{S}(\mathbf{V}, \boldsymbol{\theta}) \right| - \mathbf{S}^{\max} \le 0 \end{aligned} \tag{6.4}$$

C. Transient Stability Constraints

The constraints associated with transient stability consist of swing equations (a set of DAEs) that describe the generator rotor angle deviation after a disturbance, and a stability limit criteria that determines system stability.

In this chapter, the classical model (network-reduction) of a synchronous generator is adopted, and loads are modeled as constant impedances. The rotor angle deviation of the *i*-th synchronous generator can be expressed by differential equations as follows [6]:

$$\begin{aligned} \dot{\delta}_i &= \omega_i \\ M_i\dot{\omega}_i &= P_{mi} - P_{ei}(\delta) - D_i\omega_i, \quad i = 1,...,ng \end{aligned} \tag{6.5}$$

where, $P_{ei}(\delta) = E_i \sum_{k=1}^{ng} E_k (G_{ik}\cos\delta_{ik} + B_{ik}\sin\delta_{ik})$ is the electrical power at machine i, E_i is the constant voltage behind direct axis transient reactance. D_i and M_i are the damping ratio and inertia constant of machine i. and P_{mi} is the mechanical power. $Y = (Y_{ij})_{n\times n} = (G_{ij} + jB_{ij})_{n\times n}$ is the reduced admittance matrix.

A stability-region framework for expressing transient stability constraints in the TSCOPF formulation was proposed in [46]. Let us consider a general nonlinear dynamical system described by:

$$\dot{x} = f(x) \tag{6.6}$$

An *equilibrium point* is a solution to the equation $0 = f(x)$. An *asymptotically stable equilibrium* point x_s of (6.6) is the point where all the eigenvalues of the Jacobian matrix have negative real parts. The flow or trajectory of the system (6.6) is the solution to (6.6) at time t starting at x, and it is denoted by $\phi(t,x)$. The stability region of an asymptotically stable equilibrium point (SEP) x_s can be expressed as [9]:

$$A(x_s) = \{x : \phi(t,x) \to x_s, \quad \text{as } t \to +\infty\} \tag{6.7}$$

To analyze transient stability due to a fault, the system is considered to go through three stages: pre-fault stage, fault-on stage and post-fault stage. The fundamental issue of transient stability analysis is whether the system trajectory, starting at the post-fault initial state $x(t_{cl})$, will settle down to x_s^{post}. Transient stability analysis is to determine whether the initial point of the

post-fault trajectory is located inside the stability region of the equilibrium point x_s^{post}. It can be mathematically expressed by checking the following condition:

$$x(t_{cl}) \in A(x_s^{post}) \tag{6.8}$$

To be practical we let N be the set of the contingencies being considered in a TSCOPF problem, and $A(x_{si}^{post})$ $i \in N$ denotes the stability region of x_{si}^{post} associated with the contingency *i*. Then the mathematical expression of the transient stability constraints in TSCOPF based on the stability-region framework can be described as follows.

$$x_i(t_{cl}) \in A(x_{si}^{post}) \quad \forall i \in N \tag{6.9}$$

Solving a TSCOPF problem using the expression in (6.9) can be challenging because this expression does not have a closed-form analytical expression. As a result, many researchers use predefined and fixed thresholds for rotor angles as a mean to determine transient stability of the system.

$$\begin{gathered} \left|\delta_i(t) - \delta_{COI}(t)\right|_{\max} \le \delta_{\max} \\ 0 \le t \le t_{\max} \end{gathered} \tag{6.10}$$

where $\delta_i(t)$ is the rotor angle of machine *i* at time *t*. $\delta_{COI}(t)$ is the center of inertia (COI) reference angle. $\delta_{\max}$ is a fixed angle threshold, normally set between 100° - 120°. $t_{\max}$ is the total integration time. In TSCOPF, $t_{\max}$ is typically set to 2-5 seconds.

It has been numerically shown in [46] that the exact threshold values are system-dependent, and can vary from 80 to 190 degrees depending on several factors such as types of contingency, loading conditions, and network topology. The results also show that using the same fixed threshold for every system and contingency may lead to severe underestimated and

overestimated assessments as well as degradations of the optimal solutions. Therefore, in this paper, the following stability criterion (6.11) is considered instead of (6.10):

$$\begin{aligned} &\left|\delta_i(t)-\delta_{COI}(t)\right|_{\max} \le \delta^j_{\max}(\mathbf{z}) \\ &0 \le t \le t^j_{\max} \qquad\qquad \forall j \in N \end{aligned} \tag{6.11}$$

where $\delta^j_{\max}(\mathbf{z})$ are the threshold values to be computed on the fly. These thresholds depend on the system control variables $\mathbf{z}$, and each contingency j.

In this paper, the numerical discretization technique is applied to discretize the differential equations into a set of equivalent algebraic equations. Based on the equations (6.2)-(6.5) and (6.11), our TSCOPF formulation can be described as follows:

$$\begin{aligned} \min_{\hat{\mathbf{x}},\mathbf{z}} \quad & f(\hat{\mathbf{x}},\mathbf{z}) \\ s.t. \quad & \mathbf{H}_1(\hat{\mathbf{x}},\mathbf{z}) = 0 \\ & \mathbf{G}_1(\hat{\mathbf{x}},\mathbf{z}) \le 0 \end{aligned} \tag{6.12}$$

where vector $\hat{\mathbf{x}}$ are the new state variables which includes all discretized state variables. The difference between the proposed formulation and the traditional discretization-based TSCOPF formulation is the inclusion of a more accurate expression of transient stability criterion shown in (6.11). Instead of using the same fixed thresholds for every system and contingency in (6.10), (6.11) employs threshold values that reflect system's actual dynamics and contingencies.

6.3 A BCU-based Scheme for Computing System-Dependent Threshold Values

An exact method is proposed in [46] to compute the exact thresholds using the framework of stability region. An exact threshold represents the highest value of rotor angle deviation, with reference to the center of inertia (COI), such that the post-fault trajectory remains in the stability region of the post-fault system and converges to the post-fault stable equilibrium

point. This method, however, requires several numerical integrations to locate exact stability boundary, which can be computational expensive and not suitable for large-scale power systems. The BCU-based scheme for computing system threshold values is proposed to overcome this issue.

Figure 6.1 visualizes the main differences between time-domain-based and BCU-based approaches in computing system threshold values. To obtain an exact threshold, a post-fault trajectory starting from a point lying just inside the stability boundary (point 1) must be computed and analyzed [46]. This exact point 1 however can be very expensive to compute due to the requirement to locate the exact relevant stability boundary in the direction of the fault-on trajectory. This usually requires several numerical integrations. In the same way that a CUEP method can be used to approximate the relevant stability boundary, we can compute point 2 as an approximation of point 1. This scheme is much faster than the time-domain-based approach due to the direct identification of the initial point 2 (for computing system thresholds) via energy surface passing through the CUEP.

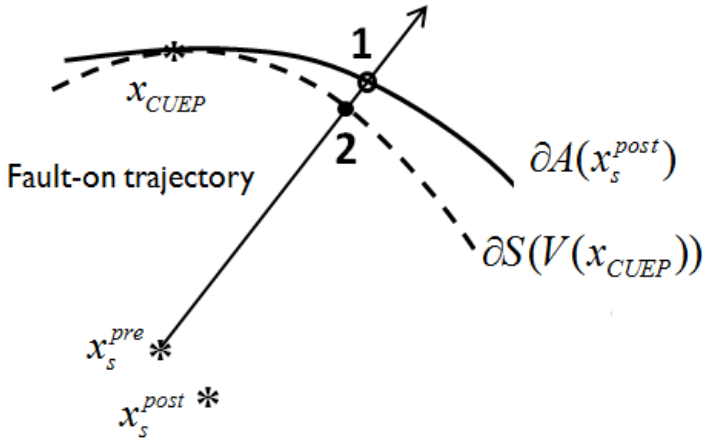

Figure 6.1 Visualization of two initial points for computing system thresholds. Point 1 can be computed by a time domain-based approach while Point 2 by the proposed CUEP-based scheme. System thresholds computed from point 1 leads to an exact value while the results computed from point 2 are estimated and conservative values.

The proposed scheme is presented as follows:

Given: A contingency with a specified fault-on trajectory and a specified post-fault SEP.

Method: Computing threshold values for angle inequalities in the form of (6.11).

Step 1: Compute the CUEP, x_{CUEP}, of the post-fault system by BCU method [13].

Step 2: Find the point along the fault-on trajectory that crosses the energy surface passing through the CUEP, $\partial S(V(x_{CUEP}))$. This point must lie inside the post-fault stability region, $A(x_s^{post})$

Step 3: Find the point along the fault-on trajectory that crosses the energy surface passing through the CUEP, $\partial S(V(x_{CUEP}))$. This point must lie inside the post-fault stability region, $A(x_s^{post})$.

Step 4: Perform a time-domain numerical integration starting from the point computed in step 2. This step produces an estimated critically stable post-fault trajectory.

Step 5: Identify the maximum angle deviation $\delta_{\max}^{est}$ along the critically stable post-fault trajectory, which can be found at the highest or lowest peak of the trajectories.

Output: The estimated system threshold value of the contingency in the context of angle inequality is $\delta_{\max}^{est}$.

The proposed scheme is tested on several case studies and the results are summarized in Table 6.1 and Table 6.2. The tests are performed on three groups of contingencies based on contingency severity. In Table 6.1, it can be seen that the estimated thresholds are uniformly and

slightly smaller than the exact threshold values. The average relative error from all 14 cases is 5.95%. Table 6.2 shows the comparison of CPU time between two approaches. It is clear that the computational times by the proposed CUEP-based scheme are much less than the original time-domain-based approach. The average relative improvement for CPU time is 90.17%. Although the computation has been greatly reduced due to the approximation, the system thresholds estimated by the proposed scheme still reflects the network topology, loading conditions, etc. and is based on the relevant stability boundary of the transient stability models [6].

Table 6.1: Exact (time-domain) vs. Estimated (CUEP) threshold values

Contingencies	TD-based Exact Threshold (degree)	CUEP-based Estimated Threshold (degree)	Relative Error %
Secure	CCT > 0.2		
59: 59-72	174.24	164.11	5.81
116:115-116	192.63	173.3	10.03
1: 1-2	176.47	172.09	2.48
8: 7-8	165.81	151.67	8.53
11: 9-11	172.69	165.7	4.05
Critical	0.1 < CCT <0.2		
6: 7-6	190.11	188.41	0.89
7:7-6	182.66	175.52	3.91
104: 7-104	195.03	175.28	10.13
98: 58-98	144.10	140.34	2.61
89: 59-89	155.10	143.08	7.75
Insecure	CCT < 0.1		
17: 17-22	139.74	133.32	4.59
33: 33-34	115.22	110.47	4.12
99: 36-99	110.70	99.01	10.56
2: 2-113	113.45	104.52	7.87

These numerical studies on the CUEP-based scheme have shown that:

- The threshold values estimated by the proposed scheme are slightly different than the exact threshold values, with fairly small relative errors.
- The threshold values estimated by the proposed scheme are always less than the exact threshold values. This implies conservative estimations by the scheme.
- The computational times are greatly reduced when compared to the original time-domain approach. Over all it is roughly 10 times faster.

Table 6.2: Exact (time-domain) vs. Estimated (CUEP) CPU time

Contingencies	TD-based CPU time (sec)	CUEP-based CPU time (sec)	Relative improvement %
Secure	CCT > 0.2		
59: 59-72	132.48	15.23	88.50393
116:115-116	156.22	16.09	89.70042
1: 1-2	142.48	12.23	91.41634
8: 7-8	135.23	12.1	91.05228
11: 9-11	149.01	17.64	88.16187
Critical	0.1 < CCT <0.2		
6: 7-6	128.46	13.35	89.60766
7:7-6	148.1	15.48	89.5476
104: 7-104	132.09	11.29	91.4528
98: 58-98	133.67	12.31	90.79075
89: 59-89	143.59	16.75	88.33484
Insecure	CCT < 0.1		
17: 17-22	153.27	11.04	92.79702
33: 33-34	147.48	13.58	90.79197
99: 36-99	139.95	12.02	91.41122
2: 2-113	131.3	14.6	88.88043

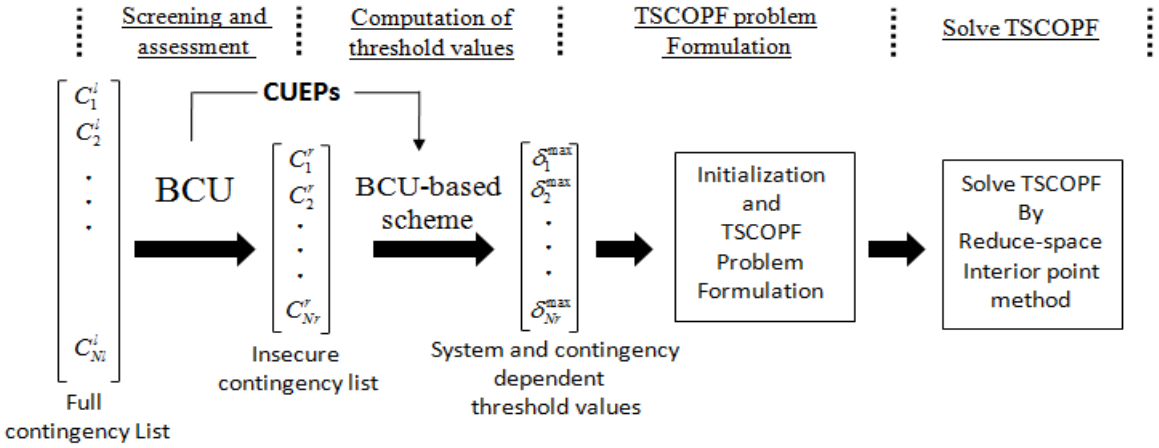

Figure 6.2 The conceptual BCU-based TSCOPF method for large-scale power systems with large contingency lists. The method consists of (i) fast assessment and screening by BCU method for taking out irrelevant contingencies (ii) computation of system and contingency dependent threshold values via a BCU-base scheme, (iii) reduce-space interior point method as the main TSCOPF solver

6.4 The Proposed BCU-based TSCOPF Method

The conceptual algorithm of the proposed BCU-based TSCOPF method is presented in Figure 6.2. The key procedures are listed as follows:

1) Assessment and Screening

Practical large-scale power systems are subject to large contingency lists, but typically only a few are insecure and require control actions. Due to the computation limitation of numerical discretization-based TSCOPF, it is extremely unfavorable to consider a large number of contingencies in the formulation. To prevent these irrelevant or secure contingencies from getting included in the main TSCOPF solver, BCU method [13] is incorporated in the algorithm as a fast screening tool. This ensures that only critical or insecure contingencies are considered by the main TSCOPF solver.

2) Computation of system and contingency dependent threshold values

The importance of using accurate threshold values in (6.11) has been stressed in [46]. The proposed BCU-based scheme is implemented to compute accurate system threshold for each critical or insecure contingency. One advantage of using this scheme along with the BCU method as screening tool is that, the CUEPs are already computed in the screening process, and hence can be readily used by the scheme.

3) TSCOPF problem formulation

The computed threshold values for all critical or insecure contingencies must be incorporated or updated into the main TSCOPF formulation in the form of (6.11).

4) Solve TSCOPF

The reduced-space interior point method is adopted as the main TSCOPF solver in this paper.

Figure 6.3 shows the flow chart of our complete BCU-based TSCOPF algorithm which includes a computational loop that constantly checks and updates the system contingency list and threshold values. Since individual transient stability constraints are typically not binding, it is prudent to begin by solving a standard OPF. The BCU method is then executed to screen out secure cases and provide CUEPs for the computation of thresholds values. Once the threshold values are computed, the main TSCOPF solver is executed to solve the problem. This process repeats until no insecure contingency is found. The procedure is fully described as follows:

Given: A power system case with a contingency list.

Method: Computing TSCOPF solution based on the proposed BCU-based scheme.

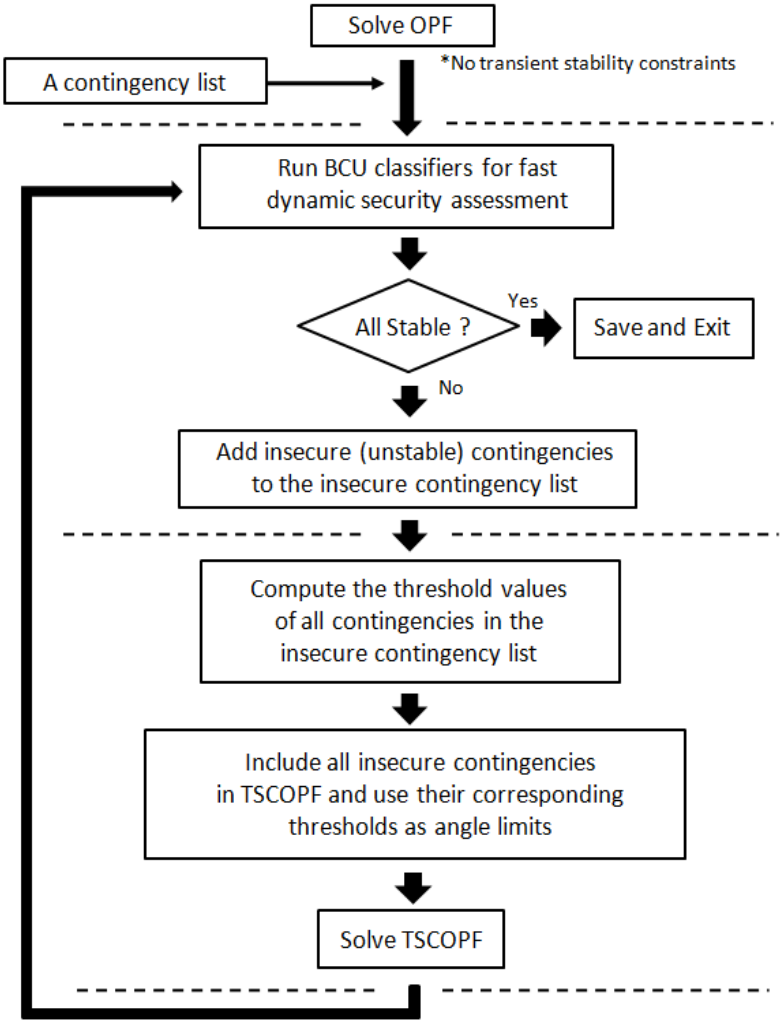

Figure 6.3 The complete algorithm of BCU-Based method for solving large-scale TSCOPF problems

Step 1: Solve standard OPF without considering any transient stability constraints.

Step 2: Run BCU method to filter out screen out secure cases [13]. Save the CUEP's of insecure cases.

Step 3: Check if all contingencies are secure. If yes, end the program and output solution, otherwise proceed to step 4.

Step 4: Update the insecure contingency list by adding the new insecure cases found in step 2.

Step 5: Compute the system threshold of each insecure contingency in (6.11) using the proposed BCU-based scheme.

Step 6: Formulate TSCOPF problem in expression (6.12) using the thresholds computed in step 5.

Step 7: Solve TSCOPF problem by interior point method and repeat step 2.

Output: A transient stability constrained optimal power flow solution.

6.5 Case Studies

Detailed numerical results for different test systems are presented in this section in order to check the robustness and efficiency of the proposed BCU-based method. Table 6.3 gives a summary of these test systems. The reduced-space IPM approach described in [40] was developed to use as the main TSCOPF solver.

In realistic scenarios, it is inevitable that large numbers of contingencies must be considered when TSCOPF problems are solved. Without a fast screening tool within a TSCOPF algorithm, it can be extremely expensive or impossible to perform the computation. Table 6.4 shows the performance of the BCU method in eliminating irrelevant or stable cases. It is clear that the results by the BCU method are very close to those of time-domain approach. Although some stable cases fail to get screened out, the difference is considerably small. Moreover, the computation times taken by the BCU method are much less when compared to the traditional time-domain approach. This confirms that the BCU can greatly reduce the number of contingencies to be included in the main TSCOPF solver.

Table 6.5 shows the comparison between the conventional method and our proposed BCU-based TSCOPF regarding the capability in handling large contingency lists. Both methods utilize interior point method as the main TSCOPF solver. The third and fifth columns show that the conventional approach cannot solve most of the cases while the BCU-based approach is successful in all cases, including 678-bus system with 300 contingencies. The fourth column of Table 6.5 presents the CPU time when conventional TSCOPF is performed along with a time-domain-based approach for screening. It can be seen that the CPU times by the time-domain approach are much higher than the BCU-based approach in all cases. This inferior performance in computational speed by the time-domain approach is mainly caused by the time-consuming numerical integrations of post-fault systems.

The advantage of using accurate system threshold values is presented in Table 6.6. The widely-used fixed threshold proxi with 100° is utilized by the conventional TSCOPF (with TD screening), while the BCU-based TSCOPF approach computes and uses the actual system threshold values. The results show that by using more accurate threshold values, the quality of the optimal solutions of all test systems can be improved by our approach. The resulting objective function values of total generation costs are shown in the Table 6.6. The average improvement on the objective function values is 7.03%.

Table 6.3: Summary of all test systems

Test Systems	N_B	N_G	$T_{\max\ (\mathrm{SEC})}$	Δt
WSCC9	9	3	2.00	0.01
IEEE39	39	10	2.00	0.02
IEEE145	145	50	2.00	0.02
IEEE162	162	25	2.00	0.02
IEEE300	300	69	2.00	0.02
CASE678	678	170	1.00	0.02

N_B = Number of buses, N_G = Number of generators

$T_{\max}$ = Total integration time, Δt = integration step size

Table 6.4: BCU method and screening performance

System	N_l	Contingency screening		
		BCU method Drop-out cases	Time-Domain stable cases	BCU screening Rate %
WSCC9	10	8	8	100%
IEEE39	50	45	46	97.83%
IEEE145	300	293	295	99.32%
IEEE162	300	295	297	99.33%
IEEE300	300	298	299	99.67%
CASE678	300	298	298	100%

N_l is number of contingencies in the contingency list

Table 6.5: Capability to handle large contingency lists:
Conventional TSCOPF (IPM) vs. BCU-based TSCOPF (IPM)

System	N_l	CPU time (sec)		
		Conventional TSCOPF (IPM) *without TD screening	Conventional TSCOPF (IPM) *with TD screening	BCU-based TSCOPF (IPM)
WSCC9	10	1.23	8.41	4.623
IEEE39	50	-	40.33	21.06
IEEE145	300	-	1256.45	538.42
IEEE162	300	-	2696.78	1002.59
IEEE300	300	-	4073.19	1716.44
CASE678	300	-	14493.05	6128.81

N_l is number of contingencies in the contingency list

Table 6.6: Capability to handle large contingency lists:
Conventional TSCOPF (IPM) vs. BCU-based TSCOPF (IPM)

System	N_l	Objective function value at TSCOPF solution		Relative improvement %
		Conventional TSCOPF (IPM) *with TD screening	BCU-based TSCOPF (IPM)	
WSCC9	10	$15,421	$14,031	9.01%
IEEE39	50	$65,330	$61,248	6.25%
IEEE145	300	$203,449	$185,226	8.96%
IEEE162	300	$148,405	$132,110	10.98%
IEEE300	300	$544,095	$523,060	3.87%
CASE678	300	$832,713	$790,432	5.08%

N_l is number of contingencies in the contingency list

6.6 Conclusions

The TSCOPF problem is a big challenge in the field of power system operation. Based on a numerical discretization approach and interior point method, a BCU-based method is proposed for computing the solution of TSCOPF problems. Details of the BCU-based method are discussed, including the BCU-based scheme for computing accurate system thresholds and the implementation of the BCU method as fast screen tool. The key parts of the proposed BCU-based TSCOPF algorithm are as follows:

1) The incorporation of the BCU provides our method a fast and effective tool to screen out irrelevant or secure contingencies. This greatly reduces the computational burden when large contingency lists are considered.
2) The BCU-based approach for computing system threshold provides the TSCOPF solver with accurate system-dependent threshold values. This improves the accuracy in stability assessment as well as the quality of the TSCOPF solution.
3) This method is applicable to any discretization based TSCOPF solvers.

Numerical results on several TSCOPF problems indicated that the proposed BCU-based algorithm could improve (i) the computational speed, (ii) the capability of TSCOPF method to handle large contingency lists, and (iii) the quality of the optimal solutions of every case study. This promising result shows that our proposed method is suitable for solving large-scale TSCOPF problems that are subject to large contingency lists.

CHAPTER 7

Critical Evaluation of Numerical Methods for Approximating the Stability Boundary of Large Power Systems

The analysis of transient stability plays a vital role in providing secured operating configurations in power systems. In this paper, we present a critical evaluation study of several numerical methods for approximating the relevant stability boundary of stable equilibrium points and for directly assessing transient stability. These methods include the PEBS method, the energy function-based controlling UEP method, the hyperplane method and a quadratic approximation approach. A technique for visualizing informative stability regions of stable equilibrium points in high-dimensional power systems is also proposed. The numerical evaluation shows that the energy function-based controlling UEP method is overall the most suitable method for approximating the relevant stability boundary and for assessing transient stability in power systems.

7.1 Introduction

Many computational methods for transient stability analysis in the power system are present in the literature. The time-domain approach is usually considered as a benchmark due to its accuracy in assessing stability and its applicability to any general power system stability model. This method is used by many utility companies around the world to perform transient stability analysis. However, the main disadvantages of this approach are the high computational

burden, the lack of a measurement for the degree of stability, and the absence of useful information for deriving preventive controls.

The direct methods (based on energy functions) [5], [7], [12], [15], [47]-[49] were proposed to overcome the shortcomings of the time-domain approach. By avoiding numerical integration during the post-fault stage, the direct methods require much less computation than the time-domain approach and are more suitable for applications where fast computation is required. Such applications include online security assessments and contingency screening. The PEBS method was proposed by Kakimoto et al. [49] with its theoretical foundation provided in [8]. Among the direct methods, the concept of the controlling unstable equilibrium point (controlling UEP or CUEP) has been shown in [7], [50] to give more accurate estimates of stability than those computed by the classical concept of the closest UEP. Several other direct methods (not based on energy functions) for transient stability analysis are also present in the literature, i.e. the hyperplane method in [51], [52], the solutions to a special set of partial differential equations [53], [54], and the use of the normal form [55], [56]. Despite their differences in assessing stability, these direct methods share one common goal: to provide an accurate approximation of the stability boundary in the direction of the fault-on trajectory. The performance of each method, however, may vary considerably in several aspects such as computational speed, accuracy in approximating the stability boundary, conservativeness, robustness, etc. Unfortunately, any technical in-depth comparisons or evaluations of these available direct methods are still lacking in the literature.

This chapter provides a critical evaluation of four direct methods for approximating the relevant stability boundary and assessing transient stability in power systems: the PEBS method, the energy function-based CUEP method, the hyperplane method, and a method that employs the

solution set (via a quadratic approximation) of a special set of partial differential equations. The evaluation study consists of two parts. First, a graphical evaluation displays the accuracy of each method in approximating relevant stability boundaries while a second detailed evaluation compares the accuracy of each method in computing the estimated *critical clearing times* (CCTs) on two test systems, the WSCC 9-bus system and the IEEE 145-bus system. The evaluation is mainly focused on the accuracy and conservativeness in assessing stability where the time-domain approach is used as the benchmark. The mathematical concepts and backgrounds of transient stability analysis are provided in section 7.2. The concept of the controlling UEP theory is given in section 7.3. Section 7.4 describes the task of computing the controlling UEP and how it can be carried out effectively. All five methods for transient stability boundary approximations are explained in section 7.5. Sections 7.6 and 7.7 contain the simulation results and evaluation of all the methods. Conclusions are given in Section 7.8.

7.2 Preliminaries

7.2.1 Power system model

Consider a power system with n generators and loads interconnected by a transmission network. The dynamics of this power system can be represented by a set of nonlinear differential equations:

$$\dot{x} = f(x) \tag{7.1}$$

where $x \in R^{2n}$ are the state variables. The classical model is used and the loads are modeled as constant impedances. The dynamics of the i-th generator can be represented by the swing equations:

$$\begin{aligned} \dot{\delta}_i &= \omega_i \\ M_i\dot{\omega}_i &= P_{mi} - P_{ei}(\delta) - D_i\omega_i, \quad i = 1,...,n \end{aligned} \tag{7.2}$$

where D_i and M_i are the damping ratio and inertia constant of machine i. $P_{ei}(\delta) = E_i^2 G_{ii} + E_i(\sum_{k\neq i}^{n} E_k(G_{ik}\cos\delta_{ik} + B_{ik}\sin\delta_{ik}))$ is the electrical power at machine i, E_i is the constant voltage behind direct axis transient reactance, and P_{mi} is the mechanical power. $Y = (Y_{ij})_{n\times n} = (G_{ij} + jB_{ij})_{n\times n}$ is the reduced admittance matrix.

If the center of inertia for all machines is used as the reference (COI format) and uniform damping is assumed, then (7.2) can be transformed into the following system:

$$\begin{aligned} \dot{\tilde{\delta}}_i &= \tilde{\omega}_i \\ \dot{\tilde{\omega}}_i &= (P_{mi} - P_{ei}(\tilde{\delta}))/M_i - P_{COI}/M_T - d_0\omega_i \\ & \qquad\qquad i = 1,...,n \end{aligned} \tag{7.3}$$

where,

$$\tilde{\delta}_i = \delta_i - \delta_0 \qquad \delta_0 = (\sum_k^n M_k\delta_k)/M_T$$
$$\tilde{\omega}_i = \omega_i - \omega_0 \qquad \omega_0 = (\sum_k^n M_k\omega_k)/M_T$$
$$M_T = \sum_k^n M_k \qquad d_0 = D_i/M_i, i = 1,...,n$$
$$P_{COI} = \sum_k^n P_{mk} - \sum_k^n\sum_j^n (E_kE_jG_{kj}\cos\tilde{\delta}_{kj} - E_kE_jB_{kj}\sin\tilde{\delta}_{kj})$$

7.2.2 Stability region and stability boundary

Let us first consider a general nonlinear dynamical system described by (7.1). An equilibrium point is a solution to the equation $0 = f(x)$. A hyperbolic equilibrium point is an equilibrium point at which the Jacobian $J(x) = \partial f/\partial x$ has no eigenvalue with a zero real part.

A hyperbolic stable equilibrium point x_s of (7.1) is the point where all the eigenvalues of the Jacobian matrix have negative real parts. A type-k equilibrium point is a hyperbolic equilibrium point at which k eigenvalues of $J(x)$ have a positive real part. The flow or trajectory of the system (7.1) is the solution to (7.1) at time t starting at x, and it is denoted by $\phi(t, x)$. The stable manifold of a hyperbolic equilibrium point x_k is the set of all points from which the flow will converge to x_k as time approaches positive infinity. It can be mathematically expressed by:

$$W^s(x_k) = \{x : \phi(t, x) \to x_k, \quad \text{as } t \to +\infty\} \tag{7.4}$$

The *unstable manifold* of the hyperbolic equilibrium point x_k is the set of all points from which the flow will converge to x_k as time approaches negative infinity. It can be mathematically expressed by:

$$W^u(x_k) = \{x : \phi(t, x) \to x_k, \quad \text{as } t \to -\infty\} \tag{7.5}$$

The stability region of an asymptotically stable equilibrium point x_s is the stable manifold of x_s and can be expressed as:

$$A(x_s) = \{x : \phi(t, x) \to x_s, \quad \text{as } t \to +\infty\} \tag{7.6}$$

The following theorem from [9] characterizes the stability region of a dynamical system.

Theorem 7.2.1 Suppose the system (7.1) satisfies the following assumptions.

1) All the unstable equilibrium points on the stability boundary are hyperbolic.
2) The stable and unstable manifolds of the equilibrium points on the boundary satisfy the transversality condition.

3) Every trajectory on the stability boundary approaches one of the equilibrium points as $t \to +\infty$.

Then, the boundary of the stability region $A(x_s)$ of a hyperbolic stable equilibrium point x_s is composed of the stable manifolds of all unstable equilibrium points x_e on the boundary of the stability region.

$$\partial A(x_s) = \bigcup_{x_e \in \partial A} W^s(x_e) \tag{7.7}$$

7.2.3 Transient stability

Transient stability is the ability of a power system to maintain its machine angle synchronism following a large disturbance or *fault*. To analyze transient stability due to a fault, the system is considered to go through three stages. The first stage, the *pre-fault* stage, represents the period before a fault occurs. The system is assumed to be in steady state. The second stage, or the *fault-on* stage, is the short period of time where the power system is under stress right after the fault occurs. Once the fault is cleared by the protective relay system, the system enters the last stage, called the *post-fault* stage. If the system settles to a stable operating condition, then the system is said to be transiently stable following the fault. In fact, transient stability analysis can be considered as the study of the stability of the post-fault system.

Pre-Fault

In the pre-fault stage, the system is operating at a stable equilibrium point x_s^{pre}. The dynamics of this stage is described by

$$\dot{x} = F_1(x), \quad t < 0, \quad x \in R^{2n} \tag{7.8}$$

where $x_s^{pre} = x(0)$, and state variables are machine angles and angular speeds.

Fault-On

At $t = 0$, the system experiences a large disturbance and enters the fault-on stage whose dynamics are governed by

$$\dot{x} = F_2(x), \quad x(0) = x_s^{pre}, \quad 0 \le t < t_{cl} \tag{7.9}$$

where t_{cl} is the time when the protective system is activated. It should be noted that the fault-on stage can also be modeled as several sub-stages when multiple protective devices are activated at different times. In this paper, we only consider a single-stage fault-on period.

Post-Fault

When the fault is cleared, the power system enters the last stage whose dynamics are described by

$$\dot{x} = f(x), \quad t \ge t_{cl} \tag{7.10}$$

In this stage, the system is assumed to have a stable equilibrium point at x_s^{post}.

The fundamental issue of transient stability analysis is whether the system trajectory, starting at the post-fault initial state $x(t_{cl})$, will be able to settle down at x_s^{post}. This can be expressed by the concept of the stability region. The stability region (or the region of attraction $A(x_s^{post})$) of the post fault stable equilibrium point x_s^{post} is defined as the set of points from which the trajectories converge to x_s^{post}. The goal of transient stability analysis is to determine whether the initial point of the post-fault trajectory is located inside the stability region of the equilibrium point x_s^{post}. Therefore it can be mathematically expressed by checking the following condition

$$x(t_{cl}) \in A(x_s^{post}) \tag{7.11}$$

7.3 Controlling UEP

Let x_s^{pre} be a pre-fault stable equilibrium point (SEP), $x_f(t)$ be the corresponding fault-on trajectory and x_s^{post} be the post-fault SEP. Let $\partial A(x_s^{post})$ denote the stability boundary of the post-fault SEP x_s^{post}. A comprehensive theory of the characterization of the stability boundary of nonlinear systems has already been developed in [48] and [7]. The exit point plays a direct relationship between the fault-on trajectory and the post-fault system as it uniquely defines the controlling UEP.

Definition 7.3.1 (Exit-Point) Given a contingency on a power system stability model, the point at which the sustained fault-on trajectory intersects with the stability boundary of the post-fault SEP is called the *exit-point* of the fault-on trajectory (relative to the post-fault system). In addition, the fault-on trajectory exits the stability region after the exit point.

Definition 7.3.2 (Controlling UEP) The controlling UEP of a fault-on trajectory $x_f(t)$ is the UEP whose stable manifold contains the exit point of $x_f(t)$ (i.e. the controlling UEP is the first UEP whose stable manifold intersects with the fault-on trajectory $x_f(t)$ at the exit point).

Theorem 7.3.1 (Existence and Uniqueness of the controlling UEP) Given a pre-fault SEP, a fault-on system, and a post-fault system with an SEP x_s^{post}. Let the post-fault system admit an energy function $V(\cdot): R^{2n} \to R$ and let the stability region of x_s^{post} contain the pre-fault SEP. Then, the controlling UEP of the fault-on trajectory always exists and is unique.

Proof: The existence of the exit point of a fault-on trajectory is ensured as long as the energy function value increases along the fault-on trajectory. This proof is built on the following facts.

Fact 1) A sustained fault-on trajectory must exit the stability boundary of a post-fault system.

Fact 2) The exit point of the fault-on trajectory must lie on the stable manifold of a UEP on the stability boundary of the post-fault system.

Fact 1) is a consequence of the following two conditions: (i) the fundamental assumption of direct methods that the pre-fault SEP lies inside the stability region of the post-fault SEP and (ii) the energy value increases along a fault-on trajectory. Fact 2) is a consequence of the following fundamental theorem in [7]: the stability boundary is contained in the union of the stable manifolds of the UEPs on the boundary. Combining both facts, we complete the proof.

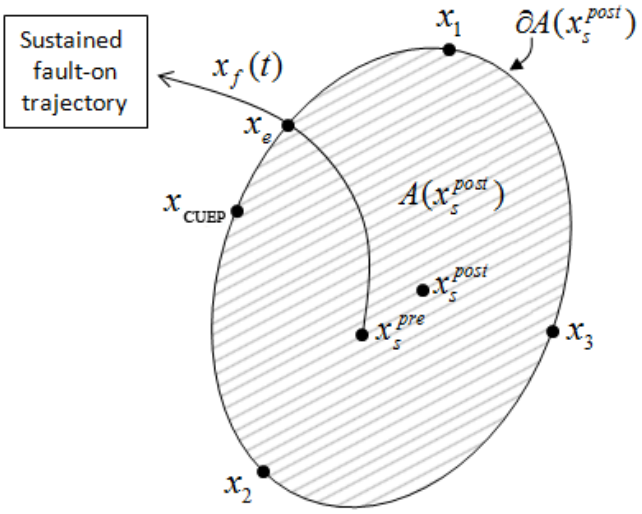

Figure 7.1 The sustained fault-on trajectory $x_f(t)$ moves toward the stability boundary $\partial A(x_s^{post})$ and intersects it at the exit point, x_e. The exit point lies on the stable manifold of the controlling UEP, x_{CUEP}

According to Theorem 7.2.1, the stable manifold of controlling UEP forms the relevant stability boundary toward which the fault-on trajectory moves. If the fault is cleared before the fault-on trajectory reaches the relevant stability boundary, then the post-fault system will be stable; otherwise, it will be unstable. Hence, the controlling UEP method for direct analysis of transient stability is composed of the following two tasks.

Task 1: Compute the controlling UEP relevant to the fault-on trajectory.

Task 2: Approximate the stable manifold of the controlling UEP by an appropriate method.

We discuss computational aspects of Task 1 in the next section and evaluate different numerical methods for Task 2 in the following section.

7.4 Computing Controlling UEP

The task of computing the (exact) controlling UEP of a given fault for general power system models is very challenging due to the following complexities:

1) The controlling UEP is a particular UEP embedded in a large-degree state-space.
2) The controlling UEP is the first UEP whose stable manifold is hit by the fault-on trajectory (at the exit point).
3) The task of computing the exit point is very involved; it usually requires a time-domain approach.

The task of computing the controlling UEP is complicated further by the size and the shape of its convergence region. It is known that, with respect to a selected numerical method, each equilibrium point has its own convergence region, i.e., the region from which the sequence generated by the numerical method starting from a point in the region will converge to the

equilibrium point. It has been observed and theoretically investigated by several researchers that, under the Newton method, the size of the convergence region of the UEP can be much smaller than that of the SEP. In addition, the convergence region of either an SEP or a UEP is a fractal. Unfortunately, finding an initial guess sufficiently close to the controlling UEP is a difficult task.

The above complexities also call into doubt the correctness of any attempt to directly compute the controlling UEP of a power system stability model. The only one method that can directly compute the controlling UEP of an (original) power system stability model is the time-domain approach. These complexities serve to explain why many methods proposed in the literature fail to compute the controlling UEP. It is because these methods attempt to directly compute the controlling UEP of the power system stability model, which is difficult if not impossible to compute without using the time-domain approach.

The ability to compute the controlling UEP is vital to direct stability analysis. It may prove fruitful to develop a tailored solution algorithm for finding the controlling UEP by exploiting special properties as well as some physical and mathematical insights of the underlying power system model. We will discuss such a systematic method, called the BCU method [13], along this line for finding the controlling UEP for power system models.

The fundamental ideas behind the BCU method can be explained as follows. Given a power system stability model (which admits an energy function), say the original model, the BCU method first explores the special properties of the underlying model with the aim of defining a reduced-state model such that certain static as well as dynamic relationships between the original model and the reduced-state model are met. The BCU method then finds the controlling UEP of the reduced-state model by exploring the special structure of the stability boundary and the energy function of the reduced-state model. Third, it relates the controlling

UEP of the reduced-state model to the controlling UEP of the original model. In summary, given a power system stability model, there exists a corresponding version of the BCU method. The BCU method does not compute the controlling UEP directly on the original model since, as pointed out, the task of computing the exit point of the original model, a key step to compute the controlling UEP, is very difficult and usually requires the time-domain approach.

A conceptual BCU method is summarized as follows.

Step 1: From the fault-on trajectory $x_f(t)$, detect the exit point at which the projected trajectory exits the stability boundary of the post-fault reduced-state model.

Step 2: Use the exit point, detected in Step 1, as the initial condition and integrate the post-fault reduced-state model to an equilibrium point. Let the solution be x_{CUEP}.

Step 3: The controlling UEP with respect to the fault-on trajectory of the original model is solved by using x_{CUEP}. The energy function at $V(x_{CUEP})$ is the critical energy for the fault-on trajectory $x_f(t)$

7.5 Methods for Approximating Stability Boundary

7.5.1 Time-domain approach

Following the dynamics of (7.10), the system is stable if $\phi(t, x(t_{cl})) \to x_s^{post}$ as $t \to +\infty$. Since the system can only be observed for a certain amount of time $t_{obs} > t_{cl}$, transient stability is assessed by checking $|x(t_{obs}) - x_s^{post}| \leq \varepsilon$ for some appropriate tolerance value, ε.

The exact stability boundary of a stability region via the time-domain approach can be obtained by checking every point in the neighborhood of a stable equilibrium point. This way of determining the stability region, however, is extremely inefficient and computationally

impossible for larger power systems. It is included in this paper only as a benchmark for the evaluation.

7.5.2 Potential energy boundary surface (PEBS) method

As described in [49] and [8], the approximated stability boundary by the PEBS method is obtained using the first local maximum of the potential energy along the fault-on trajectory. The following is the three-step procedure for finding the approximated boundary.

1) Locate the first local maximum of the potential energy x_{PEBS} along the fault-on trajectory.
2) Determine the critical energy using $V_c = V_p(x_{PEBS})$ where $V_p : R^{2n} \to R$ is the potential energy function described in [1].

Obtain the approximation of the stability boundary using all the points in the set $S = \{x \in R^{2n} : V(x) = V_c\}$ where $V : R^{2n} \to R$ is the total energy function described in [1].

7.5.3 Energy function-based CUEP method

The approximation of the stability boundary via the energy function-based CUEP method can be obtained by the following steps.

Step 1: Locate the controlling unstable equilibrium point x_{CUEP} on the stability boundary. Controlling unstable equilibrium points can be effectively computed by the BCU method proposed in [13].

Step 2: Determine the critical energy at the controlling unstable equilibrium point x_{CUEP}, $V_c = V(x_{CUEP})$ where $V : R^{2n} \to R$ is the total energy function described in [1].

Step 3: Obtain the approximation of the stability boundary by all the points in the set $S = \{x \in R^{2n} : V(x) = V_c\}$.

7.5.4 Hyperplane-based CUEP method

Let us consider the dynamical system (7.1). As described in [51], the approximation of the stability boundary in the vicinity of a type-1 unstable equilibrium point $x_e^1 = (\tilde{\delta}_e^1, \tilde{\omega}_e^1)$ can be described by the following equation.

$$g(\tilde{\delta}, \tilde{\omega}) = \alpha'(\tilde{\delta} - \tilde{\delta}_e^1) + \beta'(\tilde{\omega} - \tilde{\omega}_e^1) = 0 \tag{7.12}$$

where (α, β) is the eigenvector associated with the unstable eigenvalue μ.

$$J(x_e^1)\begin{bmatrix}\alpha \\ \beta\end{bmatrix} = \mu\begin{bmatrix}\alpha \\ \beta\end{bmatrix} \tag{7.13}$$

where $J(x) = \partial f / \partial x$ is the Jacobian of f.

In this paper, all non energy function-based methods are evaluated at the controlling UEP. The hyperplane method will therefore be referred to specifically as the *hyperplane-based CUEP method*.

7.5.5 Quadratic-based CUEP method

It is shown in [53] that the function describing the stable manifold of a type-1 unstable equilibrium point x_e^1 satisfies a specific set of partial differential equations.

$$W^s(x_e^1) = \left\{ \begin{matrix} x : h(x) = 0,\ \text{rank}(\partial h / \partial x) = 1 \\ \text{such that } [\partial h / \partial x] f = \mu h, \quad h(x_e^1) = 0 \end{matrix} \right\} \tag{7.14}$$

According to Theorem 7.2.1, the stability boundary near an unstable equilibrium point can therefore be characterized by the equations $h(x)=0$.

The implicit expression of $h(x)$ in (7.14) can be approximated and expressed explicitly by a power series expansion at an equilibrium point. Consider the dynamic system (7.1) and assume x_e^1 is a type-1 unstable equilibrium point with unstable eigenvalue μ. The series expansion at x_e^1 is as follows

$$f(x)=f(x_e^1)+J(x_e^1)(x-x_e^1)+\frac{1}{2}\begin{pmatrix}(x-x_e^1)H_1(x_e^1)(x-x_e^1)\\ \vdots \\ (x-x_e^1)H_n(x_e^1)(x-x_e^1)\end{pmatrix}+\cdots \tag{7.15}$$

where $J(x)=\partial f/\partial x$ is the Jacobian of f and $H_i(x)=\partial^2 f_i/\partial x^2$ is the Hessian matrix of f_i. Then a quadratic approximation of the stable manifold $h(x)$ at x_e^1 can be expressed as:

$$h_Q(x)=\eta^T(x-x_e^1)+(x-x_e^1)^T Q(x-x_e^1)/2 \tag{7.16}$$

The coefficients η and Q of the quadratic expression can be determined as follows.

1) The coefficient vector $\eta\in R^n$ of the linear term is the left eigenvector associated with eigenvalue μ of the Jacobian J at the equilibrium point x_e^1

$$J^T\eta=\mu\eta,\qquad \eta^T\eta=1 \tag{7.17}$$

2) The coefficient matrix Q of the quadratic term is the solution of the Lyapunov equation

$$CQ+QC^T=H \tag{7.18}$$

where $C=(\mu I/2-J^T)$, I is the $n\times n$ identical matrix, and $H=[\sum_{i=1}^n \eta_i H_i]$.

Since the final expression of the stability boundary is obtained by a quadratic approximation and the type-1 unstable equilibrium point used for the evaluation is a controlling UEP, we refer to this approach as the *quadratic-based CUEP method*.

7.6 Visualization of the Stability Regions of High-dimensional Power Systems

The ability to visualize stability regions can provide us with a better understanding of the dynamic behaviors and stability characteristics of the study system. With the visualization of stability regions, it becomes easier to observe system reactions to several factors such as changes in loading conditions, damping, etc. This task, however, can be very challenging for large systems. A technique for visualizing 2-D portraits of high-dimensional power systems while maintaining critical points of interest is proposed.

The following are steps for obtaining the 2-D portraits.

Step 1: Obtain three points of dynamic importance: a post-fault stable equilibrium point, the controlling UEP and an exit point. The post-fault SEP is computed by the Newton method, and the controlling UEP can be effectively computed using the BCU method. The actual exit point is very expensive to compute. We use the first local maximum of the potential energy value along the fault-on trajectory, starting at a pre-fault SEP, as an estimate of an actual exit point.

Step 2: Define the first intersection hyperplane from the three points found in 1) as shown in Figure 7.2.

Step 3: Obtain the stability boundary on this intersection plane. Since the computation only has to be done on the two dimensional plane, the computational burden is greatly reduced.

Step 4: Pick two observed machine angles such that the distances between the three points found in step 1) are maximized. This ensures that these points will be reasonably spaced in the final 2-D portrait.

Step 5: As shown in Figure 7.2, obtain the final 2-D portrait by projecting the results on the first intersection plane onto the final observed plane defined by the two chosen machines angles in step 4).

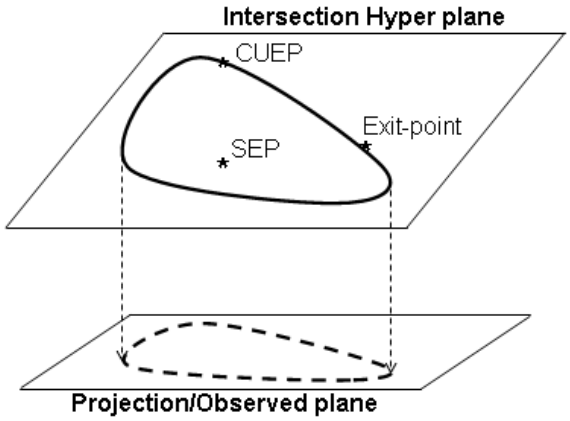

Figure 7.2 How to obtain an informative 2-D portrait of the stability regions of high-dimensional power systems.

7.7 Evaluation of Relevant Stability Boundary Approximations

We define the *relevant stability boundary* as the stable manifold of the controlling UEP intersected by the fault-on trajectory. It can also be viewed as the stability boundary in the neighborhood of the controlling UEP. The performance of each method in approximating the relevant stability boundary is illustrated by two test systems: the WSCC 9-bus system and the IEEE 145-bus system.

7.7.1 WSCC 9-bus system

The one-line diagram and dynamic data of the WSCC 9-bus system can be found in [2]. A uniform damping of 0.1 is applied to every machine while loads are maintained at the original values. Two contingencies are studied to illustrate the performance of each method in approximating the relevant stability boundary. The first contingency has bus no. 9 as the fault bus, and line 9-6 is tripped at the clearing time. The second contingency has bus no. 8 as the fault bus, and line 8-7 is tripped. All graphical results for this system are obtained on the $\omega = 0$ plane.

Figure 7.3 shows the approximated relevant stability boundaries of the first contingency by the hyperplane-based CUEP and the quadratic-based CUEP methods. The exact stability boundary, displayed by the solid black line, is obtained via the time-domain simulation and is

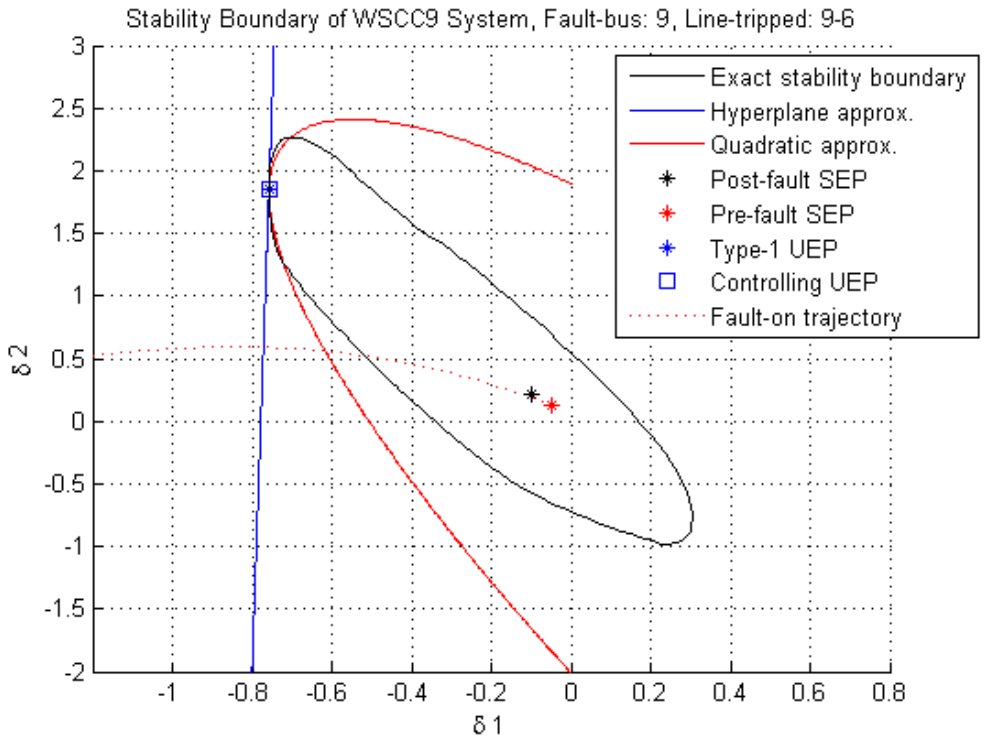

Figure 7.3 The exact stability boundary of the WSCC 9-bus system and the approximations by the hyperplane-based CUEP and the quadratic-based CUEP methods. The fault-bus is 9 and line 9-6 is tripped. Both methods give over-approximations of the relevant stability boundary.

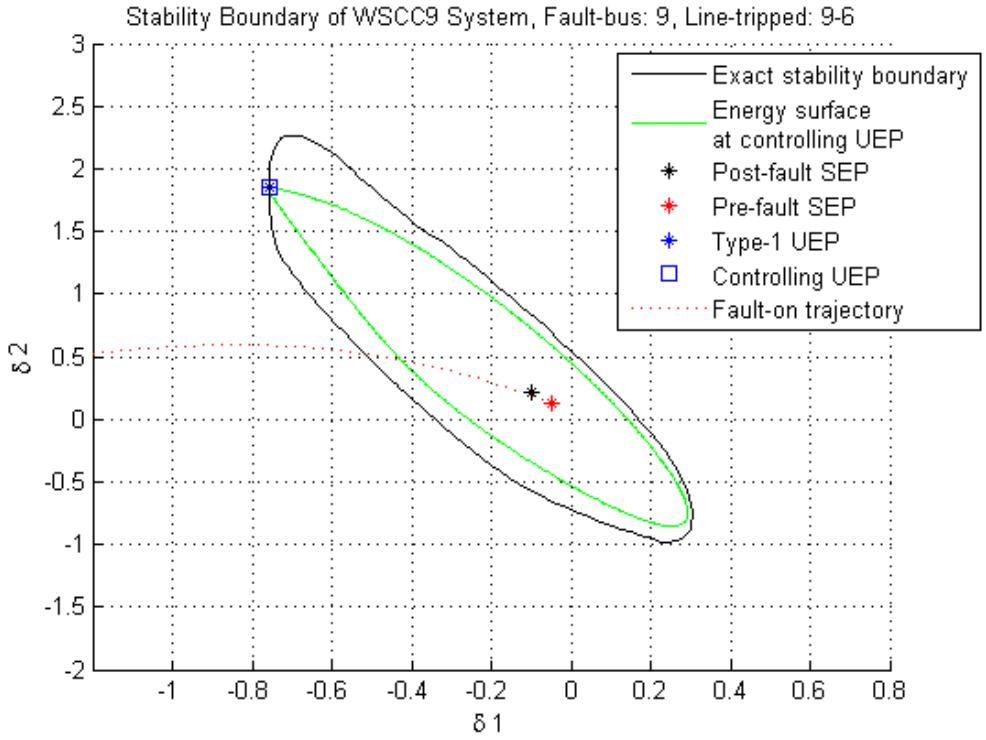

Figure 7.4 The exact stability boundary of the WSCC 9-bus system and the approximation by the energy function-based CUEP method. The fault-bus is 9 and line 9-6 is tripped. Because the controlling UEP is also a closest UEP in this case, this method gives a strictly conservative approximation of the entire stability boundary.

included as a benchmark. Since the hyperplane method employs only the first derivative information at the controlling UEP, the result is the straight blue line passing through the controlling UEP at (-0.7576, 1.858). The dotted red line is the projection of the actual fault-on trajectory onto $\omega = 0$ plane and is presented in the figure as a fault-on trajectory example. It can be seen that the fault-on trajectory hits the actual stability boundary long before it reaches the boundary approximated by the hyperplane method. This large approximation error by the hyperplane method is caused by two major factors: first is the extreme non-linear characteristic of the actual stability boundary near the controlling UEP, and second is the large distance between the controlling UEP and the point where the fault-on trajectory hits the actual stability boundary. The quadratic method tries to alleviate the non-linear characteristic issue by taking

into account the second derivative at the controlling UEP. The result of this approach is shown by the solid red line passing through the controlling UEP, and it appears to capture the characteristics of the stability boundary around the controlling UEP much more accurately than the hyperplane method. Despite the better results, the quadratic approximation can be subject to large approximation errors if the fault-on trajectory moves in a direction considerably far from the controlling UEP. Both the hyperplane and quadratic methods give an over-approximation (in the direction of fault-on trajectory) in this case.

The performance of the energy function-based direct methods is displayed in Figure 7.4-7.5. The green line in Figure 7.4 represents the relevant stability boundary approximated by the energy surface passing through the controlling UEP (energy function-based CUEP method), and

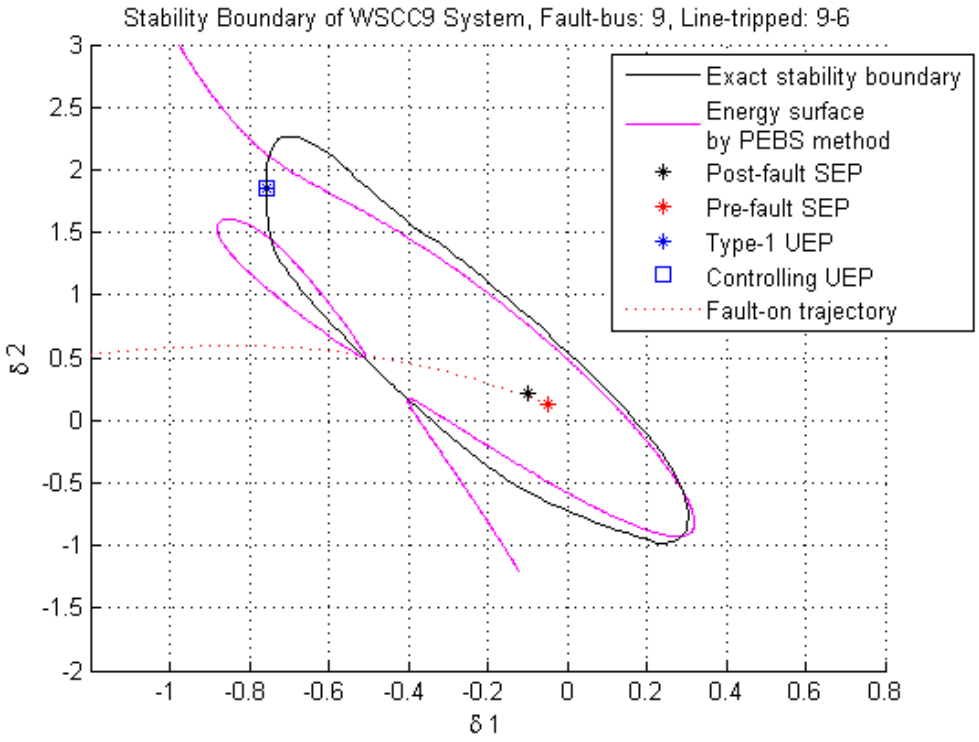

Figure 7.5 The exact stability boundary of the WSCC 9-bus system and the approximation by the PEBS method. The fault-bus is 9 and line 9-6 is tripped. The PEBS method gives a good approximation in the direction of the fault-on trajectory, but it produces a poor overall result for the relevant stability boundary.

the magenta line in Figure 7.5 is the boundary approximated by the PEBS method. In this example, the controlling UEP is also the closest UEP. Hence the green boundary appears to be strictly conservative in any direction from the SEP. The PEBS method is the only direct method that does not require a UEP to obtain a boundary approximation. It employs the first local maximum of the potential energy along the fault-on trajectory to determine the critical energy value. As a result, the boundary approximated by the PEBS method is the only one that does not pass through the controlling UEP. The approximation of the relevant stability boundary by the PEBS method is good only in the direction of the fault-on trajectory. The result in other directions can be very poor or nonexistent.

The results of the second contingency (where bus no. 8 is the fault-bus and line 8-7 is tripped) are shown in Figure 7.6-7.8. In Figure 7.6, it can be seen that both non-energy-function-based methods give much better approximations of the actual stability boundary than in the first contingency. Even though the point where the fault-on trajectory hits the actual stability boundary is farther from the SEP than in the first example, the linear characteristic of the stability boundary in the neighborhood of the controlling UEP helps make the approximations by both methods satisfactorily accurate. In the direction of the fault-on trajectory, the hyperplane method still gives an overestimate while the quadratic gives a slight underestimate in this case. In Figure 7.7, the approximated boundary by the energy function-based CUEP method shows that the controlling UEP at (-0.3765, 0.012) is not the same point as the closest UEP at (-0.561, 2.309). The approximation by the energy function-based CUEP method is conservative in the direction of the fault-on trajectory. The relevant boundary approximation by the PEBS method in Figure 7.8 is only available in the direction of the fault-on trajectory, and the result in this case is a slight overestimate.

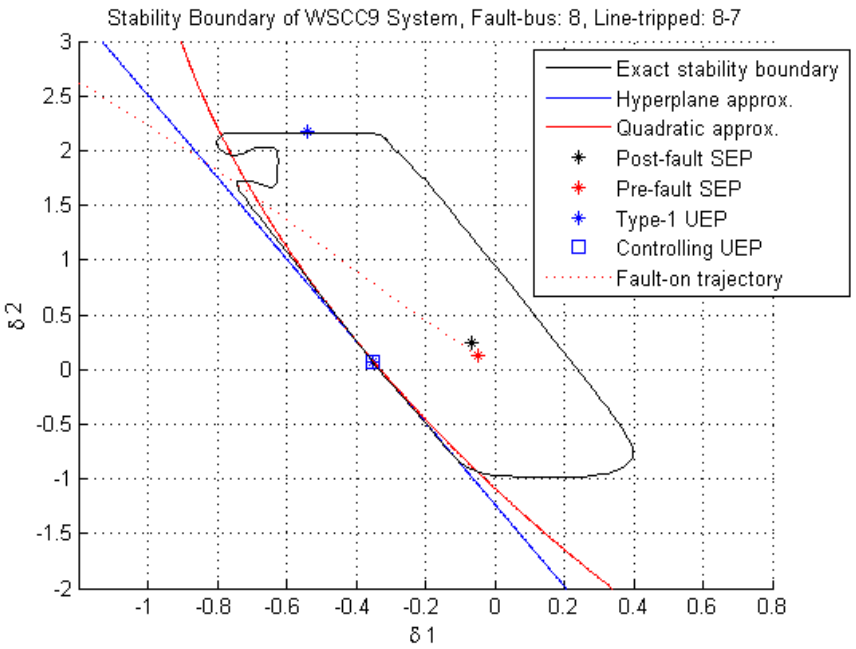

Figure 7.6 The exact stability boundary of the WSCC 9-bus system and the approximations by the hyperplane-based CUEP and the quadratic-based CUEP methods. The fault-bus is 8 and line 8-7 is tripped.

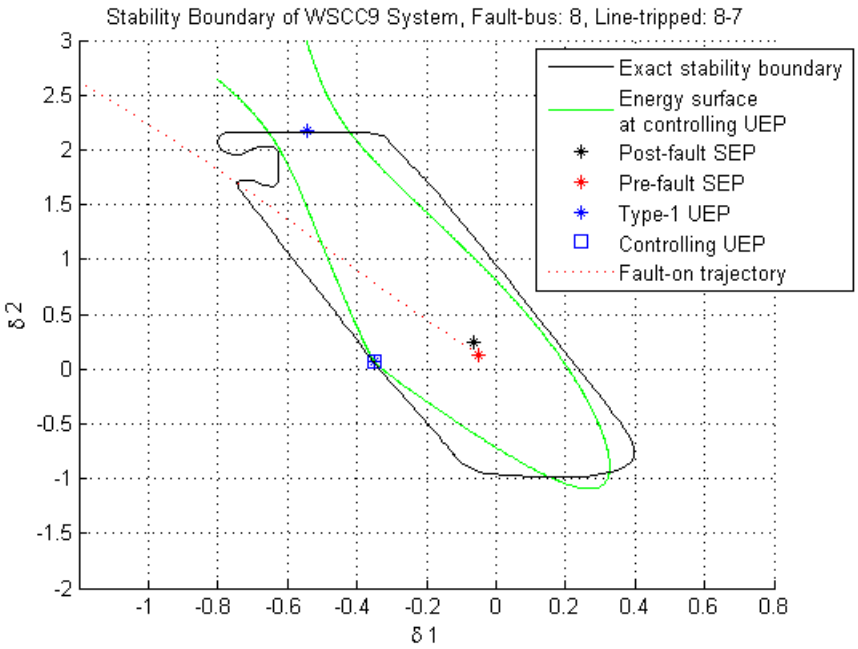

Figure 7.7 The exact stability boundary of the WSCC 9-bus system and the approximation by the energy function-based CUEP method. The fault-bus is 8, and line 8-7 is tripped. This method gives a conservative approximation in the neighborhood of the controlling UEP (relevant stability boundary).

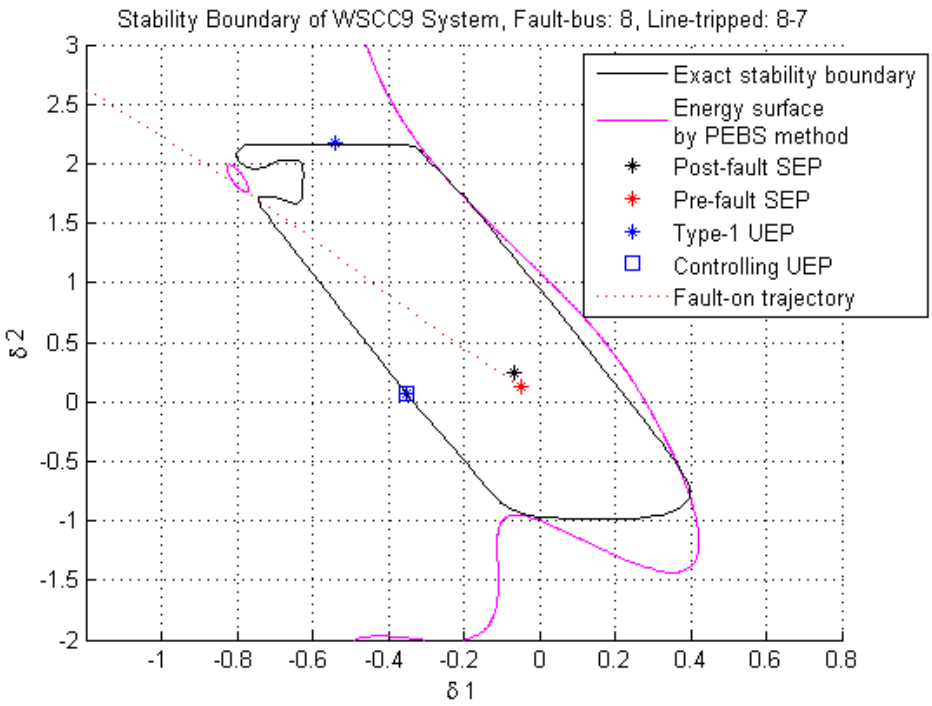

Figure 7.8 The exact stability boundary and the approximation of stability boundary of WSCC 9-bus system by the PEBS method. The fault-bus is 8, and line 8-7 is tripped. The approximation of the relevant stability boundary by the PEBS method is acceptable in the direction of the fault-on trajectory, but it is very bad in the neighborhood of the controlling UEP.

7.7.2 IEEE 145-bus system

By utilizing the visualization technique proposed in section 7.6, the performance of each method can be graphically evaluated for the larger system of IEEE 145 buses [1]. A uniform damping of 1.0 is applied to every machine and the loads are at the original values. One contingency (59 as the fault-bus, and 59-72 as the fault-line) is presented. The stability boundary approximated by the hyperplane-based CUEP and quadratic-based CUEP methods are displayed in Figure 7.9. The results by the energy function-based CUEP and the PEBS method are shown in Figure 7.10 and Figure 7.11. The chosen angle coordinates are machine 3 at bus 79 and machine 6 at bus 89. In this case, the characteristic of the stability boundary near the controlling

UEP is somewhat linear and results in good approximations by the hyperplane and quadratic methods, see Figure 7.9. Both methods, however, give slight overestimations in the direction of the fault-on trajectory. In Figure 7.10, the boundary approximated by the energy function-based CUEP method is contained within the actual stability region yielding a conservative boundary approximation. In Figure 7.11, the result by the PEBS method in the fault-on direction also gives a conservative approximation and is less conservative than that given by the energy function-based CUEP method. Similar to the WSCC 9-bus cases, the approximation of the relevant stability boundary by the PEBS method is very poor in the neighborhood of the controlling UEP.

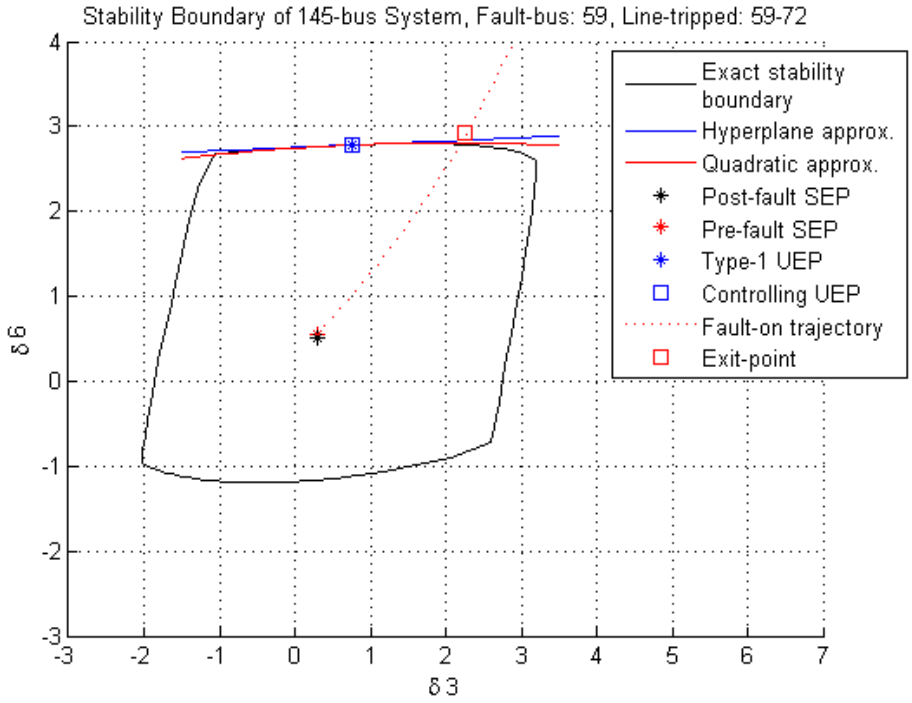

Figure 7.9 A 2-D portrait of the exact stability boundary of the IEEE 145-bus system and approximations by the hyperplane-based CUEP and the quadratic-based CUEP methods. The fault-bus is 59 and line 59-72 is tripped. Both methods give over-approximations of the relevant stability boundary.

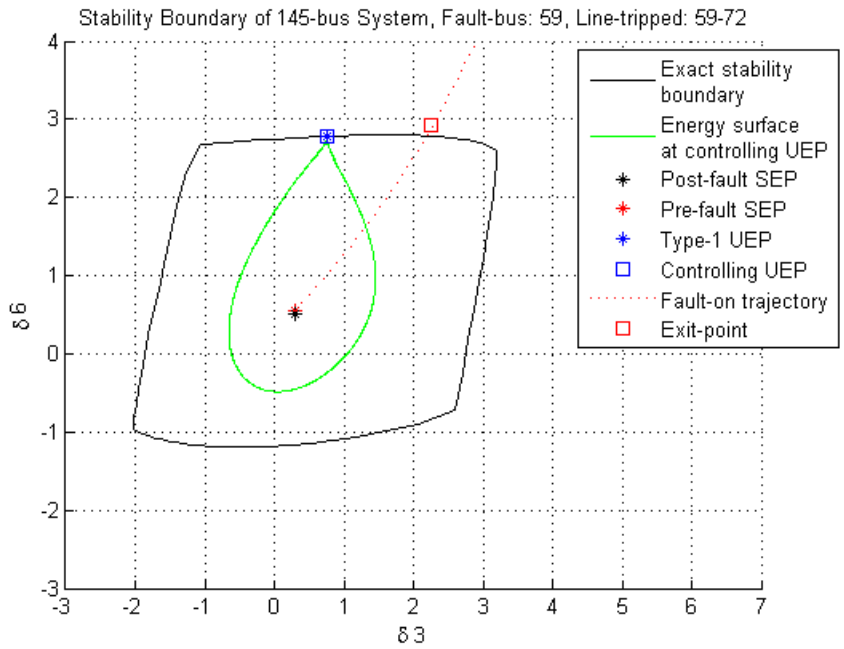

Figure 7.10 A 2-D portrait of the exact stability boundary of the IEEE 145-bus system and approximation by the energy function-based CUEP method. The fault-bus is 59, and line 59-72 is tripped. Even in the larger case, this method gives a strictly conservative approximation of the relevant stability boundary.

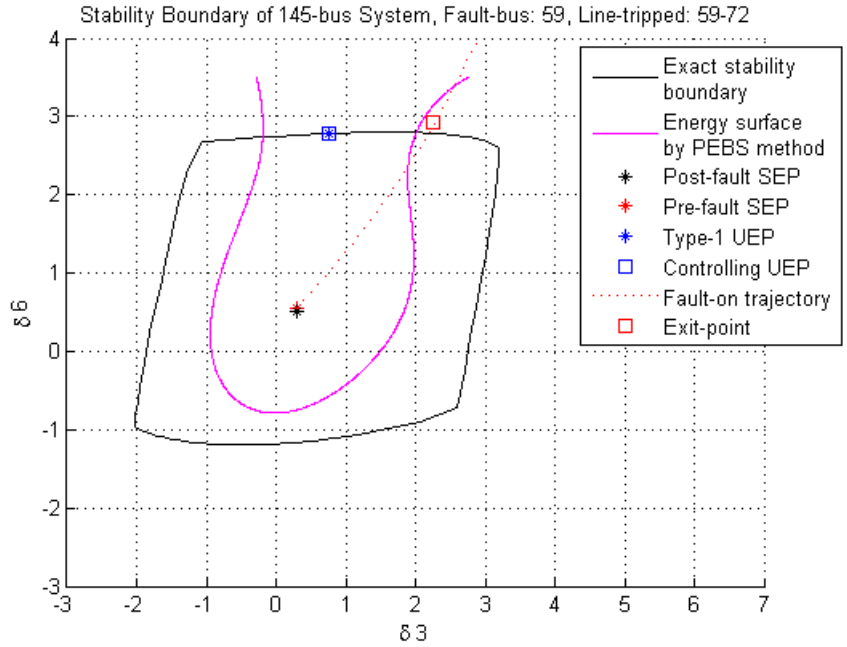

Figure 7.11 A 2-D portrait of the exact stability boundary of the IEEE 145-bus system and approximation by the PEBS method. The fault-bus is 59 and line 59-72 is tripped. The PEBS method gives a good approximation in the direction of fault-on trajectory but a poor result in the neighborhood of the controlling UEP.

The numerical studies of the relevant stability boundary approximations by all four direct methods give us the following observations.

- The energy function-based CUEP method always gives conservative approximations of the relevant stability boundary.
- The quadratic-based CUEP method gives a relatively accurate approximation of the relevant boundary but does not guarantee conservativeness.
- The hyperplane-based CUEP method always gives over-approximations of the relevant stability boundary. This may imply the convex-set characteristic of the stability region in the vicinity of the controlling UEP.
- The PEBS method can only provide a good approximation in the direction of the fault-on trajectory. However, the approximation of the relevant stability by this method is mostly very poor in the neighborhood of the controlling UEP.

7.8 Evaluation of CCT Computations

The accuracy of each direct method in computing estimated critical clearing times (CCTs) is evaluated. The time-domain approach is used as a benchmark. Ten different contingencies and five loading conditions are considered on both WSCC 9-bus and IEEE 145-bus systems. Moreover, we also investigate whether each method can give conservative estimates of the CCTs. Conservative assessment is a crucial property for fast contingency screening, where only safe contingencies can be screened out.

7.8.1 WSCC 9-bus system

For the WSCC 9-bus system, the CCTs are computed by each method for ten different contingencies as shown in Table 7.1. The average relative errors and conservativeness percentages are also included. The CCTs from the time-domain approach are considered as the benchmark. The performance of each method can be affected by several factors such as increases in loads, changes in damping values, etc. In this thesis, we present the performance of each method under variable loading conditions. In Table 7.2, the results of four loading conditions (at 90%, 125%, 150% and 200%) are presented. The data was cultivated from the same ten different contingencies as shown in Table 7.1. The increase of loads applied to the system is done such that all the original power factors are preserved.

In Table 7.1, the average relative error by the PEBS method, 2.3883%, is the smallest at followed by that of the quadratic-based CUEP method, 3.1306%. The hyperplane-based CUEP method has the highest average error of 8.6550% while the energy function-based CUEP method is marginally better at 7.0894%. Regarding the conservative assessment percentage, the energy function-based CUEP method is 100%, the quadratic method is 70%, the PEBS method is 50% and the hyperplane method is 0%. In Table 7.2, we observe that relative errors of every method rise as loads increase. The quadratic method performs much worse under stressed conditions, showing the highest relative error of 40.6959% at 200% of the loading condition. Its conservativeness percentage also decreases as loads increase. The hyperplane method has a high average relative error of 30.3171% at 200% loading, and it has a 0% conservative assessment percentage for all loading conditions. The energy function-based CUEP method, not only being the least affected in average error, produces 100% conservative estimates at all loading conditions. Its average relative error at 200% loading is the smallest among the four direct

methods at 9.2614%. The PEBS method has the lowest average relative error at smaller loading conditions but at 200% loading, the error becomes larger than that of the energy function-based CUEP method at 9.4005%.

Table 7.1: CCT estimates of the WSCC 9-bus system

Methods	Time-domain	PEBS	Energy- function CUEP	Hyperplane CUEP	Quadratic CUEP
Fault #1	0.5809	0.5799	0.5802	> 0.5907	0.5732
Fault #2	0.2611	> 0.2864	0.2604	> 0.2967	0.2560
Fault #3	0.2736	> 0.2878	0.2429	> 0.2951	> 0.2835
Fault #4	0.4178	> 0.4288	0.3415	> 0.4735	0.4083
Fault #5	0.4117	0.4099	0.4112	> 0.4198	> 0.4155
Fault #6	0.7436	0.7422	0.7433	> 0.7453	0.7426
Fault #7	0.6797	0.6763	0.6752	> 0.6830	0.6785
Fault #8	0.2430	0.2391	0.2276	> 0.3237	> 0.2749
Fault #9	0.4210	> 0.4293	0.3003	> 0.4650	0.3892
Fault #10	0.2273	> 0.2307	0.2155	> 0.2357	0.2268
Average relative error %	-	2.3883%	7.0894%	8.6550%	3.1306%
Conservativeness %	-	50%	100%	0%	70%

* The sign > at the CCT estimates indicates an over-approximation.

Fault #1 - Fault bus: 5, Line-tripped: 7-5, Fault #2 - Fault bus: 7, Line-tripped: 7-5, Fault #3 - Fault bus: 7, Line-tripped: 8-7, Fault #4 - Fault bus: 8, Line-tripped: 8-7, Fault #5 - Fault bus: 4, Line-tripped: 4-6, Fault #6 - Fault bus: 6, Line-tripped: 4-6, Fault #7 - Fault bus: 6, Line-tripped: 6-9, Fault #8 - Fault bus: 9, Line-tripped: 6-9, Fault #9 - Fault bus: 8, Line-tripped: 9-8, Fault #10 - Fault bus: 9, Line-tripped: 9-8.

Table 7.2: CCT estimates (9-bus) at different loading conditions

Methods	Time-domain	PEBS	Energy-function CUEP	Hyperplane CUEP	Quadratic CUEP
	10% Decrease				
Average relative error %	-	2.1562%	8.0148%	8.4234%	2.9772%
Conservativeness %	-	60%	100%	0%	50%
	25% Increase				
Average relative error%	-	2.9298%	7.5058%	9.5224%	6.3272%
Conservativeness %	-	60%	100%	0%	60%
	50% Increase				
Average relative error %	-	3.7712	8.3190%	11.9172%	13.0768%
Conservativeness %	-	50%	100%	0%	60%
	100% Increase				
Average relative error %	-	9.4005%	9.2614%	30.3171%	40.6959%
Conservativeness %	-	40%	100%	0%	30%

% increase is applied to all loads in the system in such a way that the original power factors are all preserved.

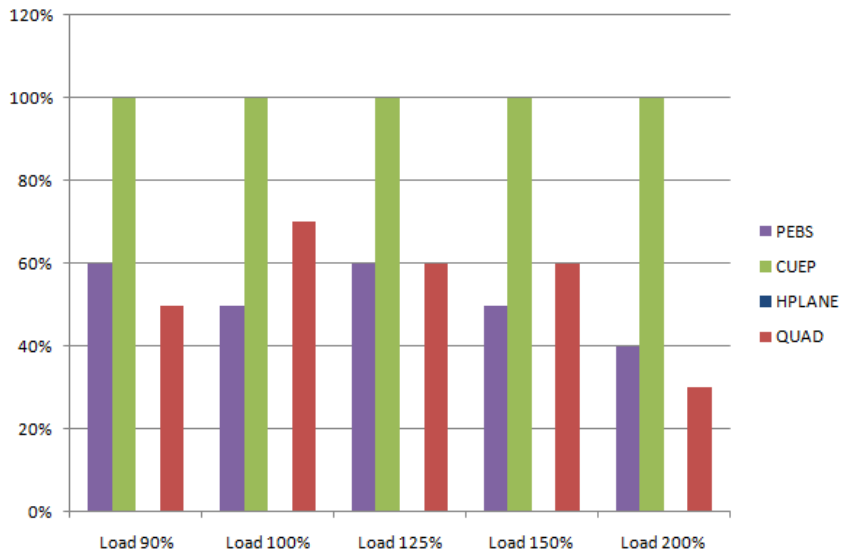

Figure 7.12: Conservative assessment percentages of 10 different contingencies of the WSCC 9-bus system

7.8.2 IEEE 145-bus system

The simulation results for the IEEE 145-bus system are presented in the same format as in the 9-bus system. Table 7.3 contains the CCTs data of ten contingencies at the base loading condition while Table 7.4 contains the average relative errors and conservativeness percentages at four different loading conditions.

Table 7.3 shows that the energy function-based CUEP method produces the smallest error of 17.2108% when compared to 20.6718%, 25.6618% and 27.9817% of the other three approaches. The energy function-based CUEP method still maintains a 100% conservative assessment percentage. Similar to the results in WSCC 9-bus system, the hyperplane method always overestimates the CCTs and hence shows 0% in its conservative assessment percentage.

Compared to the WSCC9 system, the accuracy of the PEBS method, hyperplane method and quadratic method is greatly reduced in this larger system as the average errors increase from

2.3883% to 20.6718% for the PEBS method, 8.6550% to 25.6618% for the hyperplane method and 3.1306% to 27.9817% for the quadratic method.

In Table 7.4, percentage errors at three loading conditions are presented. Since the 145-bus system is already stressed at the original loading condition, only small changes (up to 10% increase) in loads can be applied. When loads are slightly increased, the average relative error percentages of all three approaches also increase. The small increases in loading do not greatly affect the conservative assessment percentage on any approach. The energy function-based UEP method maintains its 100% conservative assessment percentage in all of the four loading conditions and gives the most accurate estimations at higher loading conditions. The hyperplane approach, same as in the WSCC 9-bus system, always overestimates CCTs in the 145-bus case.

Table 7.3: CCT estimates of the IEEE 145-bus System

Methods	Time-domain	PEBS	Energy-function CUEP	Hyperplane CUEP	Quadratic CUEP
Fault #1	0.1610	0.0981	0.1235	> 0.1860	> 0.2744
Fault #2	0.2009	0.1262	0.0985	> 0.2498	> 0.4780
Fault #3	0.2591	0.2212	0.1420	> 0.2881	> 0.2707
Fault #4	0.2699	0.1834	0.2307	> 0.5035	0.1863
Fault #5	0.3169	0.3111	0.3129	> 0.3195	> 0.3189
Fault #6	0.2998	0.2832	0.2840	> 0.3043	> 0.3032
Fault #7	0.2698	0.1832	0.2307	> 0.5034	0.1860
Fault #8	0.2850	0.2684	0.2619	> 0.2935	> 0.2871
Fault #9	1.0439	0.6674	1.0023	> 1.2981	> 1.0589
Fault #10	0.2095	0.2044	0.1990	> 0.2153	> 0.2116
Average relative error %	-	20.6718%	17.2108%	25.6618%	27.9817%
Conservativeness %	-	100%	100%	0%	20%

* The sign > at the CCT estimates indicates an over-approximation.

Fault #1 - Fault bus: 7, Line-tripped: 7-6, Fault #2 - Fault bus: 6, Line-tripped: 7-6, Fault #3 - Fault bus: 59, Line-tripped: 59-72, Fault #4 - Fault bus: 72, Line-tripped: 59-72, Fault #5 - Fault bus: 115, Line-tripped: 115-116, Fault #6 - Fault bus: 116, Line-tripped: 115-116, Fault #7 - Fault bus: 72, Line-tripped: 100-72, Fault #8 - Fault bus: 100, Line-tripped: 100-72, Fault #9 - Fault bus: 75, Line-tripped: 91-75, Fault #10 - Fault bus: 91, Line-tripped: 91-75.

Table 7.4: CCT estimates (145-bus) at different loading conditions

Methods	Time-domain	PEBS	Energy-function CUEP	Hyperplane CUEP	Quadratic CUEP
	10% Decrease				
Average relative error %	-	18.3362%	16.9460%	23.6817%	25.1587%
Conservativeness %	-	90%	100%	10%	30%
	2% Increase				
Average relative error %	-	21.4668%	18.9319%	27.7587%	29.1791%
Conservativeness %	-	90%	100%	0%	20%
	5%Increase				
Average relative error %	-	25.9607%	22.4051%	35.8428%	33.3557%
Conservativeness %	-	80%	100%	0%	20%
	10% Increase				
Average relative error %	-	30.1464%	25.0647%	48.9923%	39.9396%
Conservativeness %	-	80%	100%	0%	20%

% increase (or % decrease) is applied to all loads in the system in such a way that the original power factors are all preserved.

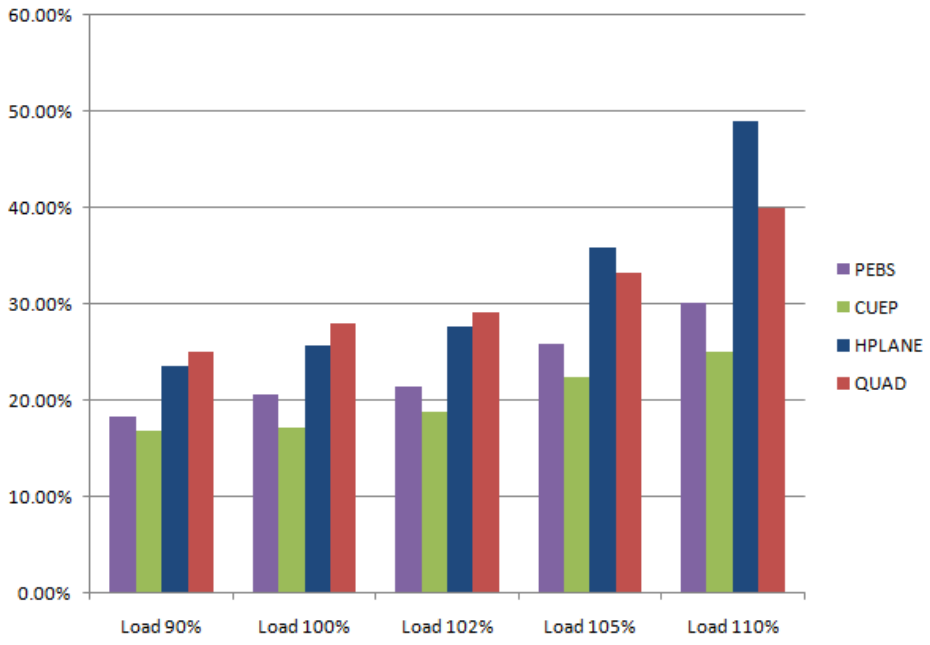

Figure 7.13: Average relative error percentages of 10 different contingencies of the IEEE 145-

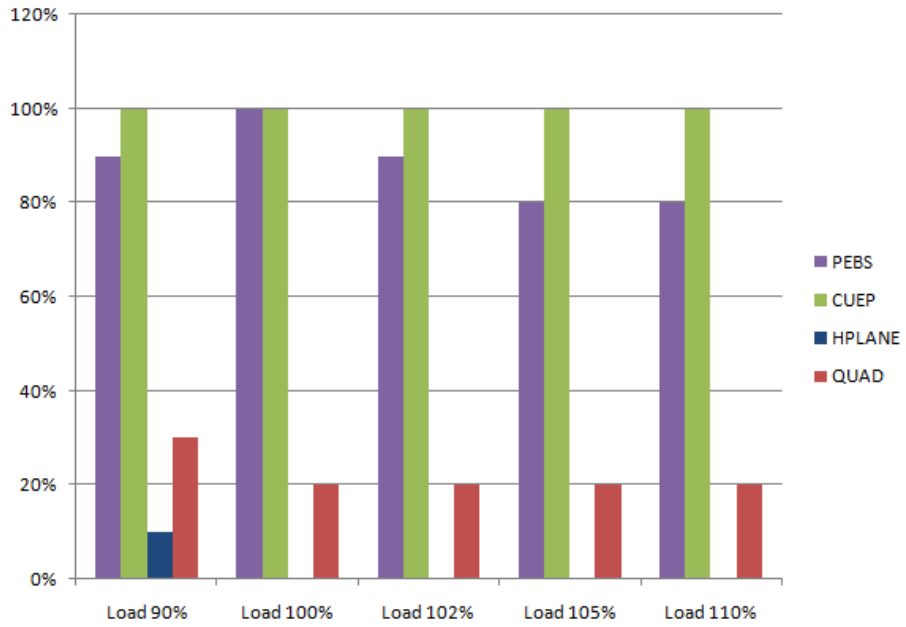

Figure 7.14: Conservative assessment percentages of 10 different contingencies of the IEEE 145-bus system.

The evaluation of CCT computations by all four direct methods provides the following observations.

- The energy function-based CUEP method is the most accurate method in estimating CCTs on the larger IEEE 145-bus system at all loading conditions except at 90% loading.
- The energy function-based CUEP method is the only method that guarantees conservative estimations of CCTs in both systems and all loading conditions.
- The accuracy in estimating CCTs by the energy function-based CUEP method is the least affected by load increases when compared to other methods.
- Although the PEBS method is very accurate in estimating CCTs on the smaller 9-bus system, the results are not as good as the energy function-based CUEP method at highest loading, at 200%, and in most conditions of the larger 145-bus system.
- An increase in loading conditions (original power factors are preserved) leads to higher

error percentages in estimating CCTs by all methods.

- The hyperplane-based CUEP method gives overestimated CCTs in almost every case regardless of the systems, contingencies or loading conditions. This may imply the convex-set characteristic of the stability region in the vicinity of the controlling UEP.
- Among all four direct methods, the PEBS method and the energy function-based CUEP method require the least computational effort in computing estimated CCTs. Only a computation of the energy function is needed for the two methods. The time-domain approach, the benchmark, is very slow since a large amount of numerical integrations are required in order to get the exact CCTs.

7.9 Conclusions

A critical evaluation of four direct methods for transient stability analysis is given in this paper: the energy function-based CUEP method, the PEBS method, the hyperplane-based CUEP method, and the quadratic-based CUEP method. A technique to visualize stability regions of high-dimensional power systems is also presented, showing that it is possible to obtain a simple yet informative 2-D portrait of the stability region of larger power systems. Using the proposed visualization technique, we provide a graphical evaluation of the performance of each direct method in approximating the relevant transient stability boundary of a large 145-bus power system. The CCT computation evaluation gives us more insight regarding the conservative assessment capability, and the accuracy of each direct method in estimating CCTs. The impact of load increases on the performance is also considered.

A comparison of the simulation results with the time-domain approach reveals several interesting observations regarding the performances of the four direct methods as follows:

- The energy function-based CUEP method always gives conservative approximations of the relevant stability boundary in both test systems.
- The energy function-based CUEP method is the most accurate method in estimating CCTs on the larger IEEE 145-bus system at most loading conditions.
- The energy function-based CUEP method is the only method that guarantees conservative estimations of CCTs in both systems and all loading conditions.
- The accuracy in estimating CCTs by the energy function-based CUEP method is the least affected by load increases when compared to other direct methods.
- It is computationally cheaper to approximate the relevant stability boundary or compute estimated CCT using the energy function-based direct methods (the energy function-based CUEP and the PEBS methods).

From these numerical results and the theoretical foundation of the controlling UEP method, it can be concluded that the energy function-based controlling UEP method excels in the following regard: the accuracy in estimating CCTs on a larger power system, the ability to provide conservative assessments, error sensitivity to higher loading conditions, and computational burden.

CHAPTER 8
Conclusion and Future Work

This chapter concludes and highlights the major contributions of this thesis. It also discusses future research directions for the BCU-based methods.

8.1 Conclusions

This thesis expands the applicability of the CUEP method to a wider range of power system applications and models, by providing numerical illustrations, conducting critical evaluations, and developing new solution methods. The first key result is the successful application of stability region theories and the concept of the CUEP method to the area of transient stability enhancement controls and TSCOPF in power systems. As a result of this work, two novel BCU-based methods were developed. The second key result is the extension and implementation of the CUEP methodology to incorporate more comprehensive power system models.

In Chapter 2, we explored the relationship between the stability regions of DAE system and the corresponding singularly perturbed system. We also numerically illustrated a method for computing the CUEP based on a projected fault-on trajectory, and demonstrated that the CUEP calculated in this form equals the CUEP calculated via the uniform CUEP of the singularly perturbed system. It is expected that the network-preserving CUEP method will play a vital role in the development of the CUEP method for power systems with more comprehensive models, including those that contain dynamic loads or renewable energy devices.

A practical extension of the BCU (CUEP) method for power systems with induction motors was developed and implemented in Chapter 3. We constructed numerical energy functions for power system models with induction motors based on the first integral principle, and then employed it to develop a corresponding BCU method with dynamic load capability. The numerical results on the adapted WSCC9 systems demonstrated the successful computations of the CUEPs which consequently, led to conservative direct assessments of transient stability.

In Chapter 4, a CUEP-based enhancement control scheme for large-scale power systems was developed and tested. Based on a stability-region framework, we gave the definition and characterizations of critical machines in power systems, and then proposed a new method for fast identifications of these machines. Instead of relying on time-domain-based observations or heuristic criteria like other existing methods, the proposed method accurately computes the critical machines by utilizing the unstable eigenvector at the CUEP to predict the post-fault system dynamics near the relevant stability boundary without having to perform numerical integrations. The numerical test results from applying the proposed method to our test systems revealed (i) good accuracy regarding the identification and rankings of critical machines, (ii) fast computational speed, and (iii) significant improvement in system transient stability.

In Chapter 5, a numerical critical evaluation of the fixed-threshold proxi for transient stability constraints in TSCOPF was conducted. By employing the proposed method for computing exact threshold values in power systems, we have shown that the exact threshold values are not constant, as assumed in the literature, and can vary from 80 to 190 degrees depending on several factors such as types of contingency, loading conditions, and network topology. We also demonstrated that if the threshold value in the proxi is chosen without the actual knowledge of system dynamics, it may lead to severe underestimate assessments,

overestimate assessments, and unnecessary degradations of the optimal solutions. These results led to the proposal of the novel BCU-based TSCOPF method in Chapter 6.

A BCU-based method is proposed in Chapter 6 to compute the solution of TSCOPF problems. What distinguishes this method from other existing TSCOPF methods is the ability to determine actual non-constant system threshold values, and more importantly the capability to handle large contingency lists. The first feature was achieved through the development of a BCU-based approach that can compute actual system thresholds, whereas the integration of the BCU method into our proposed method as a fast screening tool offers the second feature. The proposed method has been applied to several TSCOPF problems and the numerical results indicated that our proposed BCU-based method offers the advantages of (i) ensuring the accurate treatment of transient stability constraints, (ii) improving the overall computational speed, (iii) extending the capability of a TSCOPF method to handle large contingency lists, and (iv) achieving better quality optimal solutions.

In Chapter 7, a critical evaluation of four direct methods for transient stability analysis was conducted. The four direct methods include the energy function-based CUEP method, the PEBS method, the hyperplane-based CUEP method, and the quadratic-based CUEP method. We proposed a numerical technique to visualize the stability regions of high-dimensional power systems that is capable of providing fast visualizations of informative 2-D portrait of the stability region of larger power systems. The evaluation results revealed several interesting insights and showed that the energy function-based controlling UEP method excels other direct methods in (i) the accuracy in estimating CCTs of larger power systems, (ii) the accuracy in approximating relevant stability boundaries, (iii) the ability to provide conservative assessments, (iv) error sensitivity to higher loading conditions, (v) and computational burden.

8.2 Future Work

Our future research directions for the CUEP methodology include (i) the performance enhancement of the proposed BCU-based TSCOPF method and enhancement control scheme, (ii) the extension of both methods to incorporate detailed power system models, and (iii) the development of the theoretical work for the proposed methods.

In power system transient stability analysis, there are several special properties that can be exploited, such as the concept of critical machines presented in Chapter 4 or the concept of a group of coherent contingencies (group properties) which was recently introduced and characterized in [6]. The group properties in power system has proven useful in the development of a family of group-based BCU methods for accurate critical energy computations and for exact CUEP calculation [6]. Group properties can also be applied to other practical applications, such as group-based enhancement control schemes. As a result, the CUEP-based enhancement control scheme we proposed in Chapter 4 may be further enhanced by considering the group properties in its upgraded version. The consideration of group properties should greatly reduce the computation time during the contingency screening process. This computational advantage might be present during the derivation and application of the control schemes as well, i.e. one control action that enhances the transient stability of multiple contingencies that belong in the same group.

The BCU-based TSCOPF method proposed in Chapter 6 may be upgraded in the same manner except that it could also benefit from the concept of critical machines that we presented in Chapter 4. The main shortcoming of the discretization-based TSCOPF methods is the high computational burden due to the large number of constraints and variables considered in the formulation. By properly integrating the concept of critical machines in the solution method, we

may be able to reduce the number of constraints by enforcing the rotor angle limits only on critical machines, and omitting the rest. Since the rotor angles of non-critical (safe) machines should never separate first, their associated inequality limits stay non-binding throughout the calculation. Therefore they may be safely omitted to reduce the overall computation. Based on this conjecture, we conducted a study on the number of TSCOPF constraints using classical model, 5 seconds of integration time, 0.1 second step-size, and 1 critical machine. The results in Table 8.1 show that the number of constraints can be reduced by up to 28% of its original number.

Table 8.1: The concept of critical machines can be incorporated in the BCU-based TSCOPF algorithm to further reduce the number of inequality constraints.

	Without reduction		**With reduction (1 critical machine)**		**# of eliminated constraints**	**Relative improvement in number of constraints %**
System	**Inequalities** Rotor angles (thresholds)	**Total number of constraints**	**Inequalities** Rotor angles (thresholds)	**Total number of constraints**		
WSCC9	150	**510**	50	**410**	100	19.61%
New England	500	**1763**	50	**1313**	450	25.52%
IEEE145	2500	**8588**	50	**6138**	2450	28.53%

A new BCU-based preventive control scheme can also be developed by using the framework we presented in Chapter 4. Different algorithms and conditions must however be developed so that the preventive control actions can terminate when a contingency become sufficiently secure. Furthermore, the group properties may be applied to the BCU-based preventive control scheme to further enhance its performance.

BIBLIOGRAPHY

[1] P. Kundur, *Power System Stability and Control.*, New York: McGraw-Hill, 1994.

[2] P. W. Sauer, and M. A. Pai, "Power Systems Dynamics and Stability," 1998.

[3] M. A. Pai, *Energy Function Analysis for power System Stability.* Boston, MA: Kluwer, 1989.

[4] P. M. Anderson and A. A. Fouad, *Power System Control and Stability*, 2nd edition, IEEE Press, New York, 2002.

[5] A. A. Fouad and V. Vittal, *Power System Transient Stability Analysis Using the Transient Energy Function Method.* Englewood Cliffs, NJ: Prentice-Hall, 1992.

[6] H.-D. Chiang, *Direct Methods for Stability Analysis of Electric Power Systems: Theoretical Foundation, BCU Methodologies, and Applications*, Wiley, New Jersey, 2011

[7] H.-D. Chiang, F. F. Wu, P. P. Varaiya, "Foundations of direct methods for power system transient stability analysis," *IEEE Transactions on Circuits and Systems*, vol.34, no.2, pp. 160- 173, Feb 1987

[8] H.-D. Chiang, F. F. Wu, P. P. Varaiya, "Foundations of the potential energy boundary surface method for power system transient stability analysis," *IEEE Transactions on Circuits and Systems*, vol.35, no.6, pp.712-728, Jun 1988

[9] H.-D. Chiang, M. W. Hirsch, F. F. Wu, "Stability regions of nonlinear autonomous dynamical systems," *IEEE Transactions on Automatic Control*, vol.33, no.1, pp.16-27, Jan. 1988

[10] H.-D. Chiang, J. S. Thorp, "Stability regions of nonlinear dynamical systems: a constructive methodology," *IEEE Transactions on Automatic Control*, vol.34, no.12, pp.1229-1241, Dec 1989

[11] H.-D. Chiang, "Study of the existence of energy functions for power systems with losses," *IEEE Transactions on Circuits and Systems*, vol.36, no.11, pp.1423-1429, Nov 1989

[12] H.-D. Chiang and J. S. Thorp, "The closest unstable equilibrium point method for power system dynamic security assessment," *IEEE Trans. Circuits Syst.*, vol. 36, pp. 1187-1199, Dec 1989.

[13] H.-D. Chiang, F. F. Wu, P. P. Varaiya, "A BCU method for direct analysis of power system transient stability," *IEEE Transactions on Power Systems*, vol.9, no.3, pp.1194-1208, Aug 1994

[14] H.-D. Chiang, C.-C. Chu, "Theoretical foundation of the BCU method for direct stability analysis of network-reduction power system. Models with small transfer Conductances," *IEEE Transactions on Circuits and Systems I: Fundamental Theory and Applications*, vol.42, no.5, pp.252-265, May 1995

[15] H.-D. Chiang, C.-C. Chu, G. Cauley, "Direct stability analysis of electric power systems using energy functions: theory, applications, and perspective," *Proceedings of the IEEE* , vol.83, no.11, pp.1497-1529, Nov 1995

[16] J. Tong, H.-D. Chiang, T. P. Conneen, "A sensitivity-based BCU method for fast derivation of stability limits in electric power systems," *IEEE Transactions on Power Systems*, , vol.8, no.4, pp.1418-1428, Nov 1993

[17] Y. Tada, A. Kurita, Y. Zhou, K. Koyanagi, H.-D. Chiang, Y. Zheng, "BCU-guided time-domain method for energy margin calculation to improve BCU-DSA system," *Transmission and Distribution Conference and Exhibition 2002: Asia Pacific. IEEE/PES* , vol.1, no., pp. 366- 371 vol.1, 6-10 Oct. 2002

[18] H.-D. Chiang, H. Li, Z. Yan, C.-S. Wang, "BCU classifiers for on-line dynamic contingency screening of electric power systems," *Power System Technology, 1998. Proceedings. POWERCON '98. 1998 International Conference on* , vol.2, no., pp.1260-1265 vol.2, 18-21 Aug 1998

[19] H.-D. Chiang, C.-S. Wang, H. Li, "Development of BCU classifiers for on-line dynamic contingency screening of electric power systems," *IEEE Transactions on Power Systems* , vol.14, no.2, pp.660-666, May 1999

[20] H.-D. Chiang, Y. Tada, H. Li, T. Takazawa, "TEPCO-BCU for on-line dynamic security assessments of large-scale power systems," *8th International Conference on Advances in Power System Control, Operation and Management (APSCOM 2009)*, vol., no., pp.1-14, 8-11 Nov. 2009

[21] H.-D. Chiang, J. Tong, Y. Tada, "On-line transient stability screening of 14,000-bus models using TEPCO-BCU: Evaluations and methods," *2010 IEEE Power and Energy Society General Meeting*, vol., no., pp.1-8, 25-29 July 2010

[22] C.-C. Chu, H.-D. Chiang, "Boundary properties of the BCU method for power system transient stability assessment," *Proceedings of 2010 IEEE International Symposium on Circuits and Systems (ISCAS)*, vol., no., pp.3453-3456, May 30 2010-June 2 2010

[23] C.-C. Chu, H.-D. Chiang, J. S. Thorp, "An investigation of invariant properties of unstable equilibrium points on the stability boundary for simple power system models," *IEEE Int. Symp. on Circuits and Systems (ISCAS'95)*, vol 1, pp. 287-290, 1995

[24] G. C. Ejebe, and J. Tong, "Discussion of Clarifications on the BCU method for transient stability analysis", *IEEE Trans. on Power Systems*, vol. 10, no. 1 , pp. 218-219, Feb. 1995

[25] A. Llamas, J. De La Ree Lopez, L. Mili, A. G. Phadke, and J. S. Thorp, "Clarifications on the BCU method for transient stability analysis," *IEEE Trans. on Power Systems*, vol. 10, no. 1, pp. 210-219, Feb. 1995.

[26] F. Paganini, B. C. Lesieutre, "Generic properties, one-parameter deformations, and the BCU method," *IEEE Trans. on Circuits Syst. I: Fundamental Theory Appl.*, vol. 46, no. 6, pp. 760-763, 1999.

[27] Y. Zou, M. H. Yin, H. D. Chiang, "Theoretical Foundation of the Controlling UEP Method for Direct Transient-Stability Analysis of Network Preserving Power System Models," *IEEE Trans. on Circuits Syst. I: Fundamental Theory Appl.*, vol. 50, no. 10, pp. 1324-1336, 2003.

[28] L. F. C. Alberto, N. G. Bretas, "Application of Melnikov's method for Computing Heteroclinic Orbits in a Classical SMIB Power System Model," *IEEE Transactions on Circuits and Systems I: Fundamental Theory and Applications*, vol.47, no.7, pp.1085-1089, Jul 2000

[29] A L. F. C. Alberto, F. H. J. R. Silva, N. G. Bretas, "Direct Methods for Transient Stability Analysis in Power Systems: State of Art and Future Perspectives," *2001 IEEE Porto Power Tech Proceedings*, vol.2, no., pp.6 pp. vol.2, 2001

[30] H-D Chiang, Y. Tada, H. Li, "Power System On-line Transient Stability Assessment", in *Wiley Encyclopedia of Electrical and Electronics Engineering*. JohnWiley & Sons, Inc.

[31] H.-D. Chiang, L. Fekih-Ahmed, "On the direct method for transient stability analysis of power system structure preserving models," *IEEE International Symposium on Circuits and Systems*, pages 2545–2548, 1992.

[32] D. Gan, R. J. Thomas, R. D. Zimmerman, "Stability-constrained optimal power flow," *IEEE Transactions on Power Systems* , vol.15, no.2, pp.535-540, May 2000.

[33] Chen L., Tada Y., Okamoto H., Tanabe R., Ono A.; , "Optimal operation solutions of power systems with transient stability constraints," *IEEE Transactions on Circuits and Systems I: Fundamental Theory and Applications* , vol.48, no.3, pp.327-339, Mar 2001.

[34] La Scala M., Trovato M., Antonelli C., "On-line dynamic preventive control: an algorithm for transient security dispatch," *IEEE Transactions on Power Systems*, vol.13, no.2, pp.601-610, May 1998.

[35] De Tuglie E., Dicorato M., La Scala M., Scarpellini P., "A static optimization approach to assess dynamic available transfer capability," *IEEE Transactions on Power Systems*, vol.15, no.3, pp.1069-1076, Aug 2000.

[36] Yue Yuan, Kubokawa, J., Sasaki, H., "A solution of optimal power flow with multicontingency transient stability constraints," , *IEEE Transactions on Power Systems* , vol.18, no.3, pp. 1094- 1102, Aug. 2003

[37] Tangpatiphan K., Yokoyama A., "Adaptive Evolutionary Programming with Neural Network for Transient Stability Constrained Optimal Power Flow," *Intelligent System Applications to Power Systems, 2009. ISAP '09. 15th International Conference on* , vol., no., pp.1-6, 8-12 Nov. 2009.

[38] N. Mo, Z. Y. Zou, K. W. Chan, T. Y. G. Pong, "Transient stability constrained optimal power flow using particle swarm optimisation," *Generation, Transmission & Distribution, IET* , vol.1, no.3, pp.476-483, May 2007.

[39] L. Hakim, J. Kubokawa, Yue Yuan, Mitani T., Zoka Y., Yorino N., Niwa Y., Shimomura K., Takeuchi A., "A Study on the Effect of Generation Shedding to Total Transfer Capability by Means of Transient Stability Constrained Optimal Power Flow," *IEEE Transactions on Power Systems,* , vol.24, no.1, pp.347-355, Feb. 2009.

[40] Quanyuan Jiang, Guangchao Geng, "A Reduced-Space Interior Point Method for Transient Stability Constrained Optimal Power Flow," *IEEE Transactions on Power Systems*, vol.25, no.3, pp.1232-1240, Aug. 2010.

[41] Quanyuan Jiang, Zhiguang Huang, "An Enhanced Numerical Discretization Method for Transient Stability Constrained Optimal Power Flow," *IEEE Transactionson Power Systems*, vol.25, no.4, pp.1790-1797, Nov. 2010.

[42] Xiaojiao Tong, Wei He, Renjun Zhou, Xuehua Deng, "Calculation for optimal power flow with transient stability constraints based on semi-infinite programming algorithm," *Power and Energy Society General Meeting*, pp.1-6, 20-24 July 2008.

[43] R. D. Zimmerman and D. Gan, "MATPOWER, a MATLAB power system simulation package," Power System Engineering Research Center, Cornell Univ., Ithaca, NY, 1997.

[44] Y.C. Wu, A. S. Debs, and R. E. Marsten, "A direct nonlinear predictor-corrector primal-dual interior point algorithm for optimal power flows," *IEEE Trans. Power Syst.*, vol. 9, no. 2, pp.876-883, May 1994.

[45] H. Wei, H. Sasaki, J. Kubokawa, and R. Yokoyama, "An interior point nonlinear programming for optimal power flow problems with a novel data structure," *IEEE Trans. Power Syst.*, vol. 13, no. 3, pp. 870–877, Aug. 1998.

[46] W. Suampun, H. D. Chiang, "Evaluation Study of the Incorporation of Transient Stability Constraints into Optimal Power Flow," Submitted to *IEEE Transactions on Power Systems*

[47] M. Ribben-Pavella and F. J. Evans, "Direct methods for studying dynamics of large scale power systems—A survey," *Automatica*, vol. 32, pp. 1-21 Jan. 1985.

[48] P. Varaiya, F. F. Wu, and R. L. Chen, "Direct methods for transient stability analysis of power systems: Recent results," *Proc. IEEE*, vol. 73, pp. 1703-1715, Dec 1985.

[49] N. Kakimoto, Y. Ohsawa and M. Hayashi, "Transient Stability Analysis of Electric Power System via Lure-Type Lyapunov Function, Part I and II," Trans. IEE of Japan, vol. 98, pp. 516, 1978.

[50] T. Athay, R. Podmore and S. Virmani, "A practical method for direct analysis of transient stability," *IEEE Trans.Power Appar. Syst.*, vol. PAS-98, pp. 573-584, 1979.

[51] H. Yee and B. D. Spalding, "Transient stability analysis of multi-machine systems by the method of hyperplanes," *IEEE Trans. Power App. Syst.*, vol. PAS-96, no. 1, pp. 276-284, Jan. 1977.

[52] P. A. Cook and A. M. Eskicioglu, "Transient stability analysis of electric power systems by the method of tangent hypersurface," *Proc. Inst. Elect. Eng.*, vol. 130, pt. C, pp. 183-193, Jul. 1983.

[53] D. Z. Cheng and J. Ma, "Calculation of stability region," in *Proc. 2003 (42nd) IEEE Conf. Decision and Control*, 2003, vol. 6, pp. 5615-5620.

[54] A. Xue, F. F. Wu, Q. Lu and S. Mei, "Power system dynamic security region and its approximations," *IEEE Trans. Circuits Syst.*, vol. 53, no. 12, Dec. 2006.

[55] S. Saha, A. A. Fouad, W. H. Kliemann, and V. Vittal, "Stability boundary approximation of a power system using the real normal form of vector fields," *IEEE Trans. Power Syst.*, vol.12, no.2, pp797-802, May 1997.

[56] V. Venkatasubramanian and J. I. Weijun, "Numerical approximation of (n-1) dimension stable manifold in large systems such as power systems," *Automatica*, vol. 33, no. 10, pp. 1877-1883, 1997.

[57] Y. Susuki, T. Hikihara and H. D. Chiang, "Stability boundaries analysis of electric power system with dc transmission based on differential-algebraic equation system", IEICE Trans. on Fundamentals of Electronics, Communications and Computer Sciences, vol. E87-A, n.9, pp. 2339-2346, Sep 2004.

[58] C. L. DeMarco, A. R. Bergen, "Application of Singular Perturbation techniques to Power System Transient Stability Analysis," *IEEE International Symposium on Circuits and Systems*, pp. 597-601.

[59] R. E. O'Malley, Jr. "Singular Perturbation Methods for Ordinary Differential Equations", Applied Mathematical Series, v.89, Springer Verlag, 1991.

[60] Y. Zou, M. H. Yin and H. D. Chiang, "Theoretical foundation of the controlling UEP method for direct transient-stability analysis of network-preserving power system models", IEEE Trans. Circuits Syst. I: Fundamental Theory and Applications, vol. 50, n.10, pp. 1324-1336, Oct 2003.

[61] L. Alberto, W. Suampun, H.-D. Chiang, "Towards Development of a CUEP Method for Network-Preserving Power System Models," Submitted to ISCAS 2013

[62] Zhujun Jing, Zhiyuan Jia, Yinghui Gao , "Research of the stability region in a power system," *IEEE Trans. Circuits and Systems I: Fundamental Theory and*, vol.50, no.2, pp. 298- 304, Feb 2003

[63] C. L. DeMarco and T. J. Overbye, "An energy based security measure for assessing vulnerability to voltage collapse," *IEEE Trans. Power Syst.*, vol. 5, pp. 419–427, May 1990.

[64] V. Venkatasubramanian, H. Schattler, J. Zaborsky, "Dynamics of large constrained nonlinear systems-a taxonomy theory," *Proceedings of the IEEE* , vol.83, no.11, pp.1530-1561, Nov 1995

[65] V. Venkatasubramanian, H. Schattler, J. Zaborsky, "Local bifurcations and feasibility regions in differential-algebraic systems, " *IEEE Transactions on Automatic Control*, vol.40, no.12, pp.1992-2013, Dec 1995

[66] N. Tsolas, A. Arapostathis, P. Varaiya, "A structure preserving energy function for power system transient stability analysis," *IEEE Transactions on Circuits and Systems*, vol.32, no.10, pp. 1041- 1049, Oct 1985

[67] T. Athay, R. Podmore, S. Virmani, "A Practical Method for the Direct Analysis of Transient Stability," *IEEE Transactions on Power Apparatus and Systems*, vol.PAS-98, no.2, pp.573-584, March 1979

[68] C.C. Chu, H.-D. Chiang, "Constructing Analytical Energy Functions for Lossless Network-Reduction Power System Models: Framework and New Developments," *Circuits Systems and Signal Processing*, Vol. 18, No. 1, 1999.

[69] C.C. Chu, H.-D. Chiang, "Constructing Analytical Energy Functions for Lossless Network-Preserving Power System Models," *Circuits Systems and Signal Processing*, Vol. 24, No. 4, 2005.

[70] A. R. Bergen and D. J. Hill, A structure preserving model for power system stability analysis, *IEEE Trans. Power Apparatus and Systems*, PAS-100:25–35, 1981.

[71] A. R. Bergen, D. J. Hill, and C. L. De Marco, Lyapunov function for multi-machine power systems with generator flux decay and voltage dependent loads, *Internat. J. Electrical Power Energy Systems*, 8(1):2–10, 1986.

[72] A. R. Bergen and V. Vittal, *Power System Analysis*, 2nd edition, Prentice-Hall, Englewood Cliffs, NJ, 1999.

[73] R. J. Davy and I. A. Hiskens," Lyapunov functions for multimachine power systems with dynamic loads", *IEEE Trans. Circuits and Systems Part I: Fundamental Theory and Applications*, CAS-44(9):796–821, September 1997

[74] I. A. Hiskens, R. J. Davy, "Lyapunov function analysis of power systems with dynamic loads," *Proceedings of the 35th IEEE Conference on Decision and Control, 1996.*, vol.4, no., pp.3870-3875 vol.4, 11-13 Dec 1996

[75] G. E. Gless, Direct method of Lyapunov applied to transient power system stability, *IEEE Trans. Power Apparatus and Systems*, PAS-85:164–179, 1966.

[76] M. Ribbens-Pavella and P. G. Murthy, *Transient Stability of Power Systems: Theory and Practice*, Wiley, New York, 1994.

[77] S. Tanneeru, J. Mitra, Y. J. Patil, S. J. Ranade, "Effect of Large Induction Motors on the Transient Stability of Power Systems," *2007 NAPS '07. 39th North American Power Symposium*, , vol., no., pp.223-228, Sept. 30 2007-Oct. 2 2007

[78] L. Pereira, D. Kosterev, P. Mackin, D. Davies, J. Undrill, W. Zhu, "An interim dynamic induction motor model for stability studies in the WSCC," *IEEE Transactions on Power Systems*, vol.17, no.4, pp. 1108- 1115, Nov 2002

[79] H.-D. Chiang, J.-C.Wang, C.-T. Huang, Y.-T. Chen, and C.-H. Huang, "Development of a dynamic ZIP-motor load model from on-line field measurements," *Int. J. Elect. Power Energy Syst.*, vol. 19, no. 7, pp. 459–468, 1997.

[80] C.-J. Lin, Y.-T. Chen, H.-D. Chiang, and J.-C. Wang, "Dynamic load models in power systems using the measurement approach," *IEEE Trans. Power Syst.*, vol. 8, no. 1, pp. 309–315, Feb. 1993.

[81] D. Karlsson and D. J. Hill, "Modelling and identification of nonlinear dynamic loads in power systems," *IEEE Trans. Power Syst.*, vol. 9, no. 1, pp. 157–166, Feb. 1994.

[82] B.-K. Choi, H.-D. Chiang, Y. Li, H. Li, Y.-T. Chen, D.-H. Huang, M. G. Lauby, "Measurement-based dynamic load models: derivation, comparison, and validation," *IEEE Transactions on Power Systems*, vol.21, pp.1276-1283, Aug. 2006

[83] "Standard load models for power flow and dynamic performance simulation," *IEEE Transactions on Power Systems*, vol.10, no.3, pp.1302-1313, Aug 1995

[84] T. S. Key, "Predicting behavior of induction motors during severe faults and interruptions," *IEEE Industry Applications Magazine*, Jan/Feb 1995.

[85] J. C. Das, "Effects of momentary voltage dips on the operation of induction and synchronous motors," *IEEE Transactions on Industry Applications*, vol. 26, no. 4, July/Aug 1990, pp. 711–718.

[86] G. W. Bottrell and L. Y. Yu, "Motor behavior through power system disturbances," *IEEE Transactions on Industry Applications*, vol. 16, no. 5, Sep/Oct 1980, pp. 600–604.

[87] J. J. Cathey, R. K. Cavin, A. K. Ayoub, "Transient Load Model of an Induction Motor," *IEEE Transactions on Power Apparatus and Systems*, vol.PAS-92, no.4, pp.1399-1406, July 1973

[88] F. Nozari, M. D. Kankam, W. W. Price, William, "Aggregation of Induction Motors for Transient Stability Load Modeling," *IEEE Transactions on Power Systems*, vol.2, no.4, pp.1096-1103, Nov. 1987

[89] D. Ruiz-Vega, T. I. Asiain Olivares, D. Olguin Salinas, "An approach to the initialization of dynamic induction motor models," *IEEE Transactions on Power Systems*, vol.17, no.3, pp. 747- 751, Aug 2002

[90] D. Ruiz, T. Asiain, D. Olguin, "Improvement of induction motors models for power system transient stability studies," *1999. PowerTech Budapest 99. International Conference on Electric Power Engineering*, vol., no., pp.70, 1999

[91] K. R. Sreerama, R. Ramanujam, H. P. Kincha, L. Jenkins, "Induction motor modelling and interfacing technique for fast transient stability simulation," *1998. Proceedings of EMPD '98. 1998 International Conference on Energy Management and Power Delivery*, vol.2, no., pp.548-551 vol.2, 3-5 Mar 1998

[92] M. Watanabe, Y. Mitani, H. Iki, Y. Uriu, Y. Urano, "Transient stability assessment of industrial power systems with detailed models implementation," *2011 IEEE Industry Applications Society Annual Meeting (IAS)*, vol., no., pp.1-6, 9-13 Oct. 2011

[93] PSAT computation package

[94] Chih-Wen Liu, J. S. Thorp , "A novel method to compute the closest unstable equilibrium point for transient stability region estimate in power ystems," *IEEE Transactions*

on Circuits and Systems I: Fundamental Theory and Applications, vol.44, no.7, pp.630-635, Jul 1997.

[95] X.-D. Dai, D. He, L.-L. Fan, N.-H. Li, H. Chen, H., "Improved ANN αth-order inverse TCSC controller for enhancing power system transient stability," *IEE Proceedings-Generation, Transmission and Distribution*, vol.146, no.6, pp.550-556, Nov 1999

[96] W. A. Mittelstadt, J. L. Saugen, J.L., "A Method of Improving Power System Transient Stability Using Controllable Parameters," *IEEE Transactions on Power Apparatus and Systems*, vol.PAS-89, no.1, pp.23-27, Jan. 1970

[97] K. S. Shim, H. K. Nam, S. G. Song, Y. G. Kim, K. Y. Lee, "Application results of the eigen-sensitivity theory of augmented matrix to small signal stability analysis of large power systems," *2000. IEEE Power Engineering Society Summer Meeting*, vol.3, no., pp.1835-1838 vol. 3, 2000

[98] J. P. Bayne, P. Kundur, W. Watson, "Static exciter control to improve transient stability," *IEEE Transactions on Power Apparatus and Systems*, vol.94, no.4, pp. 1141-1146, July 1975

[99] C.-N. Huang, "Preventive flow control for transient stability by phase shifting transformers," *2003 IEEE PES Transmission and Distribution Conference and Exposition*, vol.2, no., pp. 677- 682 vol.2, 7-12 Sept. 2003

[100] M. Poshtan, B. N. Singh, P. Rastgoufard, "A Nonlinear Control Method for SSSC to Improve Power System Stability," *2006. PEDES '06. International Conference on Power Electronics, Drives and Energy Systems,* , vol., no., pp.1-7, 12-15 Dec. 2006

[101] S. H. Hosseini, A. Ajami, "Transient stability enhancement of AC transmission system using STATCOM," *TENCON '02. Proceedings. 2002 IEEE Region 10 Conference on Computers, Communications, Control and Power Engineering*, vol.3, no., pp. 1809- 1812 vol.3, 28-31 Oct. 2002

[102] Ch. Praing, T. Tran-Quoc, R. Feuillet, J. C. Sabonnadiere, J. Nicolas, K. Nguyen-Boi, L. Nguyen-Van, "Impact of FACTS devices on voltage and transient stability of a power system including long transmission lines," *2000. IEEE Power Engineering Society Summer Meeting*, vol.3, no., pp.1906-1911 vol. 3, 2000

[103] V. Mahajan, "Power System Stability Improvement with Flexible A.C. Transmission System (FACTs) Controller," *2008. POWERCON 2008. Joint International Conference on Power System Technology and IEEE Power India Conference*, vol., no., pp.1-7, 12-15 Oct. 2008

[104] S. R. Wagh, A. K. Kamath, N. M. Singh, N.M., "Non-linear Model Predictive Control for improving transient stability of power system using TCSC controller," *2009. ASCC 2009. 7th Asian Control Conference*, vol., no., pp.1627-1632, 27-29 Aug. 2009

[105] A. V. MacHias, J. L. Souflis, "A fuzzy approach in the determination of unstable machines," *IEE Proceedings C Generation, Transmission and Distribution*, vol.137, no.2, pp.115-122, Mar 1990

[106] S. Limyingcharoen, U. D. Annakkage, N. C. Pahalawaththa, "Effects of unified power flow controllers on transient stability ," *IEE Proceedings- Generation, Transmission and Distribution*, vol.145, no.2, pp.182-188, Mar 1998

[107] H. Chen, Y. Wang, R. Zhou, "Transient and voltage stability enhancement via coordinated excitation and UPFC control," *IEE Proceedings- Generation, Transmission and Distribution*, vol.148, no.3, pp.201-208, May 2001

[108] E. Gholipour, S. Saadate, "Improving of transient stability of power systems using UPFC," *IEEE Transactions on Power Delivery*, vol.20, no.2, pp. 1677- 1682, April 2005

[109] C. V. The, K. La Minh, T. T. Quoc, N. B. Khue, L. D. Son, "FACTS Devices Applications on Power System to Improve the Angle Stability," *2006. APCCAS 2006. IEEE Asia Pacific Conference on Circuits and Systems*, vol., no., pp.1358-1363, 4-7 Dec. 2006

[110] R. Patel, T. S. Bhatti, D. P. Kothari, D.P., "Improvement of power system transient stability by coordinated operation of fast valving and braking resistor," *IEE Proceedings- Generation, Transmission and Distribution*, vol.150, no.3, pp. 311- 316, 13 May 2003

[111] J. J. Ford, G. Ledwich, Z.Y. Dong, Z.Y., "Efficient and robust model predictive control for first swing transient stability of power systems using flexible AC transmission systems devices," *IET Generation, Transmission & Distribution*, vol.2, no.5, pp.731-742, September 2008

[112] Y. Xia, K. W. Chan, T. S. Chung, "A TEF approach for solving transient stability constrained OPF," *2004. PowerCon 2004. 2004 International Conference on Power System Technology*, vol.2, no., pp. 1485- 1489 Vol.2, 21-24 Nov. 2004

[113] D. Z. Fang, Y. Xiaodong, S. Jingqiang, Y. Shiqiang, Z. Yao, "An Optimal Generation Rescheduling Approach for Transient Stability Enhancement," *IEEE Transactions on Power Systems*, vol.22, no.1, pp.386-394, Feb. 2007

[114] A. Hoballah, I. Erlich, "Generation coordination for transient stability enhancement using particle swarm optimization," *2008. MEPCON 2008. 12th International Middle-East Power System Conference*, vol., no., pp.29-33, 12-15 March 2008

[115] H. Raoufi, M. Kalantar, "Reactive power rescheduling with generator ranking for voltage stability improvement," *2008 IEEE Power and Energy Society General Meeting - Conversion and Delivery of Electrical Energy in the 21st Century*, vol., no., pp.1-5, 20-24 July 2008

[116] T. B. Nguyen, M. A. Pai, "Dynamic security-constrained rescheduling of power systems using trajectory sensitivities," *IEEE Transactions on Power Systems*, vol.18, no.2, pp. 848- 854, May 2003

[117] M. R. Aghamohammadi, A. Maghami, F. Dehghani, "Dynamic security constrained rescheduling using stability sensitivities by neural network as a preventive tool," *2009. PSCE '09. IEEE/PES Power Systems Conference and Exposition*, vol., no., pp.1-7, 15-18 March 2009

[118] D. Z. Fang, W. Sun, Z. Y. Xue, "Optimal generation rescheduling with sensitivity-based transient stability constraints," *IET Generation, Transmission & Distribution*, vol.4, no.9, pp.1044-1051, September 2010

[119] I. Genc, R. Diao, V. Vittal, "Computation of transient stability related security regions and generation rescheduling based on decision trees," *2010 IEEE Power and Energy Society General Meeting*, vol., no., pp.1-6, 25-29 July 2010

[120] L. Wang, A. A. Girgis, "A new method for power system transient instability detection," *IEEE Transactions on Power Delivery*, vol.12, no.3, pp.1082-1089, Jul 1997

[121] M. Ribbens-Pavella, P. G. Murthy, J. L. Horward, "The acceleration approach to practical stability domain estimation in power systems," *1981 20th IEEE Conference on Decision and Control including the Symposium on Adaptive Processes*, vol.20, no., pp.471-477, Dec. 1981

[122] W. P. Yuan, K. W. Chan, Y. Zhang, "Identification of critical cluster in transient stability study using line potential energy method," *2006. IEEE Power Engineering Society General Meeting*, vol., no., pp.6 pp.

[123] Y. Xue, M. Pavella, "Critical-cluster identification in transient stability studies [of power systems]," *IEE Proceedings C Generation, Transmission and Distribution*, vol.140, no.6, pp.481-489, Nov 1993

[124] Y. Xue, T. Van Cutsem, M. Ribbens-Pavella, "Real-time analytic sensitivity method for transient security assessment and preventive control," *IEE Proceedings C Generation, Transmission and Distribution*, vol.135, no.2, pp.107-117, Mar 1988

[125] D.-H. Kuo, A. Bose, "A generation rescheduling method to increase the dynamic security of power systems," *IEEE Transactions on Power Systems*, vol.10, no.1, pp.68-76, Feb 1995

[126] A. A. Fouad, S. E. Stanton, "Transient Stability of a Multi-Machine Power System Part I: Investigation of System Trajectories," *IEEE Transactions on Power Apparatus and Systems*, vol.PAS-100, no.7, pp.3408-3416, July 1981

[127] R. Grondin, A. Heniche, M. Dobrescu, G. Trudel, M. Rousseau, A. Edwards, S. Richards, B. Kirby, "Loss of Synchronism Detection, A Strategic Function for Power Systems," *2008. DPSP 2008. IET 9th International Conference on Developments in Power System Protection*, vol., no., pp.380-386, 17-20 March 2008

[128] K. R. Padiyar, S. Krishna, "Online detection of loss of synchronism using energy function criterion," *IEEE Transactions on Power Delivery*, vol.21, no.1, pp. 46- 55, Jan. 2006

[129] A. A. Fouad, J. Tong, "Stability constrained optimal rescheduling of generation," *IEEE Transactions on Power Systems, ,* vol.8, no.1, pp.105-112, Feb 1993

[130] R. Qi, D. Cook, W. Kliemann, V. Vittal, "Visualization of Stable Manifold and Multidimensional Surfaces in the Analysis of Power System Dynamics," *J. Nonlinear Sci.*, vol. 10, pp. 175-195, 2000

[131] D. Cheng, J. Ma, "Calculation of Stability Region," *Proceedings of the 42nd IEEE Conference on Decision and Control*, pp. 5615-5620, December 2003

[132] F. M. Salam, A. Arapostathis, P. P. Varaiya, "Analytic Expressions for the Unstable Manifold at Equilibrium Points in Dynamical Systems of Differential Equations," *The 22nd IEEE Conference on Decision and Control, 1983.*, vol.22, pp.1389-1392, Dec. 1983

[133] S. Ushiki, "Analytic Expressions of Unstable Manifolds," *Proc. Japan Acad. Ser. A Math. Sci.*, Volume 56, pp. 239-244, Number 1980

[134] B Krausopf, H. M. Osinga, E. J. Doedel, M. E. Henderson, J. Gukenheimer, A. Vladimirsky, M. Dellnitz, O. Junge, "A Survey of Methods for Computing (Un)Stable Manifolds of Vector Fields," *International Journal of Bifurcation and Chaos*, Vol. 15, No. 3, pp. 763–791, 2005

[135] Z. Jing, Z. Jia, Y. Gao, "Research of the stability region in a power system," *IEEE Transactions on Circuits and Systems I: Fundamental Theory and Applications, ,* vol.50, no.2, pp. 298- 304, Feb 2003

[136] V. Venkatasubramanian, H. Schattler, J. Zaborsky, "Dynamics of large constrained nonlinear systems-a taxonomy theory [power system stability]," *Proceedings of the IEEE* , vol.83, no.11, pp.1530-1561, Nov 1995

[137] V. Venkatasubramanian, H. Schattler, J. Zaborszky, "Local bifurcations and feasibility regions in differential-algebraic systems," *IEEE Transactions on Automatic Control*, vol.40, no.12, pp.1992-2013, Dec 1995

[138] J. G. Slootweg, "Wind Power Modelling and Impact on Power System Dynamics," *Phd Disseration*, 2003

[139] J. G. Slootweg, S. W. H. de Haan, H. Polinder, and W. L. Kling, “Modeling wind turbines in power system dynamics simulations,” in *Proc. IEEE Power Eng. Soc. Summer Meeting*, Vancouver, BC, Canada, July 15–19, 2001.

[140] J. G. Slootweg, H. Polinder, and W. L. Kling, “Initialization of wind turbine models in power system dynamics simulations,” in *Proc. IEEE Porto Power Tech*, Porto, Portugal, Sept. 10–13, 2001.

[141] J. G. Slootweg, S. W. H. de Haan, H. Polinder, W. L. Kling, "General model for representing variable speed wind turbines in power system dynamics simulations," *IEEE Transactions on Power Systems*, vol.18, no.1, pp. 144- 151, Feb 2003

[142] J. G. Slootweg, H. Polinder, and W. L. Kling, "Representing wind turbine electrical generating systems in fundamental frequency simulations," *IEEE Transactions on Energy Conversion,* , vol.18, no.4, pp. 516- 524, Dec. 2003

[143] K. A. Folly, S. Sheetekela, "Impact of fixed and variable speed wind generators on the transient stability of a power system network," *2009. PSCE '09. IEEE/PES Power Systems Conference and Exposition*, vol., no., pp.1-7, 15-18 March 2009

[144] H. Hou, L. Lin, T. Wu, Y. Miao, "Comparison of Transient Stability between Wind Farm Based on DFIG and Traditional Power Plant in an Actual Grid," *2010 Asia-Pacific Power and Energy Engineering Conference (APPEEC)*, vol., no., pp.1-4, 28-31 March 2010

[145] P. Ledesma, J. Usaola, "Doubly fed induction generator model for transient stability analysis," *IEEE Transactions on Energy Conversion*, vol.20, no.2, pp. 388- 397.

[146] H. Zhaoqing, M. Chengxiong, L. Jiming, "Improvement of transient stability in AC system by HVDC Light," *Transmission and Distribution Conference and Exhibition: Asia and Pacific, 2005 IEEE/PES*, pp. 1-5, 2005

[147] Y. Liu, Z. Chen, "Transient voltage stability analysis and improvement of a network with different HVDC systems," *Power and Energy Society General Meeting, 2011 IEEE*, pp. 1-8, 24-29 July 2011

[148] L. Meegahapola, D. Flynn, "Impact on transient and frequency stability for a power system at very high wind penetration," *2010 IEEE Power and Energy Society General Meeting*, vol., no., pp.1-8, 25-29 July 2010

[149] I. Mansour, D.O. Abdeslam, P. Wira, J. Merckle, "Fuzzy logic control of a SVC to improve the transient stability of ac power systems," *Industrial Electronics, 2009. IECON '09. 35th Annual Conference of IEEE*, pp.3240,3245, 3-5 Nov. 2009

[150] A. Ishigame, T. Taniguchi, "Transient stability analysis for power system using Lyapunov function with load characteristics," *2003, IEEE Power Engineering Society General Meeting*, vol.2, no., pp. 4 vol. 2666, 13-17 July 2003